Q41/6965

OPTIMIZATION OF LASER ABLATED PLUMES FOR THIN FILM DEPOSITION USING FAST PHOTOGRAPHY

by

ASHUTOSH MISRA

DEPARTMENT OF PHYSICS
INDIAN INSTITUTE OF TECHNOLOGY KANPUR
MAY, 1999

OPTIMIZATION OF LASER ABLATED PLUMES FOR THIN FILM DEPOSITION USING FAST PHOTOGRAPHY

A Thesis Submitted
in Partial Fulfilment of the Requirements
for the Degree of

DOCTOR OF PHILOSOPHY

by

ASHUTOSH MISRA

to the

DEPARTMENT OF PHYSICS
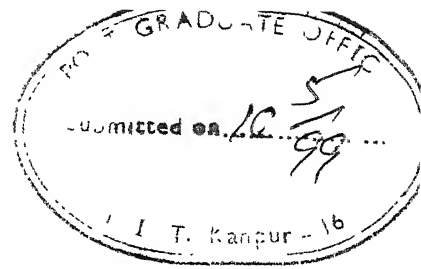
INDIAN INSTITUTE OF TECHNOLOGY KANPUR

MAY, 1999

T

1997/M

A131099

CERTIFICATE

It is certified that the work contained in this thesis entitled *"Optimization of Laser Ablated Plumes for Thin Film Deposition using Fast Photography"* by *Ashutosh Misra* has been carried out under my supervision and the same has not been submitted elsewhere for a degree.

Kanpur

May 10, 1999

(Raj K. Thareja)

Professor

Department of Physics

I. I. T. Kanpur

Dedicated

To

My Mother & Father

SYNOPSIS

Name of Student	: **Ashutosh Misra**	Roll #	:	**9410965**
Degree for which submitted	: **Ph. D.**	Department	:	**Physics**
Thesis Title	: **Optimization of Laser Ablated Plumes for Thin Film Deposition Using Fast Photography**			
Name of the thesis supervisor	: **Professor Raj K. Thareja**			

The thesis discusses in details the studies of laser ablated aluminum plasma in the presence of various ambient gases (He, Ar, O_2, N_2 & Air) at various pressures (1 mTorr-100 Torr), using moderate laser intensities (10^{10}-10^{11}Wcm^{-2}). An attempt is made both theoretically and experimentally to understand the process of evolution of a laser ablated plume in an ambient atmosphere and subsequent deposition of a thin film on to a substrate placed at pre-determined distance from the target. Intensified Charge Couple Device (ICCD) camera system is used as a tool to diagnose the expanding plasma. The images of the expanding plume front recorded at various delay times with respect to the ablating pulse are used to evaluate the velocity of the expanding front and to calculate the size of the particles in the plasma. The evolution of shock due to the expansion of high pressure plasma in an ambient atmosphere is discussed. It is inferred that at a critical distance from the target (plume length) in the shocked region the temperature is high and due to diffusion of both the ambient gas particles and the plasma species into this region, it is possible to have a vigorous chemical reaction at the interface. In order to confirm the possibility of chemical reaction, films of aluminum in oxygen were deposited at plume length. The aluminum nitride films were deposited at room temperature on a substrate placed at the breakdown front of nitrogen gas. The deposited aluminum oxide and aluminum nitride films are characterized using Scanning Electron Microscopy (SEM), Rutherford Back Scattering (RBS), Micro-Raman spectroscopy, and X-Ray Diffraction (XRD). A correlation on the characteristics of the deposited films with that of the parameters of the plume is presented.

To produce an aluminum plasma plume a Nd:YAG (Spectra Physics, DCR-4G) laser beam operating at fundamental wavelength (λ = 1.06 μ m), was focussed on to a pure aluminum target mounted in a vacuum chamber which could be evacuated to pressures better than 0.1 m Torr. The chamber has provision for introducing gas in a controlled manner. The experiments were carried out at various laser energies and in various ambient environments (He, Ar, N_2, O_2 and Air) at various pressures (1 mTorr-100 Torr). The target was continuously rotated and translated so that each laser pulse falls on a fresh target surface. The spot size on target was about 260 μm. The laser ablated plasma was investigated using (a) Fast photography, (b) Optical emission spectroscopy, (c) Faraday cup and (d) Time of flight mass spectrometer. Two-dimensional view of the plume expansion was made by recording the overall visible emission from the plasma plume with a gated ICCD camera system (ICCD 176G/2, Princeton Instrument Inc.). The detector consisted of Multi-Channel Plate (MCP) with spectral response in the wavelength range 200-800 nm and 384 x 576 CCD array. In order to have better insight of the plume dynamics, the ICCD photographs were recorded at various time delays with respect to ablating laser pulse using a pulse generator (PG-200, Princeton Instruments Inc.) and adjustable gate widths (5 ns - 20 ns) and fixed gain of MCP. The fast gate acts as a shutter for the camera and hence the name fast photography. These photographs are essentially photoelectric images of the plume. The plume front is taken along the outermost axial position where the intensity falls to 25 % of the maximum intensity.

For spectroscopic investigations of the plume the emitted plasma radiation was imaged onto the entrance slit of a monochromator (Jobin Yvon, HRS-2) with a lens of 16 cm focal length so as to have one to one correspondence with the plasma and its image onto the slit of a monochromator. The output from the monochromator was detected with a photomultiplier tube (IP28, Hamamatsu) and recorded on a strip chart recorder. The optical emission from the laser-ablated plasma in oxygen ambient at 100 mTorr was recorded at various distances and at various laser irradiances. The intensity of the emitted lines increases in presence of oxygen at 100 mTorr. The stark broadened profile of Al II (4p $^1P^o$-4d ^1D) transition at 559.3 nm was used to estimate electron density and is found to lie in the range 10^{15}-10^{16} cm^{-3}. The electron temperature of the plasma calculated at various laser energies, using emission line intensity ratio, is found to lie between 5-13 eV.

A faraday cup with a honeycomb collector was designed and used in time of flight mode to measure the distribution of ions and electrons in a laser produced aluminum plasma. One of the output ports of the target chamber at an angle of 45° with respect to the laser beam was used for the Faraday Cup. It is observed that both the kinetic energy and the ionic yield increase with increase in fluence on the target.

A time of flight mass spectrometer was developed and was used for measuring the ionization threshold of laser irradiated aluminum targets, the estimated threshold is 4.5 x 10^{10} W cm^{-2}.

We have used the equation of motion and the continuity to transform the expansion for time dependent density, pressure and velocity into force equations that give the dynamics of the plume's maximum density boundary. The simulated plume front is observed to match well with the ICCD images of the plumes.

The analysis of the recorded images show that the expansion is more in the longitudinal direction than in the transverse direction. From the displacement time plots the velocity of the expanding front is estimated to be 7.29 x 10^6 cm/sec, 6.84 x 10^6 cm/sec, 6.75 x 10^6 cm/sec and 6.21 x 10^6 cm/sec respectively for He, Air, O_2 and Ar ambient at 10 mTorr. It is observed that displacement of the plume front decreases with increase in ambient pressure, the displacement increases with increase in incident laser energy because of increase in the energy coupled to the target.

The recorded ICCD images show that the expansion is conical at earlier times with vertex at the focusing point of the laser. The equations of mass, momentum and energy conservation at the shock-ambient interface are used to estimate the plasma and shock parameters. It is observed that the vapor pressure decreases with the increase in time and ambient gas pressure, also the vapor temperature decreases with time and with ambient gas pressures. This is attributed to the difference in heat capacities of plasma species and the ambient atmosphere. It is observed that the shock temperature (~ 1.922 x 10^6 K, in 100 mTorr of oxygen at 29 ns after the ablating pulse) is greater than the vapor temperature (~ 2.089 x 10^5 K, in 100 mTorr at 29 ns after the ablating pulse). The surface temperature of the target is estimated using the expansion velocity of the luminous front of the blow off material. The surface temperature (~1.18 x 10^6 K) is found to be much greater than the

sublimation temperatures (~8500 K) of the metal and hence no superheating of the surface can occur above the normal vaporization temperature.

The dynamics of the expanding plume is also studied with a classical drag and blast wave model. The collisions between the particles of the ambient gas and plume attenuate and slow down the plume particles. The propagating plume progressively slows down eventually coming to rest due to viscous drag force. The distance from the target at which the propagation ceases is called stopping distance or plume length. As the pressure of the ambient atmosphere increases the stopping distance decreases and the intensity of the plume increases. The increase in intensity is due to confinement of the plasma to a small volume.

According to the blast wave theory the position of the shock front R follows an equation of the form $R = K_1 t^q$, where, K_1 is a constant, q an exponent and has a value of 0.4 for an ideal shock condition and 1 for free expansion. The fit of this equation to our experimental data shows that value of the exponent lies in the range, $0.22 \leq q \leq 0.48$ for laser irradiance of ~ 10^{10} - 10^{11} W/cm^2. The discrepancy in the value of exponent may be due to the growth of instability at moderate laser intensities and low pressures.

The collision of the plasma species with that of ambient gas may result in the formation of clusters. The size of the particles is estimated using the ICCD images by assuming the plasma as an ensemble of small spherical particles radiating like a blackbody at high temperature. The size of the particles after 400 ns of the ablating pulse, at pressures 10 mTorr, 100 mTorr, 10 Torr and 100 Torr is calculated to be 1.20, 1.02, 0.12 and 0.11 μm respectively.

In order to verify the possibility of a chemical reaction in the shocked region, we deposited aluminum films in oxygen atmosphere at various target substrate distances (1.0, 2.0 and 3.0 cm). The distance of 2.0 cm corresponds to a distance where the plume propagation ceases, as inferred from ICCD images. The other two distances (1.0 and 3.0 cm) are chosen to compare the quality of the film with that of 2.0 cm film. SEM photographs show that the films deposited at a distance of 1.0 cm are denser in aluminum as compared to the films deposited at 2.0 cm and 3.0 cm from the target. However, the RBS spectra showed that the chemical composition of the deposited films at 2.0 cm in the stoichiometric ratio of Al:O to be 2:3, implying that background oxygen has reacted with

the plasma particles resulting in change of chemical composition of the film. The film deposited at 1.0 and 3.0 cm showed compositional (Al:O) change as 1:1.33 and 1.2:3. Micro-Raman spectra of the films confirmed the presence of Al_2O_3 in the films. The analysis of the Raman bands of c-Si (521 cm^{-1}) and Al_2O_3 (755 cm^{-1}) established that optimum target-substrate distance for the oxygen rich films is the plume length or stopping distance. It is in accordance with our earlier result that a chemical reaction takes place at the plasma-compressed region-gas interface and the plume length is the optimum position for the deposition of thin oxide film.

Breakdown of the ambient gas is observed at high ambient pressure and moderate laser intensities. This property of the gas is made use of in depositing aluminum nitride films on silicon substrate at room temperature. The ICCD images are used to locate the exact position of breakdown front of the N_2 gas and a substrate is placed at this position. The laser irradiation used was 1.65×10^{11} W/cm^2 with an ambient gas pressure of 100 Torr. The XRD peaks observed at 38.5°, 44.7°, 65.2°, 78.4°, 82.5°, and 116.7° match well with that available in the literature. The SEM photograph of the films show that the density of the films formed on the substrate is very high. The Raman bands corresponding to Al_2O_3 observed at 239, 252, 607, 610, 614, 667 and 673 cm^{-1} match well with that available in the literature. The Raman and XRD spectra indicate that the films are crystalline in nature. The Raman spectrum of the annealed film showed a considerable increase in the intensity of the AlN bands. The increase in intensity in the annealed films is attributed to impregnation of the flowing nitrogen at high temperatures.

To conclude, an extensive investigation of laser ablated aluminum plume using fast photography (ICCD) is presented. The measurement of various plasma parameters in ambient atmosphere and the shocked regime is reported. The proposed technique for depositing oxide films may be useful for the growth of high T_c superconducting films and ceramic films. The AlN films deposited at room temperature may help in the short wavelength applications, hard coatings and in various opto-electronic and micro electronic devices.

ACKNOWLEDGEMENTS

Some moments come in life, when one finds it difficult to express his feelings. Twenty-six alphabets, in a variety of permutations and combinations seem to help out but ones vocabulary falls short of words and phrases. The same is true with me, now when I want to express my gratitude to Professor R. K. Thareja for introducing me to the field of laser ablated plasmas. His able guidance, valuable suggestions, everlasting enthusiasm for physics, motivation towards work, keen and sustained interest in the course of work enabled me to bring this work to fruition. His intuitive, ingenuity and approach to solving problems of both academic and social nature always overwhelmed me during my interaction with him both academically and socially. His idea of simple living and high thinking has been a great source of inspiration for me. Working with him was a great experience.

I express my sincere regards to Dr. (Mrs.) Sukarma Thareja, for her cordial behavior, constant encouragement, and suggestions. Her hospitality at all my visits gave me my first lessons on social interaction.

I sincerely thank Professors K.K. Sharma, V. Ravishankar and V. A. Singh for their evaluations and fruitful suggestions from time to time.

My heartfelt thanks to Ashwini, Narayanan and Ani'da (Anirban) for their direct or indirect help in finalizing my thesis.

Special thanks are due to Dr. R. K. Dwivedi, who introduced me to the academic world of IITK. I also express my gratitude to Drs. R. K. Dwivedi, Vinay Kumar, Amit Sircar, Abhilasha, Ranjit Singh, Alika Khare, and Amit Neogi for their inspiration, suggestions and care during my visits to them.

I record my sense of indebtness to Ani'da who has spent nights with me in laboratory during my experimentation. I wish to thank Ani'da, Narayanan, Ashwini and S. P. Singh for their respect, co-operation and support with selfless spirits to me during all my stay at IIT K. I wish all of them great success in their research endeavors.

I also record my gratefulness to Mr. Gopesh Tiwari, who introduced me to the field of computers and has always been my last resource. When all sources dried up, he used to come up with encouraging solutions and advice, even at odd hours.

I express my appreciation towards Professor H. D. Bist and Dr. M. S. Navati during experimentation with Raman setup and Professor V. N. Kulkarni and Dr. T. Som for their help in carrying out experiment with RBS setup.

Hostel life is an important part of any academic life, I am thankful to all the residents of Hall V for the respect, cooperation and encouragement extended to me in

various hall activities. I wish to thank all my wardens who kept bearing with me in spite of my opposition to them on various issues. I thank Rajan, Alok, Tapoda, Sudhir, Kushal, Sanat, Gopal Das, Banga, Kaliprasad, Kalyan, Mahesh, Dwarika, Navati and many others, who along with Hall V residents made my stay at IIT K enjoyable and full of blooming memories.

I would like to take this opportunity to express my sincere appreciation to all my Professors and teachers of IIT K, Christ Church College, Kanpur and St. Joshep's Convent Sr. Sec. School, Kanpur, especially, Professors Y. R. Waghmare, R. K. Thareja, A. N. Dixit, P. P. Varma, Mukul Misra, V. K. Srivastava, R. K. Dwivedi, Mrs. Shruti and Mr. J. B. Singh whose cooperation on several occasions have enabled me to move forward.

I am filled with joy and nostalgia to remember my friends at this moment-Deepak, Ajay, Arvind, Sameer and Chiranjib who have been my colleagues at various stages of life. Even their family members have always made me feel as if I was one among them.

I am thankful to Mrs. Shubha Karnick for giving me lessons in French languange and Drs. (Mrs.) Sushma Tiwari and Raghvendra Tiwari for teaching me programming in 'C'.

I also thank Professors Deepak Mathur, G. Ravindra Kumar and especially Mr. F. A. Rajghara for helping me in designing the TOFMS. I would also like to acknowledge the help of Dheeraj and Tripti during the development of Faraday cup.

I would like to thank all the Staff members of CELT & Physics office, CELT & Physics workshop, DORD office, for providing me timely help. A special word of thanks to Mr. R. K. Bajpai, for preparing the tracings and other assistance whenever, I asked for.

I wish to acknowledge University Grants Commission, New Delhi for providing me financial support during my research work.

A word of love to my dearest little friends: Aditya, Abhishek, Raghav and Esha for their affection.

I express my gratitude to my parents, brother and sister for their constant display of affections, encouragement, and moral support. Their love and affection has been a constant source of inspiration for me, through out.

Lastly, I would like to confess to Professor G. K Shukla, one of my well wishers, whom I never knew was in such a close relationship to me, and still after knowing, I could visit him only thrice.

Ashutosh

LIST OF PUBLICATIONS

1. A. Neogi, A. Misra and R. K. Thareja
   Dynamics of Laser Produced Carbon Plasma Expanding in Low Pressure Ambient Atmosphere, J. Appl. Phys. **83**, (1998) 2831

2. R. K. Thareja, A. Misra and S. R. Franklin
   Investigation of Laser Ablated Metal and Polymer Plasmas in Ambient Gas Using Fast Photography, Spect. Acta B **53**, (1998) 1919

3. R. K. Thareja, R. K. Dwivedi, A. Misra, A. Mitra and A. Neogi
   Deposition of Thin Films by Laser Ablation, Metals, Materials and Processes, **10**, (1998) 217

4. A. Misra, A. Mitra and R. K. Thareja
   Diagnostics of Laser Ablated Plasmas Using Fast Photography, Appl. Phys. Lett. **74**, (1999) 929

5. A. Misra and R. K. Thareja
   Laser Ablated Plasma for Deposition of Aluminum Oxide Film, Appl. Surf. Science **143**, (1999) 56

6. A. Misra, T. Srivastava and R. K. Thareja
   Optimization of Laser Ablated Aluminum Plasmas using Charge Collector, Int. J. Mod. Phys. **13**, (1999) xxxx

7. A. Misra and R. K. Thareja
   Laser Ablation Deposition of Metal Oxide/Nitride Films at Room Temperature, J. Appl. Phys. (Communications), Accepted (1999)

8. A. Misra and R. K. Thareja
   Investigation of Laser Ablated Plumes Using Fast Photography, IEEE trans. on Plasma Science , Submitted (1999)

9. A. Misra, H. D. Bist, R. K. Thareja, M. S. Navati and J. Narayanan
   Thin Film of Aluminum Oxide through Pulsed Laser Ablation: A Micro-Raman Study, J. Chem. Phys., Submitted (1999)

10. A. K. Saxena, R. K. Dwivedi, R. K. Thareja, R. Cowsik, R. Sarkar and A. Misra
    Laser Ablation Deposition of Thin Gold Film, Curr. Sci., Submitted (1999)

TABLE OF CONTENTS

LIST OF FIGURES

LIST OF TABLES

LIST OF SYMBOLS

A	Atomic number
A_1	Ion broadening parameter
A'', A'	Transition probabilities
a_o	Speed of sound
α_{1B}	Absorption coefficient
α^{-1}	Optical absorption depth
B	Constant
b	Number of photons
β	Damping constant
C	Constant
C_p	Heat capacity
c	Speed of light
D	Diffusion constant
D_r	Diffusion range
D_{1ff}	Thermal diffusivity
d	Distance between the target and collector
Δ	Thickness of the shocked region
ΔE_{mn}	Energy difference between upper and lower level
ΔH	Volume latent heat
ΔT	Rise in temperature
Δx_{th}	Thickness of the target material evaporated per pulse
δ	Mean free path
E	Energy of Explosion
E_p	Laser pulse energy
E', E''	Excitation energies of lower and upper levels
e^-	Electron
e	Electronic Charge
ε	Fraction of laser energy absorbed in plasma plume
ε_I	Ionization potential
F	Drag force
G, G_1	Constant
g_+, g_o	Statistical weight of ionic and neutral stages
g'', g'	Statistical weight of upper and lower level
γ_1	Ratio of specific heat capacities
h_p	Enthalpy
h	Planck's constant
I	Integrated intensity of Raman lines
I_L	Intensity of laser radiation
I_s'', I_s'	Intensity of upper and lower level
j	Current density
K_1	Constant
$\mathbf{k}$	Propagation vector
k_B	Boltzmann constant
L_s	Latent heat of sublimation
L_{th}	Thermal diffusion length
λ	Wavelength

λ_L	Laser wavelength
λ'', λ'	Wavelengths of various transition
M	Mass of neutral atom
M_f	Final mass
M_a	Mach number
M_o	Initial mass
m	Mass of atomic species
m_e	Mass of electron
N_D	Number of particles in a Debye sphere
N_T	Total number of ablated species
n	Number density
n_c	Critical density
n_e	Electron density
n_I	Density of ion
n_{1o}	Neutral flux
n_{1+}	Positive ion flux
ω	Laser frequency
ω_p	Plasma frequency
P	Pressure
P_o	Pressure of the undisturbed background gas
P_1	Pressure of the plasma
P_p	Power emitted by plasma
R	Displacement of plume front
R_a	Reflectivity
R_g	Gas constant
ρ	Density
ρ_o	Density of the undisturbed gas
ρ_1	Density of plasma
ρ_{sh}	Density of shocked region
q	Exponent
S	Irradiated surface area
T	Temperature
T_e	Electron temperature
T_o	Temperature of undisturbed gas
T_1	Temperature of plasma vapor
T_{su}	Surface temperature
T_{sh}	Temperature of the shocked region
T_{sl}	Transnational temperature
t	Time
t_{ei}	Electron-ion thermalization time
τ_L	Laser pulse duration time
t_p	Most probable time
u_o	Velocity of the undisturbed gas
u_p	Initial expansion velocity of the plasma
V_o	Volume of the undisturbed gas
V_1	Volume of the plasma
V_{max}	Maximum Velocity
$\overline{v}$	Velocity
v	Velocity of ensemble

v_P	Most probable velocity
v_f	Velocity of expanding plasma
v_{sh}	Velocity of shock
x	Distance moved by plume
X, Y, Z	Dimension of the expanding plasma
X_o, Y_o, Z_o	Initial orthogonal edges
X_{max}	Stopping distance
W	Electron impact parameter
Z_e	Average charge
z_i	Number of ions
ϕ	Work function

Chapter I

INTRODUCTION

Lasers, having proven useful in diverse areas such as high resolution spectroscopy, surface alloying, material processing (welding, hole drilling), thin films or microstructures deposition, elemental analysis of solid samples, biomedical applications such as laser surgery and structural studies of bio-molecules and laser based weapons are amongst the preferred choice of researchers, material scientists and engineers. The interaction of intense laser light with matter has been a topic of extensive research in the field of plasma and atomic physics for more than three decades [1]. The first experimental work was published by Honig and Woolston [2]. Ready [3] was the first to report about the temporal and spatial profile of the ablated plume of the ejected material using photographic technique. The first experimental demonstration of the laser ablation deposition of thin films was reported by Smith and Turner [4]. They ablated a variety of materials with a ruby laser and demonstrated that thin films can be grown on a suitably placed substrate. Lasers became ubiquitous in the eighties, picosecond systems became common and femtosecond systems emerged, tunable lasers were already available from ultraviolet to infrared, and with this the interest shifted from area of development of lasers to the area of laser based applications. During eighties and nineties the study of pulsed laser ablation has grown rapidly for its increasing number of applications [5-10]. The development of X-ray lasers has boosted the interest in lithography and biological imaging. Other developments include the laser-based accelerators [11], laser material processing [12], nanocrystals [13], laser annealing [14], surface modification [15], laser etching [16] and laser assisted chemical vapor deposition [17].

LASER MATTER INTERACTION

The process of laser matter interaction has been a subject of many theoretical [18-20] and experimental [10, 21-24] studies for many years now. Laser solid interaction depends strongly on laser and interaction parameters (laser wavelength, laser irradiance,

pulse width, irradiated spot size, angle of incidence etc.), material characteristics (composition, optical and thermal properties etc.) and environmental conditions (pressure, acceleration etc.) [8,19,25,26]. Depending on laser power and pulse duration the laser created plumes consist of atoms, ions in the highly excited states and clusters [27]. The characteristic features of the laser-ablated plumes such as temperature, density, velocity, pressure and forward directed nature mainly depend on laser irradiance [19] and surrounding ambient conditions. At low irradiance ($I_L < 10^6$ W/cm^2), only a rise in temperature by conduction below the surface with no change of phase is observed. However, at moderate ($10^6 \leq I_L \leq 10^{13}$ W/cm^2) and high irradiance ($I_L > 10^{13}$ W/cm^2), multi-photon ionization at the surface eventually leads to plasma formation. The absorption of the optical energy is via inverse bremsstrahlung process. The thermal effects resulting in the ablation of the material depends upon laser characteristics such as the laser fluence, laser focussed spot size, laser wavelength etc. [28]. Depending on the irradiance less than or greater than 10^8 W/cm^2, Laqua [29] showed that for irradiance lower than 10^8 W/cm^2 the emitted polyatomic species move with a velocity of 10^4 cm/sec. However, at higher irradiance, the temperature of the plasma is much higher than the boiling temperature of the material and the evaporated material i.e., atomic and ionic species move with velocities greater than 10^6 cm/sec.

To control the underlying processes in plasmas for various applications, it is necessary to understand the physics of laser ablation. It requires an understanding of the initial stages of the various processes involved during the laser-target interaction, evaporation, plasma formation and its subsequent expansion in the ambient atmosphere. The interaction of the laser beam with the target and with the gas cloud of the ablated material is the initiation process followed by absorption or partial reflection of radiation by the target surface. The threshold power density varies with the operating wavelength, because the absorptance of the target surface depends on the wavelength of the incident radiation. In the laser power density regime where a plasma plume can be produced from the target surface, the leading edge of the laser pulse is absorbed by the surface layer, heats it rapidly to vaporize the solid target. Since the target is a solid, a part of the absorbed laser power is expended into latent heat of fusion in addition to latent heat of vaporization [30]. The early vapor phase species interact with the incident laser pulse and get internally

excited subsequently getting ionized. Collisions among the particles lead to a rise in the temperature and pressure of the gas. However, thermal ionization leads to the production of charged species at all stages of laser heating. The process of evaporation and heating continues until the electron density of the partially ionized gas (plasma) becomes high enough for the heating of the gas by inverse bremsstrahlung process to begin. The inverse bremsstrahlung process heats primarily the electrons in the presence of the ions, resulting in free-to-free state transitions. It results in increasing the plasma temperature and consequently the electron density. At moderate to high laser power, the electron density of the plasma can attain a value sufficiently high so that the core of the plasma becomes opaque. This occurs when the frequency of the plasma oscillation, as given by $(n_e e^2/\pi m)^{1/2}$, become equal to the laser frequency. The laser beam is no longer able to penetrate the plasma and reach the target. Here n_e is the electron number density, e the electronic charge, and m the electron mass. The density corresponding to critical surface is called critical density, $n_c \sim 10^{21}$ $(cm^{-3})/\lambda_L^2$ (μm). Laser heating of the plasma continues indirectly by thermal conduction from the plasma and the critical region advances towards the laser, resulting in the expansion of the plasma plume towards the laser [31]. The heating rate of plasma increases sharply at high electron densities by both the linear process of inverse bremsstrahlung and non-linear processes that come into play. Multiple ionized, high kinetic energy species are produced [32]. The energetic particles escape from the plasma essentially at asymptotic velocities. The typical expansion velocities of $\sim 10^7$ cm/sec are estimated and are independent of the ambient gas species. The high temperature and density of the laser-produced plasma without any external confinement are a direct result of the extremely high rate of heating by the high peak power lasers. The interaction of the expanding plasma of metal with an ambient background gas has been a subject of interest for numerous theoretical and experimental works [33-35]. Neogi and Thareja [36] have numerically modeled laser matter interaction in presence of an ambient gas by modifying one-dimensional MEDUSA code. The studies are aimed at modeling various processes in space physics, plasma chemistry and hydrodynamics of plasma. The nature of the interaction between laser plasma and ambient gas depends upon parameters such as velocity of different ionic species, densities in the interaction region, ambient gas pressure,

etc.. Though the research in this field has been going on for several years, many effects of the laser beam interacting with a metallic surface in an ambient atmosphere are still to be satisfactorily explained. The same is true of interaction with polymers [37]. It has been shown [38,39] that when a laser radiation falls on the organic surface, two distinct processes result. There can either be etching due to photochemical processes at the site of irradiation, to a depth which can be controlled by the number of pulses and fluence of the laser beam or the material may both melt and etch due to thermal process [40]. It has been suggested that ablation via photodecomposition of organic substances occurs as a result of bond scission by multiphoton processes induced by laser photons [41]. Various diagnostic techniques [42,43] are used to get time resolved information about the fragments of polymer leaving the surface with supersonic speeds. The product analysis gives a broad distribution of fragments ranging from diatomic to high molecular weight products [44]. The ablation of polymeric materials using lasers find its use in microfabrication [45] and photolithography [46].

The laser-produced plasma from different targets has been extensively studied [33,34,47-49]. Emission spectra have been used to study laser ablation plasma of Mg, Mn and Ti etc. [50]. The ablation yields and threshold of Al, Sn and Ti as a function of incident laser energy and target translation rate using gravimetric analysis has been reported [51]. The angular variation of the kinetic energies of various ionic species of laser-ablated carbon has been investigated [52]. Angle resolved velocity distribution of neutral copper atoms created by UV laser ablation of polycrystalline copper foils has been reported as a function of laser fluence [53]. Intensities of both emission [54,55] and absorption lines [56,57] have been extensively used to qualitatively monitor the spatial variation of ions and neutrals within the laser-ablated plume. The line shapes of the emission lines are very sensitive to local plasma conditions such as temperature, pressure and electron density and hence are used to study the plasma parameters [34,58]. Stark broadened profiles of selected transitions to estimate electron density have been extensively used [34,56,59,60]. The influence of magnetic field on the laser-generated plumes is also being studied [61-65]. The significant changes in the laser-ablated plume have been investigated in varying magnetic field strengths [64,65]. Some of the recent applications of laser-ablated plasmas at moderate laser irradiances, includes source of X-rays [66], VUV continuum [67], highly charged ions

[68-70], generation of laser oscillations [71,72], understanding of hydrodynamics of plasma [73,74], modeling of various processes in space physics [75], and the studies of laser-plasma interactions in the presence of magnetic fields [76-84] to simulate astrophysical plasma.

DYNAMICS OF LASER-ABLATED PLASMAS

The plasma is an interesting object for study for two reasons. Firstly, the laser-induced plasma is becoming an important tool for industrial processes for thin film deposition and secondly for the study in three-dimensional dynamics of a compressive fluid. The propagation of the laser-ablated plume in an ambient atmosphere is a complex hydrodynamic problem. In the case of expansion in vacuum, the plume particles collide with themselves resulting in the observed angular distribution [85]. The direction of the laser-ablated plume and its angular spread depends on laser parameters, target parameters and ambient atmosphere [86]. In the case of expansion in an ambient atmosphere, collisions between the particles of the ambient gas and plume also take place, which attenuate and slow down the plume particles. Several theoretical investigations have been carried out in the past to understand the formation and evolution of the plasma [18,19]. In the presence of an ambient atmosphere, the hot vapor plasma interacts with the surrounding atmosphere in two ways. Firstly, the expansion of the high-pressure vapor drives a shock wave into the atmosphere, and secondly energy is transferred to the ambient atmosphere by thermal conduction, radiative transfer and heating by the shock wave [28]. The interaction between laser plasma and the ambient gas is also of interest as it provides information on collisional, collective and electromagnetic processes in astrophysical and laboratory plasmas. The nature of interaction is governed by the densities, relative velocity, temperature, ion composition etc. of the plasma and background gas. The importance of these processes in determining the subsequent plasma evolution also depends on irradiance, target vapor composition, ambient gas composition, pressure and laser wavelength.

The interaction of laser-ablated plasmas with the ambient atmosphere leads to

(a) Laser supported combustion waves,

(b) Laser supported detonation waves, and

(c) Laser supported radiation wave.

At low irradiance ($< 10^6$ W/cm^2) [28], laser-supported combustion waves are produced. Here the conduction dominates, the vapor/shocked gas forms a thin layer which transports energy efficiently by radiation. Only a weak shock wave results in such cases. At moderate irradiance ($10^6 < I_L < 10^{12}$ W/cm^2) [87], laser supported detonation waves evolve. In this case the shocked gas is just hot enough and begins absorbing the laser irradiation without requiring additional energy to be transferred from plasma. The laser absorption zone follows behind the shock wave and moves at the same velocity. At still higher irradiance ($> 10^{12}$ W/cm^2), the laser supported radiation waves results. In such cases before the formation of the region of shocked gas, the ambient gas is heated to temperatures where laser absorption begins and hence shock wave is formed. The exact nature of the plasma processes requires detailed qualitative data on the composition and dynamics of the plume evolution. Several theoretical models are available in the literature to describe the material removal from the solid surface by high/moderate power laser irradiation [87-90]. Ho et al [87] have numerically simulated the interaction of pulsed laser irradiation of nanosecond duration with a metal surface. The vapor phase consisting of neutrals, ions and electrons is modeled as a one-component (local thermal equilibrium) ideal gas. Using Monte-Carlo simulation Kools [91] studied the effect of elastic collisions between the target atom and low pressure gas on the kinetic energy and spatial distribution of the particles arriving at the substrate. There are reports on the study of the interaction of a hot expanding laser plasma with a low-density background gas [61,92,93]. Although the laser ablation in presence of a background gas is of significant interest due to its application to laser ablation deposition (LAD), the exact processes in ambient are rarely defined. Several authors [33-35,94,95] have experimentally investigated the motion of plume in different ambient gases at different pressures. The holographic interferometry has been used to investigate the expansion of the laser-ablated aluminum plumes [96]. The expansion was studied in vacuum and in argon gas at various pressures. A compressible gas dynamics model has been used for describing the development of shock discontinuity in the plume expanding in a background gas [97]. Using this model, the development of shock discontinuities in the plume of laser-ablated plume of metal vapor expanding in a gas has been reported [97]. Several other researchers [98-104] have used drag and shock models to explain the plume expansion. To define the region of occurrence of shock, Dyer et al. [105] studied

experimentally the effect of background gas pressure on the formation of shock and concluded that at high pressures the shock model described their experimental observations better. Geohegan [106] and Wanniarachchi et al [107] have shown that the drag model fits better for the expansion of plume at low background pressures. Study of pulsed laser-ablated plume in low ambient pressure of the order of a few mTorr is very important as they are generally used in LAD [108]. Since the high velocity of the shock can deteriorate the quality of the films on the substrate, it is important to have knowledge of the pressure and distance at which the shock formation takes place. Anan'in [92] have used fast imaging technique to investigate the dynamics of the laser-ablated species in an ambient gas. Dyer et al [105] have used the streak camera to image the laser-ablated polymide and PET films to study the expansion of the LAP both in vacuum and in air. The results show that at a pressures of P < 0.5 mbar the expansion approaches a free expansion as in vacuum, and the time dependent exponent is close to that predicted by an ideal blast model. One-dimensional imaging of laser induced fluorescence spectroscopy (1d-LIF) has been applied to investigate the dynamics of the non-emissive particles (YO molecules) during the ArF excimer laser ablation of $YBa_2Cu_3O_{7-\delta}$ in an ambient oxygen gas [107]. Buranov et al [84] have used the snowplow model [109] to explain the dynamics of plasma expansion. They also reported that the plasma front often tends to become unstable due to Rayleigh-Taylor instability [110]. Zerkle and Sappey [111] have reported the estimates of the ground state copper atom number density in a laser-ablated copper plasma plumes using Planar Laser-Induced Fluorescence (PLIF). The shock wave formed due to the interaction of ablated fragments with background oxygen gas has also been reported by Gupta et al [112], and its temporal evolution as a function of oxygen pressure has been shown to agree better with a planar than spherical model. The dynamics of the species ejected by excimer laser ablation of a BiSrCaCuO target in different gas environments has been studied by spatially resolved, optical emission spectroscopy [101]. It is shown that the expansion is dominated by the interaction of the ejected particles and the background gas atoms or molecules through collisional interactions rather than by the reactions in the gas phase. The time and space-resolved emission spectroscopy has been applied to investigate plasma dynamics during the laser evaporation of a graphite target [113]. Two stages of expansion are found in the generated plume, the first starts just after the laser irradiation and the second beginning

some time later depending on the nature and the pressure of the ambient gas. The two stages are discussed using a viscous drag model for the first one and a delayed ideal blast wave model for the second. The dynamics of the gas phase induced by excimer laser ablation of Ge has been investigated by Vega et al [114] by analyzing the light emitted by the plume. Two clusters of neutrals with different velocities are observed. The fast species, both neutral and ionized, are produced by the direct ejection from the target whereas the slower species (neutrals) are due to recombination of ions. Blackbody emission from ejecta following KrF-laser irradiation of Yba_2Cu_{7-x}(YBCO) and BN targets have been observed by Geohegan [115] using ICCD. The spectra are used to estimate temperatures of ejecta from both BN and YBCO targets when irradiated at 3.5 and 1.5 J/cm^2. The observed temperature is between 2200 and 3200 K. The dynamics of nanoparticle formation, transport and deposition by pulsed laser ablation of c-Si in 1-10 Torr He and Ar gases has been studied by imaging laser-induced photoluminescence and Rayleigh-scattered light from gas suspended 1-10 nm SiO_x particles [116]. Optical absorption and emission spectroscopy has been employed to simultaneously identify populations of both the excited and ground states of Y and Y^+. These are correlated with ICCD photographs of visible plume luminescence and ion fluxes recorded with fast ion probes. These measurements indicate that plume splitting in background gases is consistent with the scattering of target constituents by ambient gas atoms [99]. Thareja, Abhilasha and Dwivedi [117] have reported a peculiar double peak structure in laser produced carbon plasmas as it expands in the background gas. The structure is said to originate due to stratification of the plasma plume into slow and fast ion components at the interface where Rayleigh-Taylor instability occurs. Ion probes and charge collectors are also useful diagnostics for the flowing laser plasmas such as those used in LAP [118,119]. Dwivedi, Singh and Thareja [120] have studied the propagation of carbon plumes in argon atmosphere using langmuir probe. They have reported both the spatial and angle resolved analysis of plasma parameters as a function of argon gas pressure. Di Palma et al [121] have studied the formation, composition and gas dynamics of pulsed laser produced plasma plumes from an AlN target by spatially and temporally resolved optical spectroscopy.

LASER ABLATION DEPOSITION OF THIN FILMS

Last several years have seen a phenomenal growth of a large number of thin film deposition processes. Various thin film deposition techniques which have been reported include evaporation [122,123], sputtering [124,125], ion beam deposition [126-128], e-beam deposition [129], plasma enhanced chemical vapor deposition [130,131], laser induced chemical vapor deposition [132], molecular beam epitaxy [133] and laser ablation deposition [134] etc. Of all these available techniques, laser ablation deposition (LAD) technique is rapidly proving to be an effective method for the preparation of a variety of thin films due to its several potential advantages over other techniques. The technique is being used to deposit a variety of materials including metals, semiconductors, superconductors and insulators etc [12,13,134,135]. Many thin films of several metals, ceramics, ferroelectrics, metal and metal compounds, polymer, biological material, refractive material [134], semiconductors, high T_c superconductors and insulators have been deposited by laser ablation deposition technique [12,135]. Laser ablation deposition has been used extensively to obtain high quality metallic films irrespective of their optical properties. The deposition of various metallic films such as Cu, Al, Co, Fe, Pt, Ti [13,136,137] etc have been reported in the literature. However, the reports on the laser ablation deposition of gold are rare [138]. The success of LAD in fabricating high quality and high T_c superconducting thin films has tremendously enhanced the interest in the research and development in this area. Laser ablation deposition offers the following advantages over other conventional physical vapor deposition techniques:

1. It can be used to deposit the thin films of almost any material, irrespective of its optical properties [28] because under high power laser irradiation most of the materials turn optically opaque by an optical breakdown.

2. Compositional fidelity is often retained between the target material and the deposited film and hence is attractive for fabricating stoichiometric multicomponent films [139,140].

3. It offers very high instantaneous growth rate. Growth rate of pulsed laser deposited CuNi films as high as 800 nm/sec has been reported [141].

4. Deposition can be carried out even at relatively lower temperatures due to very high kinetic energies of the plasma species [142,143].

5. The process is relatively simple, inexpensive and free of contamination.

6. Possibility of obtaining high-density films with good adhesion due to the presence of energetic species during the deposition process.

7. The efficiency of the target used is superior compared to any other technique since a predominant amount of evaporated material is forward directed and can be collected with a high degree of efficiency.

8. The fabrication of multi-layers is fairly straightforward with rapid substitution of targets into the path of the laser beam. Some of the most complex integrated high-T_c component has recently been demonstrated by pulsed laser deposition [144].

There are, however, certain drawbacks associated with LAD [145,146]. Foremost of these are the formation of particulates [145], inhomogeneities of deposition rates resulting from Cos^p profile of the ablation plume, relatively small area of deposition etc. These problems arise not only from the material specific properties but also from the incomplete understanding of the control parameters. Although the results available on LAD seem to be exciting and the application of LAD is ahead of its comprehension, however, many of the results have been obtained by trial and error approach. In practice, the formation of good quality films is rather difficult as it requires the optimization of various processing variables such as laser irradiance, laser wavelength, laser pulse width, ambient pressure, target-substrate separation and substrate temperature simultaneously. Each of these processes plays a dominant role in defining the quality of the deposited films, the major role being of laser produced plasma [147]. In fact, the possibility of modifying the system geometry (target-substrate distance and orientation, laser spot shape and dimension etc.) and ambient gas parameters (pressure, atomic weight, temperature, flow velocity, reactive properties etc.) make LAD affordable technique for growing wide variety of thin films with excellent properties. It is therefore, necessary to understand the mechanism of laser-surface interaction both experimentally and theoretically.

Laser induced plasma at laser irradiance of ~ 10^8 - 10^9 W/cm^2 is mostly used for pulsed laser deposition of thin films e.g. high T_c superconductors [148,149], metallic films [150-152], polymeric films [153,154], microelectronics and optoelectronics [155], for production of clusters of aluminum [156], carbon [157], sodium [158] and copper [159], nanostructures [160], surface temperature measurements [161], and for diamond like

carbon (DLC) films [162,163]. In laser ablation deposition process, an intense laser beam vaporizes a solid target surface and a thin film is deposited onto a suitably placed substrate. The laser heating of the target surface plays a major role in the particle generation. The peak power density on the target reaches very high so the process involved in laser ablation is quite different from that in ordinary vacuum evaporation where the thermal equilibrium is maintained. The non-equilibrium nature makes laser ablation technique unique for thin film deposition. In general, LAD consists of various consecutive processes separated in space and time such as energy coupling to the target material, removal of the material from the target surface, transfer of the target material as vapor and/or plasma to the substrate via gas phase and the subsequent growth of thin film.

It has been shown by several investigators [102,104,105] that the expansion dynamics of the plume during initial stages of expansion remains unhindered by the environmental gas and resembles free expansion in vacuum. It is assumed that the initial density distribution for ablation in gas corresponds to that in vacuum if the number of collisions between plasma species and background gas atoms are negligible and it is true up to mean free path (δ) only. Hence, the background gas plays a role after the mean free path, given by

$$\delta = \frac{k_B T}{\pi r^2 P_o} \qquad (1.1)$$

where T is the temperature of the gas, P_o the gas pressure and r the sum of radii of the colliding partners. During the expansion of the plume, the pressure within the plume (P_1) decreases and approaches the pressure of the ambient gas (P_o) i.e.,

$$P_1 (X,Y,Z,t) = P_o . \qquad (1.2)$$

The distance at which eqn. (1.2) is satisfied defines the plume length, L_P given by [108]

$$L_P = \zeta \left[\frac{(\gamma_1 - 1)\varepsilon E_p V_1^{\gamma_1 - 1}}{P_o} \right]^{1/3\gamma_1} \tag{1.3}$$

where E_P is the laser pulse energy, ε the fraction of laser energy absorbed in the plasma plume, V_1 the initial volume of the plume, P_o the background gas pressure and ζ is a geometrical factor. The plume length is the distance beyond which the ambient gas can diffuse into the plume. The influence of target-substrate distance on the film quality has been studied by streak photography and emission spectroscopy [164]. Lembo et al [165] analyzed the plume fluorescence emission and ionic yield of laser ablation from a PZT target. The results indicated that the oxidation of the ablated material occurs during transport from target to substrate and in order to grow ferroelectric thin films the substrate should be located in the region of the plume where the relative concentrations of metal oxide increases.

Saengar [98] has reviewed a number of experimental findings. The effect of various parameters such as target surface topography, target substrate distance, dimensions of laser spot size and laser parameters viz., wavelength, fluence, pulse width on the plume angular distribution in vacuum has been discussed by her. Ong et al [166] have studied the effect of laser intensity on the deposition of DLC films using an ArF (193 nm) excimer laser. The presence of the ambient gas greatly influenced the deposited films. Ambient gas pressure in PLD process has been observed to significantly modify the lattice parameters of (1-x)SrTiO$_3$-xBaTiO$_3$ films. The variations in the oxygen content and the interdiffusion of species into the substrate during subsequent annealing treatments have been discussed [167]. Thareja, Dwivedi and Abhilasha [22] have deposited carbon films in the presence of helium and argon at various pressures and attempted to correlate their formation with the characteristics of laser produced carbon plasmas. Thickness and composition variation in the laser-deposited superconducting thin films and their effects on the microstructure development was investigated by Singh et al [168]. Kim et al. [169] have reported an ambient pressure- target substrate distance relationship for optimum quality films of YBCO and PLZT in oxygen atmosphere using blast wave theory. Ozegowski et al [170] used four different pulsed lasers to deposit and study the influence of the laser parameters on plasma

parameters and on the surface morphology of the deposited films. Gold films have been used extensively as an electrical conductor in integrated circuits and microelectronics industry because of their desirable properties for these applications such as resistance to oxidation, low electrical resistance and overall chemical inertness [171]. However, the major problem in thin gold films is its poor adhesion to various substrates [172]. Björmander et al [173] have grown ferroelectric/superconducting heterostructure on single crystal $LaAlO_3$ using Nd:YAG laser. They reported characteristics of coexisting superconducting and ferroelectric properties which have been achieved in laser deposited $PZT/YBCO/LaAlO_3$ heterostructures. Perovskite $La_{1-x}Ca_xMnO_{3-\delta}$ thin films were deposited by Gu et al. [174] on Mg (001) substrate and the films were analyzed for the effect of deposition conditions, such as laser fluence, substrate temperature and oxygen pressure on the growth behavior of films. Recently, thin films of carbon nitride were deposited by pulsed laser deposition technique and were characterized for chemical composition and atomic bonding using scanning Auger, x-ray photoelectron spectroscopy, and electron energy-loss spectroscopy. The effect of the growth parameters including substrate temperature, substrate bias, nitrogen partial pressure, and atomic nitrogen on the film composition were studied [175]. Pulsed laser deposition has been shown to be a promising technique for the thin films of oxide materials, particularly high T_c superconducting films [13], ferroelectric thin films [173] and various metal oxides [176] and nitrides [177]. The extent of their orientation depends upon the deposition process, i.e., in situ deposition at an elevated temperature or low temperature deposition followed by heat treatment. However, only a few reports are available for the deposition of films at room temperature [143,178]. In situ films deposited at high temperatures are in general, highly oriented (monocrystals) or epitaxial, but grain growth, low deposition rates, film cracking and uneven interfacial reactions result in rough surfaces [179]. On the other hand, films deposited at low temperatures reduce the problems associated with high temperatures but they undergo a change in structure and as a result are polycrystalline with a random distribution or slightly preferred orientation [179].

In 1969, Asmus et al [180] showed that the absorption of CO_2 radiation by thin film metallic foils increases when the measurements are performed in an oxygen rich environment. The effect was attributed to the laser-induced thermochemical reaction of

of oxygen with the surface atoms of the sample to form a thin oxide layer. Although the great majority of these films are insulating [135] but some films such as ZnO [181,182] are actually semiconductors. The most commonly applied laser method in metallic oxide formation is that of localized laser heating [183]. In this case, the chemistry is confined to those areas where the temperatures are sufficiently high. PLD has been extensively employed in preparation of high quality films of metallic oxides [176,184,185] and nitrides [143,186,187]. Moore et al [188] have demonstrated the photoassisted deposition of thin film aluminum oxide films from layers of trimethylaluminum (TMA), dimethylaluminum hydride, and aluminum hexafluoroacetylacetonate condensed with water on a cold substrate. The effect of laser irradiation of sapphire (single crystalline α-Al_2O_3) was studied by Cao et al [184]. He reported that the laser-melted material resolidifies as γ-Al_2O_3. Sato et al [189] has made a comparison of laser ablation deposited thin films of Al, C, Si and Cu. He found that the film of C were smooth, while other films were composed of many particles of 100 nm in diameter on average. Also, the films deposited by laser ablation of Al and Si contained oxygen. Since the success of the optical fiber amplifiers, rare earth doped optical materials for waveguides are being studied because of their potential application as planar optical amplifiers and lasers [190]. Serna et al [185] have grown and studied Al_2O_3 films doped in situ with erbium by pulsed laser deposition on a Si (100) wafer at room temperature in a single step process by alternate ablation from Al_2O_3 and Er targets. It has been shown that this technique allows designing a uniform and efficient dopant distribution through out the film thickness. Misra and Thareja [136] have deposited Al_2O_3 films on a silicon substrate at room temperature. They used 2-dimensional ICCD images of the ablated plumes to optimize the target substrate distance. Al_2O_3 films on oxidized Si substrates were implanted with Er ions having concentrations ranging from 0.01 to 1 atomic % by Van den Hoven et al [190]. Photoluminescence characterization of Er-implanted Al_2O_3 films showed that high Er concentration is achieved with only moderate concentration quenching effects. High quality epitaxial AlN layers were deposited by LAD process on sapphire substrates at 800°C and laser energy densities of 2-3 J/cm^2 for the first time by Vispute at al [187]. The XRD, UV-V spectroscopy, electrical resistivity, and TEM studies showed that by raising the substrate temperatures to 800°C and lowering of energy density of the laser to 2 J/cm^2 improved electrical properties, crystallinity and purity of exitaxial layers. This is one of the

first reports on the growth of high quality AlN films on sapphire by PLD. The earlier attempts on the deposition of AlN yielded polycrystalline [191,192] or amorphous microstructures [178]. Titanium-aluminum-nitride (TAN) electrode films were prepared by pulsed laser ablation on (100) Si and (100) MgO substrates for ferroelectric lead-zirconate-titanante (PZT) thin-film capacitors by pulsed laser deposition technique [193]. Dual supersonic molecular beam gas sources of triethylaluminum and ammonia were used to deposit single phase aluminum nitride (0001) on Si (100) substrates at a temperature of 700°C by Brown at al [194]. High crystalline quality epitaxial GaN films with thickness 0.5-1.5 μm have been grown directly on Al_2O_3 (0001) substrate by PLD [195]. The crystalline properties of these films were found to be comparable to those deposited by chemical vapor deposition and molecular beam epitaxy. Nearly oxygen free AlN thin film has recently been grown by pulsed laser deposition on Si substrate at a temperature of 600° C [196]. Optical second harmonic generation was observed in AlN films from ultraviolet to near infrared by Lundquist et al [197]. Near band edge transitions in AlN has recently been observed for the first time by luminscence emission spectroscopy [198].

Various techniques which are routinely used to characterize the laser-ablated films to get information on the surface stoichiometry, constituent content, thickness, and optical properties etc. are listed in Table 1.1.

THE PRESENT WORK

The work deals with the diagnostics and investigation of laser-ablated aluminum plasma in various ambient atmospheres. Various parameters of the plasma are estimated using fast photography. Based on the observations of image of LAP an attempt is made to optimize an important parameter, the target-substrate distance for thin film deposition. The films are characterized using several techniques and are presented in details.

Chapter II presents the quantitative analysis of the plasma plume produced off the target surface by focusing an intense laser pulse. The physics of interaction of the laser pulse with the target, evaporation of the target material, interaction of the laser beam with the evaporated material, expansion of the blow off material and finally deposition of the evaporated material as a thin film is presented.

Table 1.1

Different methods used for thin film characterization

Optical Characterization
— Absorption and Luminescence
— Raman Spectroscopy
— Infrared Spectroscopy

Electron Spectroscopy
— Photo Electron Spectroscopy
— Auger Electron Spectroscopy

Analytical Electron Microscopy
— Scanning Electron Microscopy
— Transmission Electron Microscopy
— Atomic Force Microscopy
— Scanning Tunneling Microscopy
— Electron Energy Loss Spectrometry
— Energy Dispersive X-ray Spectroscopy

Electrical Characterization
— Electrical Resistivity
— Electrical Conductivity

Ion Spectrometry and microscopy
— Secondary Ion Mass Spectrometry
— Rutherford Back Scattering

X-ray Analysis
— X-ray Diffraction
— X-ray Fluorescence

Magnetic Resonance Methods
— Internal Stress and Adhesion
— Hardness
— Frictional Coefficient and wear

Chapter III describes the experimental techniques developed in order to carry out the present studies. The aluminum plasma was characterized using optical emission spectroscopy and a charge collector. The optical emission from the plume was found to be dominated by various atomic/ionic species at moderate laser irradiances (10^8 - 10^{11} W/cm^2). Assuming local thermodynamical equilibrium (LTE), the electron temperature for Al II species was estimated using intensity ratio of emission lines. Stark broadened profiles of Al II transition (4p ^{1}P$^{\circ}$-4d ^{1}D) at 559.3 nm were used to calculate the electron density. The presence of an ambient gas increased the intensity of emitted spectra and hence resulted in increase of electron temperature. A charge collector was used to characterize the total ionic yield from the laser-ablated aluminum plasmas. Faraday cup was fabricated and used in time of flight mode for this work. Preliminary work on linear time of flight mass spectrometer (to be used for laser ablation studies) is also discussed.

The results on the investigation of laser-ablated aluminum plume using fast photography are discussed in Chapter IV. In order to study the dynamics of the laser-ablated plasma, the characteristic luminous plume is imaged at different time intervals with respect to the ablating pulse, onto an ICCD camera system. The continuity equation along with equations of motion are solved numerically to simulate the expanding front of a laser-ablated plume and is found to compare well with the recorded image of the plume. The recorded image is used to plot displacement-time curves, which in turn are used to calculate the velocity of the expanding plume front. Equations of hydrodynamics are used to calculate various plasma parameters such as plasma vapor density, pressure and temperature. The variation of each of the above parameter in various (Ar, He, N$_2$, O$_2$ and Air) ambient environments, delay time and laser energy are discussed in details. Classical drag and blast models are used to explain the dynamics of the experimentally observed expanding front. An empirical model based on the experimental observations is presented to describe the motion of plume in an ambient atmosphere. Stratification of the laser-ablated plasmas observed both in metals and polymers is explained on the basis of double vaporization from the target.

In Chapter V, the results on the deposition of laser-ablated aluminum oxide and nitride films at room temperature are presented. XRD, SEM, RBS, EDX and Raman spectroscopy are used to characterize the deposited films. The combined outcome of this

Chapter and characteristics of laser ablated plumes is the development of a technique to optimize the target-substrate distance, a vital parameter for the deposition of metal oxide/nitride and high T_c superconducting films.

Chapter VI summarizes the results of the present work.

Chapter II

LASER-ABLATED PLASMAS

The process of laser interaction with matter resulting in the formation of plasma is a subject of many theoretical [18-20] and experimental [10, 21-24] studies. The process can be categorized in three regimes, namely:

1. Evaporation regime, where the laser-target interaction and the evaporation of the target surface layer takes place.

2. Isothermal regime, the regime in which the laser-plasma interaction begins resulting in the formation of a high temperature expanding plasma.

3. Adiabatic regime, the regime defines the characteristic forward-directed expansion of the plume after the termination of laser pulse.

The first two regimes start with the laser pulse and continue until the laser pulse duration. The last regime starts after the termination of the laser pulse. A physical understanding of the dynamics of the vaporised plume is crucial to the process of deposition of thin films. Thus, it is important to study each of the three regimes separately.

LASER TARGET INTERACTION

The mechanisms responsible for the absorption of laser radiation, electron generation and subsequent plasma formation are:

a) Cascade Breakdown

In this process laser radiation is absorbed on collision of electrons with neutrals. If the electrons energy is sufficient they can impact ionize the gas or solid through the reaction

$$e^- + M \rightarrow 2e^- + M^+ .$$
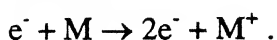
The concentration of electron increases exponentially with time leading to cascade breakdown. This process occurs provided there is an initial electron in the focal volume and electrons acquire energy greater than the ionization energy of the gas or band gap of the solid.

b) Multiphoton Ionization

The mechanism involves the simultaneous absorption by an atom or molecule of a sufficient number of photons to cause ionization or to raise an electron from the valance to the conduction band. The process can be described by an equation

$$M + bh\nu \rightarrow M^+ + e^-$$
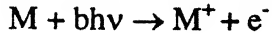
If ε_I is the ionization potential of the gas (or band gap for a solid) the number of photons b must exceed the integer part of $(\varepsilon_I / h\nu + 1)$. The ionization rate is proportional to I_L^b and the electron density, where I_L is the intensity of laser radiation. For constant I_L the ionization rate increases linearly with time. Multiphoton ionization is important only at short wavelengths ($\lambda < 1$ μm).

Both the mechanisms, cascade and multiphoton ionization require moderate irradiance ($\geq 10^8$ W/cm^2). However, breakdown of solids has been observed at irradiance as low as 10^6 W/cm^2 [21]. Absorption of radiation by the solid (either bulk or at impurity sites) causes its vaporization thus driving a shock into the surrounding air. Absorption of radiation by electrons in the vapor or behind the shock leads to heating of the vapor or shocked air. This leads to the generation of more thermal electrons and concurrently to a higher absorption rate.

At laser intensity $\sim 10^6$ W/cm^2, the absorbed radiation appears as heat which is evenly distributed through out the material by thermal diffusion. In case of metals the conduction electrons absorb the laser photons and are excited resulting in increase in their kinetic energy. The increase in kinetic energy of electrons can increase collision frequency which results in the rise in temperature of the surface of the material [199]. At slightly higher laser intensities ($> 10^6$ W/cm^2) depending on the thermal conductivity, thermal diffusivity, reflectively of the target material and the parameters of laser pulse, local heating of the surface increases and a molten pool of depth $(D_{iff}\tau_L)^{1/2}$ is formed [28], where D_{iff} is the thermal diffusivity and τ_L is the laser pulse duration time. If the optical absorption depth is much smaller than the thermal diffusion length, $\alpha^{-1} \ll L_{th}$ the absorbed energy is not appreciably diffusible from the surface region but is mostly used up to excite the atoms and particles leading to surface heating. A further increase in irradiation causes the surface temperature of the molten pool to reach boiling point resulting in evaporation. This will

happen when the energy deposited is approximately equal to the latent heat of sublimation [28] L_S (erg/gm) $= I_L \tau_L^{0.5} \rho^{-1} D_{iff}^{-0.5}$ where ρ is the density of solid target and I_L is the intensity of laser irradiation. Once the vapors are formed, the laser light causes further heating resulting in the formation of plasma. The removal of the material from the target surface by laser irradiation depends on the coupling of laser beam energy with the solid target.

The amount of material evaporated can be calculated using energy balance considerations. The energy deposited on the target by the laser beam is equal to the sum of energy needed to vaporize the surface layers, the conduction losses by the target and the losses due to absorption of the laser energy by plasma. The thickness of the target material evaporated per pulse (Δx_{th}) is given by

$$(1-R_a)[E-(\text{Conduction losses} + \text{Plasma losses})] = \Delta x_{th}[\rho_n C_p \Delta T + E \Delta H]$$

where R_a, ρ_n, C_p, ΔT and ΔH represents the reflectivity, density, heat capacity, temperature rise and volume latent heat of the target material respectively. Since $\Delta H \gg \rho_n C_p \Delta T$, it follows from above equation

$$\Delta x_{th} = (1 - R_a) \left[\frac{E - E_{th}}{\Delta H + C_v \Delta T} \right] \quad (\text{cm}) \qquad (2.1)$$

Here E_{th} is the laser energy threshold. This equation is valid for conditions where the thermal diffusion distance L_{th} [$= (2D\tau_L)^{1/2}$] is larger than the absorption length of the laser beam in the target material, α^{-1}. In eqn. (2.1), the energy threshold (E_{th}) depends on the laser wavelength, pulse duration, plasma losses and the thermal properties of the material. If the material parameters are independent of pulse energy density, a linear increase in evaporated material thickness as a function of pulse energy density is observed. However, a nonlinear behavior, especially at high energy densities, is observed due to the change in plasma losses and reflectivity of the laser beam. The evaporation flux is dependent on both the laser and material parameters which indirectly play an important role in the determination of plasma absorption coefficient.

Mechanisms of Plume Ionization

It follows from the previous section that the interaction of the high power laser beam with the bulk target leads to very high surface temperature resulting in the emission of positive ions and electrons from the target surface. The flux of the electrons can be estimated using Richardson equation,

$$j = BT^2 \exp(-\phi/k_B T) \tag{2.2}$$

and ions by Langmuir Saha equation

$$n_{i+}/n_{io} = (g_+/g_o) \exp[(\phi-\varepsilon_I)/k_B T] \tag{2.3}$$

where, j is the current density, ϕ the work function of the surface, T the temperature, k_B the Boltzmann's constant and B is a constant equal to 60.2 A cm^{-2}deg^{-2} for many metals. n_{i+} and n_{io} are, respectively, the positive ions and neutral species density leaving the surface at temperature T and g_+ and g_o are, respectively, the statistical weights of the ionic and the neutral states.

The plasma formation can mainly be ascribed to the following processes during the laser-vapor interaction, namely collisional excitation, collisional ionization, photo-excitation, photo-ionization and bremsstrahlung. Depending upon the wavelength and fluence of the laser radiation, inverse bremsstrahlung and/or photoionization dominate.

The dispersion relation for an electromagnetic wave travelling through a plasma is given by $\omega^2 - \omega_p^2 = k^2 c^2$, where ω_p is the plasma frequency, $\omega_P = (4 \pi n_e e^2 / m_e)^{1/2}$ Hz, c, the speed of light, **k**, the propagation vector and n_e is the electron density. For $\omega > \omega_p$, **k** is real and the propagation of electromagnetic wave take place whereas for $\omega < \omega_p$, **k** is imaginary and the wave is not propagated at all. At $\omega = \omega_p$, the reflection of laser light occurs at a density called the critical density, $n_c = [m_e\omega^2/4\pi e^2]$. Most of the absorption of laser energy occurs at or close to n_c. The laser light is absorbed in the plasma by an inverse bremsstrahlung process which is due to electron-ion collisions in the plasma. The absorption coefficient is given by,

$$\alpha_{IB} = 5.64 \times 10^{-11} \frac{Z_e n_e^2 \ln \Lambda}{\omega^2 T_e^{3/2}} \cdot \frac{1}{\left(1 - \frac{\omega_p^2}{\omega^2}\right)^{1/2}} \tag{2.4}$$

$$\text{and } \Lambda = \frac{3(k_B T_e)^{3/2}}{4(\pi n_e)^{1/2} e^3}$$

where, Z_e, n_i and T_e are respectively the average charge, ion density and temperature of the plasma, k_B and ν are the Boltzmann constant and the frequency of the laser light respectively, $\ln\Lambda$ stands for the coulomb logarithm which gives dynamical information about ion-electron collisions. For laser produced plasmas $\ln\Lambda$ takes on value between 5 and 10.

In an inverse bremsstrahlung process, if $\omega >> \omega_p$, the second factor in eqn. (2.4) may be taken as unity and the rate of absorption varies as n_e^2. The absorbed energy causes an increase in the kinetic energy of the electrons i.e. an increase in electron temperature and this in turn produces further ionization with a consequent increase in n_e. Hence the rate of absorption and with it the rate of ionization escalates so that n_e increases further and eventually approaches n_c, the critical density is established across a plane surface some distance into the plasma. The critical density corresponding to 1.06 μm radiation is approximately 10^{21} cm^{-3}. At a distance where the plasma attains the critical density, the plasma becomes opaque to the incoming radiation which causes laser light to get reflected. Laser light can no longer reach the target surface to generate new plasma. However, the plasma growth does not cease. Because of the heating due to the absorption of radiation by inverse bremsstrahlung, the plasma is driven rapidly away from the target surface resulting in the decrease in electron density and hence laser light again reaches the surface. These processes do not take place discontinuously but merge into a smooth self-regulating regime with the generation, heating and expansion of plasma taking place through out the laser pulse. Figure 2.1, shows the formation of laser-ablated plasma and different regions formed when a laser beam is incident on a planar solid target. The situation is analogous to rocket take off condition where the hot gas exhaust results into a net upward thrust.

The energy absorbed by the electron equilibrates very rapidly so that a well-defined electron temperature is reached. The energy gained by the electrons is also shared with ions in collision. The time required to attain equilibrium (the electron-ion thermalization time) is given by [200]:
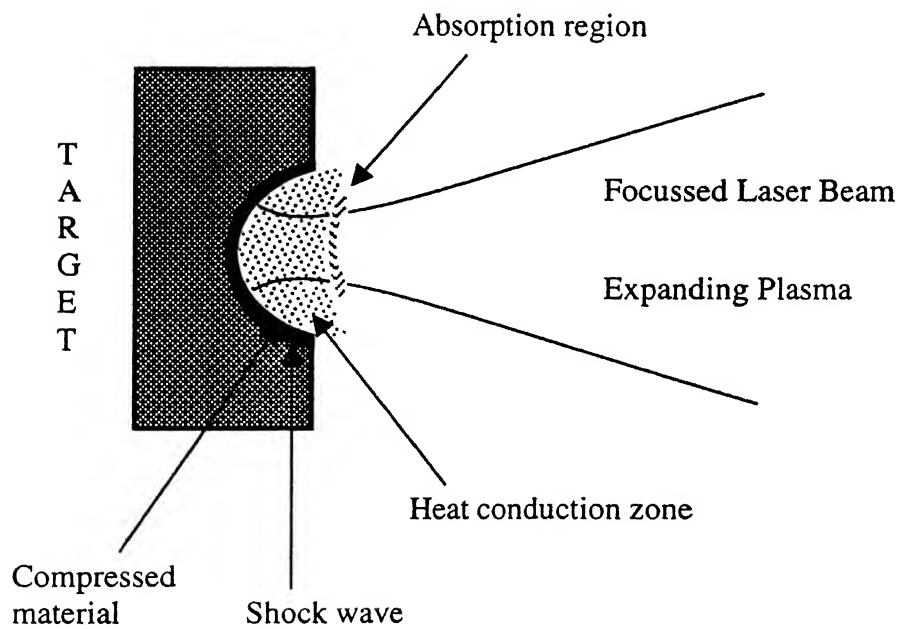
Fig. 2.1. Figure shows the schematic of a laser-ablated plasma formed when a laser beam is incident on a planar solid target

$$t_{ei} = 252 \frac{A T_e^{3/2}}{n_e Z_e^2 \ln \Lambda} \qquad (2.5)$$

If this time is considerably less than the duration of Q-switched pulse, then a good degree of thermalization is expected in plasma. The thermalization time for Al (A=27, $n_e \approx 10^{17}$, $T_e \approx 20,000$ K) is found to be of the order of picoseconds which is much less than the duration of a Q-switched pulse (nanoseconds) used. However, at higher irradiances ($>10^{12}$ W/cm^2) the laser-ablated plasma is heated to a very high temperature in a thin absorbing layer at the surface of the dense regime and has only a small optical thickness, the self regulating regime does not exist. Absorption becomes non-collisional and takes place via resonance mode conversion at critical density. These plasmas are used for studying dynamics of strongly coupled plasmas [201], short wavelength lasers [71,202] and simulating astrophysical like plasmas [201].

Plasma in an ideal thermodynamic equilibrium at a temperature T_e satisfies the following conditions: (a) all particles; electrons, neutral species and ions obey the Maxwell velocity distribution law, (b) the population distributions over the states of any atom or ion are given by the Boltzmann formula, (c) the number of ions in stage z_i relative to the number in stage (z_i-1) is given by the Saha equation, (d) the intensity distribution of the radiation in the cavity as a function of frequency and temperature is given by the Planck formula. A system is said to be in complete thermodynamic equilibrium if it follows all the conditions. Rarely, is a perfect thermodynamical equilibrium approached in case of laser-ablated plasmas. The commonest plasma model is the local thermodynamic equilibrium (LTE). In LTE it is assumed that collisional events, in particular the events involving electrons, determine the behavior of the system. These collisions are assumed to be governed by the same laws as that hold in thermodynamic equilibrium. Thus if an electron temperature T_e is defined and electron velocity distribution is defined in terms of T_e then the populations in excited states and various stages of ionization are given by the Maxwell velocity distribution, the Boltzmann formula and the Saha equation. The radiation distribution is, however, not given by Planck's equation and the radiation effects are assumed to play an insignificant role in determining the equilibrium in the plasma.

ISOTHERMAL REGIME

Because of the high expansion velocities of the leading plasma edge, the electron and ion densities decrease very rapidly with time, making the plasma transparent to the laser beam for larger distances (away from the target surface). As the plasma is constantly augmented with evaporated particles at its inner edge adjacent to the target surface, a thin region near the surface is constantly absorbing the laser radiation during the time interval of laser pulse. A schematic diagram of the laser interaction with the plasma-target is shown in figure 2.2. The figure shows that the four separate regions can be distinguished (i) unaffected bulk target, (ii) evaporating target surface, (iii) area near the surface absorbing the laser beam and (iv) rapidly expanding outer edge which is transparent to the laser beam.

The bremsstrahlung process is responsible for maximum radiative loss in the laser-ablated plasma and the emitted power in Watt/unit volume is given by

$$P_p = 1.42 \times 10^{-34} Z_e^3 \, n_e^2 \, T_e^2$$

For the case of laser-ablated aluminum plasma $Z_e = 1$, $n_e \sim 10^{16}/cm^3$, $T_e \sim 20,000$ K and the volume [$= u_f \tau_L S$], where u_f is the initial expansion velocity ($= 10^6$ cm/sec), τ_L is the laser pulse duration (8 ns) and S is the irradiated area ($\sim 5.31 \times 10^{-8}$ cm^2)], the emitted power is of the order of 2 Watt, which is very small compared to laser pulse power ($= 10^9$ Watt). As a consequence of the small value of τ_L, the plume is uniformly heated and due to negligible loss the first step of the expansion process can be taken as isothermal. A dynamic equilibrium exists between the plasma absorption coefficient and the rapid transfer of thermal energy into kinetic energy. At higher energy densities when the plasma absorbs an appreciable amount of energy, a self-regulating regime may exist near the target surface. It has been shown that the density, temperature, and dimension of the plume adjust in such a manner that the plasma absorbs same amount of laser radiation to maintain self-regulating regime [19]. During the isothermal regime the power absorbed by plasma is distributed uniformly over its entire mass. This is valid for laser produced plasmas where the thermalization time is significantly smaller than the plasma expansion time which results in the establishment of a uniform temperature in the plasma. Thus, in this regime the plasma is in isothermal state, continuously absorbing the laser radiation and expanding outwards isothermally. This region is constantly augmented with particles evaporated from the target
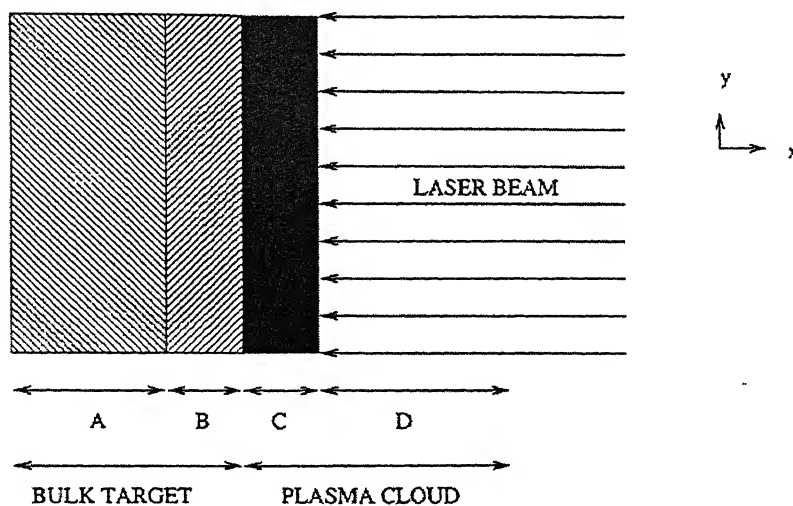
A = Uneffected Target

B = Evaporated Target Material

C = Dense Plasma Absorbing Laser Radiation

D = Expanding Plasma Outer Edge Transparent
      To The Laser Beam.

Fig. 2.2. Schematic diagram showing different phases during
laser interaction with target

surface. The rapid expansion of the plasma in vacuum results from large density gradients.

The plasma which is absorbing laser energy can be simulated as a high temperature and high pressure gas initially confined in a small volume which is suddenly allowed to expand in vacuum/ambient atmosphere. Because of the large pressure gradients initially present near the outer edge (vacuum), very high expansion velocities are induced at this edge. In the initial stages of the plasma expansion when the particle density is high the mean free path of the particle is short and hence the plasma behaves as a continuum fluid. The following equations of gas dynamics can thus be used to simulate its expansion,

$$\frac{\partial n}{\partial t} + \nabla.(n\overline{v}) = 0 \qquad (2.6)$$

$$nm\left(\frac{\partial \overline{v}}{\partial t}\right) + (\overline{v}.\nabla)\overline{v} = -\nabla P \qquad (2.7)$$

where n is the number density, $\overline{v}$ the velocity and P the pressure. For the duration of the laser pulse the plasma temperature can be taken to be constant i.e., the expansion is an isothermal one. The density (n) of plasma at any point (x, y, z) at time t can be expressed as a Gaussian function given by [19]

$$n(x, y, z, t) = \frac{N_T t}{\sqrt{2\pi}^{15}\tau_L X(t)Y(t)Z(t)} \exp\left[-\frac{x^2}{2X(t)^2} - \frac{y^2}{2Y(t)^2} - \frac{z^2}{2Z(t)^2}\right]$$

$$(2.8)$$

where N_T is the total number of ablated species at $t = \tau_L$ (pulse width). X(t), Y(t) and Z(t) are the dimensions of the expanding plasma in the three orthogonal directions and correspond to the distances at which the plasma density decreases to 60.65 % of the maximum density. Assuming plasma to be an ideal gas, the pressure at any point can be expressed as

$$P(x, y, z, t) = n(x, y, z, t)R_g T_1 \qquad (2.9)$$

where T_1 is the isothermal temperature of the plasma and R_g the gas constant. It has been shown that gas dynamic equations follow similarity transformation [203] in which the velocity can be expressed as

$$\overline{v} = \frac{x}{X(t)}\frac{dX(t)}{dt}\hat{i} + \frac{y}{Y(t)}\frac{dY(t)}{dt}\hat{j} + \frac{z}{Z(t)}\frac{dZ(t)}{dt}\hat{k} \qquad (2.10)$$

where $\dfrac{dX}{dt}, \dfrac{dY}{dt}$ and $\dfrac{dZ}{dt}$ refer to the expansion velocities of the plasma edges X, Y, and Z

respectively. Substitution of equation (2.8) in (2.10) gives

$$X(t)\left[\frac{1}{t}\frac{dX}{dt} + \frac{d^2X}{dt^2}\right] = Y(t)\left[\frac{1}{t}\frac{dY}{dt} + \frac{d^2Y}{dt^2}\right] = Z(t)\left[\frac{1}{t}\frac{dZ}{dt} + \frac{d^2Z}{dt^2}\right] = \frac{k_B T_1}{m}, \qquad t < \tau_L$$

$$(2.11)$$

where m corresponds to the mass of atomic species. The above equation determines the initial expansion in the three orthogonal directions. The initial dimensions of the plasma are of the order of mm in the transverse direction whereas in the perpendicular direction they are less than 1 μm. Equation (2.11) shows that during initial expansion stages when the velocities are small the acceleration is very high. With the increase in expansion velocity, acceleration starts to decrease and ultimately becomes zero resulting in an elongated shape of plasma. Since the plasma dimensions are much smaller along the target normal than in the transverse direction the expansion is anisotropic.

ADIABATIC EXPANSION

After the termination of the laser pulse, no particles are evaporated or injected into the inner edge of the plasma. The thermal energy rapidly gets converted into kinetic energy giving higher expansion velocity of the plasma. The adiabatic equations of state are

$$P\left[X(t)Y(t)Z(t)\right]^{\gamma_1} = \text{constant} \qquad (2.12.a)$$

$$T_e\left[X(t)Y(t)Z(t)\right]^{\gamma_1 - 1} = \text{constant} \qquad (2.12.b)$$

where γ_1 is the ratio of the specific heat capacities at constant pressure and volume and T_e corresponds to the plasma temperature. In adiabatic expansion regime, the velocity of the plasma increases due to a decrease in thermal energy of the plasma. As there is no injection of particles in the inner edge of the plasma, the density and pressure gradients can be expressed in a form similar to eqn. (2.8) and (2.9) by neglecting the term (t/τ_L) which takes into account the injection of particles into the plasma. The density (n) and pressure (P) in the plasma can be expressed as

$$n(x,y,z,t) = \frac{N_T}{\sqrt{2}\pi^{1.5}X(t)Y(t)Z(t)} \times \exp\left[-\frac{x^2}{2X(t)^2} - \frac{y^2}{2Y(t)^2} - \frac{z^2}{2Z(t)^2} \right] \qquad t \geq \tau_L$$

(2.13)

$$P(x,y,z,t) = \frac{N_T k_B T_1}{\sqrt{2}\pi^{1.5}X(t)Y(t)Z(t)} \times \exp\left[-\frac{x^2}{2X(t)^2} - \frac{y^2}{2Y(t)^2} - \frac{z^2}{2Z(t)^2} \right] \qquad t \geq \tau_L$$

(2.14)

The equations of the gas dynamics are the same as in the isothermal regime except that the equation of energy and adiabatic equation of state need to be solved. Differentiating eqn. (2.12.a) and (2.12 b), we get the adiabatic equation of state,

$$\frac{1}{P}\left[\frac{\partial P}{\partial t} + \overline{v}.\nabla P \right] - \frac{\gamma_1}{n}\left[\frac{\partial n}{\partial t} + \overline{v}.\nabla n \right] = 0 \qquad (2.15)$$

and the equation of temperature is given by

$$\frac{\partial T}{\partial t} + \nabla.\nabla T = (1 - \gamma_1)T\nabla.\overline{v} \qquad (2.16)$$

We have assumed that there are no spatial variations in the plasma temperature, so second term will be zero. Substituting the velocity, density, and the pressure equation into the differential equations the solution, which controls the expansion of plasma is given by

$$X(t)\left[\frac{d^2X}{dt^2} \right] = Y(t)\left[\frac{d^2Y}{dt^2} \right] = Z(t)\left[\frac{d^2Z}{dt^2} \right] = \frac{k_B T_1}{m}\left[\frac{X_0 Y_0 Z_0}{X(t)Y(t)Z(t)} \right]^{\gamma_1 - 1} \qquad t \geq \tau_L$$

(2.17)

where X_0, Y_0 and Z_0 are the initial orthogonal edges of the plasma after the termination of the laser pulse ($t>\tau_L$). The above equation shows that acceleration of the plasma species depends upon the temperature and dimensions of the plasma and the mass of the species.

LASER-ABLATED PLASMA IN THE PRESENCE OF AN AMBIENT GAS

When a laser–ablated plasma flows into an ambient media interstreaming plasma interactions, much like those found in many space and astrophysical situations occur [28]. At low background gas pressure ($p<10^{-2}$ Torr) a large fraction of ions stream through the background gas depositing very little of their energy. Whereas at higher pressure ($p>10^{-2}$

Torr) of the ambient gas essentially all the kinetic energy of the ions is lost in collisions with the background gas particles that occur within a very small volume near the target resulting in shock/blast waves [203,204]. The interaction of laser-plasma with the ambient gas results in recombination interactions, collisional and collision-less interactions, shock/blast wave interactions, micro-instabilities and turbulent interactions etc..

Shock Waves

We will now concentrate on the motion of the plume front along the Z-axis in an ambient atmosphere. Before we start looking at the plume dynamics it is essential to identify the following boundaries, namely: the contact front or the expansion front, compressed front and the shock front. In the present context the plasma pushes and compresses the ambient gas in front of it. It acts as a piston and almost all the ejected particles are concentrated near the boundary called the contact front or the expansion front (this front is dynamic). A thin region in front of the contact surface is compressed between the piston and the ambient atmosphere and is termed as compressed front. The region between the driven gas and the ambient gas is the shock front. A shock wave is a discontinuity formed near the leading edge of the plume when the surrounding gas is distinctly pressed by the ablated species. Figure 2.3 gives a schematic of the expanding plasma in an ambient atmosphere. The expansion of plume in vacuum shows an angular distribution due to collision of particles among themselves. However, in case of an expansion in an ambient atmosphere collisions between the particles of the ambient gas and the plume particles also take place which attenuate and slow down the plume front.

If we consider our expansion to be conical at earlier times with vertex at the focusing point of the laser beam and spherical at later times, the shock thickness can be approximately calculated by considering that entire mass of the gas encompassed by the shock wave is concentrated in a thin layer behind the front surface, the density inside the layer being constant and equal to the density behind the front $\rho_s = \rho_o \left(\dfrac{\gamma_1 + 1}{\gamma_1 - 1} \right)$. The thickness Δ of the shock is determined from the conservation of mass. The initial mass M_o and the final mass M_f are given by, $M_f = 4\pi R^2 \Delta \rho_s$ and $M_o = \dfrac{4}{3} \pi R^3 \rho_o$ for spherical
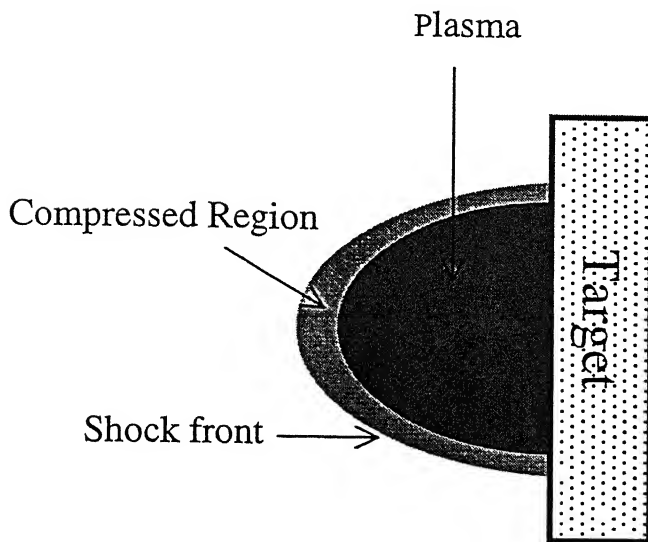
Fig. 2.3. Schematic of various regions formed during the expansion of a laser-ablated plasma in an ambient atmosphere

expansion, and $M_f = C\{(R +\Delta)^3 - R^3\}\rho_s$ and $M_o = C R^3 \rho_o$ for conical expansion, where C is a constant taking care of geometrical factor. Thus Δ is given by [91,205];

$$\Delta = \begin{cases} R\left[\left(\dfrac{2\gamma_1}{\gamma_1 +1}\right)^{1/3} -1\right] & \text{for conical expansion} \\[4em] R(\gamma_1 -1)/3(\gamma_1 +1) & \text{for spherical expansion.} \end{cases} \qquad (2.21)$$

γ_1 the specific heat ratio of the vapor (1.2-1.3) [203], and R is the position of the expanding front. The density, pressure and temperature in the shocked region can be estimated by applying the laws of conservation of mass, momentum and energy. The velocity and temperature of the shocked region are given by [204]:

$$v_{sh} \approx \left(\frac{\gamma_1 +1}{2}\right) v_f$$

$$T_{sh} = \frac{2\gamma_1}{\gamma_1 +1}\left[\frac{(\gamma_1 -1)}{(\gamma_1 +1)}M^2 +1\right] T_o \qquad (2.22)$$

where v_s is the velocity of the shocked region, v_f the velocity of the expanding plume front, M is the Mach number ($=v_f/a_o$), v_f (can be estimated from R-t plots) the velocity of the expanding front, T_o the background gas temperature, ρ_{sh} the density of the shocked region and ρ_o is the density of the ambient gas at NTP. From the values of temperature and density of the shocked gas, the extent of diffusion can be estimated. The diffusion coefficient (D) [102] and diffusion range (D_r) [102] are being given by

$$D = D_o (T_s/T_o)^{5/4}(\rho_o/\rho_{sh}) \qquad (2.23)$$

$$D_r = (4Dt)^{1/2}. \qquad (2.24)$$

In order to evaluate the plasma parameters (P_1, V_1, ρ_1) in terms of known parameters of undisturbed gas (P_o, V_o, ρ_o), the law of conservation of mass can be expressed as [203,204],

$$\rho_1 u_1 = \rho_0 u_0 \qquad (2.25)$$

The law of conservation of momentum, as

$$P_1 + \rho_1 u_1{}^2 = P_o + \rho_o u_o{}^2 \qquad (2.26)$$

and the law of conservation of energy (in terms of specific enthalpy), as

$$h_{p1} + u_1{}^2/2 = h_{po} + u_o{}^2/2 \qquad (2.27)$$

where P denotes the pressure, u the velocity, ρ the density, ε the internal energy and $h_p = \varepsilon + P/\rho$ the enthalpy of the system. Here the subscript o and 1 denote the undisturbed gas and plasma region (vapor) respectively. Knowing the thermodynamic properties of the gas (P_o, ρ_o) ahead of the plasma and assuming that the value of velocity of plasma particles creating the shock wave is known, remaining variables can be calculated.

Eliminating ρ_o and ρ_1 from eqn. (2.26), we get

$$u_o^2 = V_o^2 \left(\frac{P_1 - P_o}{V_o - V_1} \right) \qquad (2.28)$$

$$u_1^2 = V_1^2 \left(\frac{P_1 - P_o}{V_o - V_1} \right) \qquad (2.29)$$

where $V_o/V_1 = u_o/u_1$, where V_o and V_1 are the specific volumes. Using (2.28) and (2.29) in (2.27) we get,

$$h_{p1} - h_{po} = \tfrac{1}{2} (P_1 - P_o)(V_o + V_1) \qquad (2.30)$$

eqn. (2.30) is termed as shock adiabatic or the Hugoniot relation. Substituting

$$h_p = C_p T = PV\gamma_1/(\gamma_1 - 1) \qquad (2.31)$$

in eqn. (2.31) gives

$$\frac{P_1}{P_o} = \frac{(\gamma_1 + 1)V_o - (\gamma_1 - 1)V_1}{(\gamma_1 + 1)V_1 - (\gamma_1 - 1)V_o}, \qquad (2.32)$$

$$\frac{V_1}{V_o} = \frac{(\gamma_1 - 1)P_1 + (\gamma_1 + 1)P_o}{(\gamma_1 + 1)P_1 + (\gamma_1 - 1)P_o}, \qquad (2.33)$$

and

$$\frac{T_1}{T_o} = \frac{P_1 V_1}{P_o V_o} \Rightarrow \frac{\rho_1}{\rho_o} = \frac{V_o}{V_1} = \left(\frac{\gamma_1 + 1}{\gamma_1 - 1} \right) \qquad (2.34)$$

For a strong shock wave, $P_1/P_2 \gg 1$ and $V_1/V_o \approx (\gamma_1 - 1)/(\gamma_1 + 1)$. Also, $a_o^2 = (\partial P/\partial \rho)_s = \gamma_1 (P/\rho) = \gamma_1 PV$ we get

$$P_1 = 2\rho_o\ u_1^2\ /(1 + \gamma_1) \qquad (2.35)$$

$$T_1 = P_1/(R_g \rho_1) \qquad (2.36)$$

where a_o is the speed of sound and R_g the gas constant.

Now we discuss the plume dynamics in case of expansion into the ambient gas based on two existing models viz. Classical drag [99,102,104,106] and Blast [102,104,203] model.

Drag Model

In order to define the finite propagation of the plume in an ambient atmosphere, we consider the ablated particles to be an ensemble assumed to move in the forward direction with a force due to its internal pressure $(\partial P / \partial x)\partial V$, the net force in X-direction becomes

$$\rho_o F_x dV - \left(\frac{\partial P}{\partial x}\right) dV = \left(\frac{\partial v_x}{\partial t}\right)\rho_o dV \qquad (2.37)$$

similarly, for Y and Z directions. The equation of motion (eqn.2.7) becomes

$$\frac{\partial v}{\partial t} + (v.\nabla)v = F - \left(\frac{1}{\rho_o}\right)\nabla P \qquad (2.38)$$

Introducing the drag force $F = -\beta v$ in the above equation and taking only X component, here, v is the speed of the ensemble and β the damping coefficient, we get

$$\frac{\partial v_x}{\partial t} + v_x \frac{\partial v_x}{\partial x} = -\beta v_x - \frac{k_B T}{\rho_o m}\left(\frac{\partial \rho_o}{\partial x}\right) \qquad (2.39)$$

where $\overline{v}(x, y, z, t) = \hat{i}v_x + \hat{j}v_y + \hat{k}v_z$

Assuming Maxwell-Boltzmann distribution, the density is given by

$$\rho_o = G \exp\left[-\frac{m\left(v_x^2 + v_y^2 + v_z^2\right)}{2k_B T}\right] \qquad (2.40)$$

where G is a constant, on substitution of ρ_o in equation (2.39), we get

$$\frac{\partial v_x}{\partial t} = -\beta v_x \qquad (2.41)$$

$$\therefore \qquad \int \frac{\partial v_x}{v_x} = -\int \beta \partial t \qquad (2.42)$$

applying boundary condition, at t=0, $v_x = v_o$, we get

$$v_x = v_o \exp(-\beta t) \qquad (2.43)$$

since $v_x = dx/dt$, we can write

$$\frac{dx}{dt} = v_o \exp(-\beta t)$$ (2.44)

Integration of eqn. (2.44) gives

$$x = \frac{[v_o \exp(-\beta t)]}{-\beta} + G_1$$ (2.45)

On applying boundary conditions; at t=0, x = 0, we get $G_1 = v_o/\beta$, eqn. (2.45) reads

$$x = X_{max}[1-\exp(-\beta t)]$$ (2.46)

where $X_{max} = v_o/\beta$, and is referred to as the maximum distance to which a plume can expand in an ambient atmosphere.

Eqn. (2.45) shows that plume progressively slows down and eventually comes to rest due to the drag force (at a place where the ambient pressure equals the plume pressure). The distance from the target at which the propagation of the plume ceases is called the stopping distance or plume length.

Blast Wave Model

Consider a perfect gas with constant specific heats and density ρ_o in which a large amount of energy E is liberated in a small volume (a point explosion) during a short time interval. A shock wave will propagate through the gas starting from the point where the energy is released [203]. We shall consider the process at a stage when the shock wave has moved through a distance which is extremely large in comparison with the dimensions of the region in which the energy was originally released, i.e., the mass of gas set in motion by the explosion is large in comparison with the mass of the explosion products. In the case of a laser beam ablating a target, the energy released can be assumed to be both instantaneous and occurring at a point, focussed spot. We shall also assume that this stage of the process is sufficiently early that the shock wave has not moved too far away from the source so that its strength is still sufficiently large. Thus we can neglect the initial gas pressure or counter pressure P_0 in comparison with the pressure behind the shock wave. This is equivalent to neglecting the initial internal energy of the gas which has been set in motion in comparison with the explosion energy E and disregarding the initial speed of sound a_o, in comparison with the velocities of both the gas and the wave front.

The gas motion is determined by two-dimensional parameters, the energy of the explosion E and the initial density ρ_o. These parameters cannot be combined to yield scales with dimensions of either length or time. Hence, the motion will be self-similar, that is, will be a function of a particular combination of coordinate r_a (distance from the center of the explosion) and the time t. The initial speed of sound a_o cannot be used to characterize the process; whenever $P_o = 0$ in a particular approximation, a_o will be equal to zero to the same degree of approximation. This condition determines the limits of applicability of the solution. We impose specific requirements on the accuracy of the solution by comparing the pressure P_1 behind the wave front and the propagation velocity of the shock wave v_{sh}, with P_o and a_o, and find the time when the approximation $P_1 \gg P_o$ is no longer satisfied. It should be noted, however, that the condition for neglecting the counter pressure is $P_1 \gg [(\gamma_1+1)/(\gamma_1-1)]P_o$. With this condition the density ratio across a shock wave is equal to its limiting value $(\gamma_1+1)/(\gamma_1-1)$. Hence the quantity r_a/t cannot serve as the similarity variable. In this case, the only dimensional combination which contains only length and time is the ratio of E to ρ_o, with the dimensions $[E/\rho_o] = [cm^5 \, sec^{-2}]$. Hence the dimensionless quantity

$$\xi = r_a \left(\frac{\rho_o}{Et^2} \right)^{1/5} \qquad (2.47)$$

can be taken as a similarity variable.

The shock front is described by a given value of the independent variable ξ_o. The motion of the wave front R(t) is defined by

$$R = \xi_o \left(\frac{E}{\rho_o} \right)^{1/5} t^{2/5} \qquad (2.48)$$

The propagation velocity of the shock wave becomes

$$v_{sh} = \frac{dR}{dt} = \frac{2}{5}\frac{R}{t} = \xi_o \frac{2}{5} \left(\frac{E}{\rho_o} \right)^{1/5} t^{-3/5} = \frac{2}{5}\xi_o^{5/2} \left(\frac{E}{\rho_o} \right)^{1/2} R^{-3/2} \qquad (2.49)$$

We can express the parameters behind the front in terms of its velocity using the limiting formulas for a strong shock wave, viz;

$$\acute{\rho}_1 = \rho_o \left(\frac{\gamma_1 + 1}{\gamma_1 - 1} \right), \qquad P_1 = \frac{2}{\gamma_1 + 1} \rho_o v_{sh}^2, \qquad u_1 = \frac{2}{\gamma_1 + 1} v_{sh}. \qquad (2.50)$$

The density behind the wave front stays constant and is equal to its limiting value. The temporal dependence of pressure is

$$P_1 \sim \rho_o v_{sh}^2 \sim \rho_o \left(\frac{E}{\rho_o} \right)^{2/5} t^{-6/5} \sim \frac{E}{R^3}. \qquad (2.51)$$

The above model is restricted between two extremes i.e., in a range of R beyond which the model breaks down. The first limit requires that the mass of the gas encompassed by the shock wave ($\approx 2/3 \pi R^3$) is much greater than the initial explosion mass (M_o) i.e.,

$$R >> R_1 = (3M_o/2\pi\rho_o)^{1/3} \qquad (2.52)$$

The second limit requires that the pressure driving the front (P_1) is much greater than that ahead of the propagation (P_o) of the explosion front i.e.,

$$R_2 = (E_o/P_o)^{1/3} \qquad (2.53)$$

Thus the model is expected to hold for $R_1 << R << R_2$

$$\text{or} \qquad (3M_o/2\pi\rho_o)^{1/3} << R << (E/P_o)^{1/3} \qquad (2.54)$$

In general terms, the shock model eqn. (2.43) can be written as

$$R = K_1 t^q, \qquad (2.55)$$

where, K_1 is a constant, q an exponent and has a value of 0.4 for ideal shock condition and 1 for free expansion.

To conclude, in this Chapter we have discussed the basic mechanisms of laser ablation leading to the formation of hot plasma. The dynamics of the laser-ablated plume expanding in an ambient environment using hydrodynamic equation is presented. Expansion of the laser-ablated plumes in an ambient atmosphere is discussed in the light of shock and drag models.

Chapter III

EXPERIMENTAL TECHNIQUES

An overview of laser-ablated plasmas is presented in Chapters I and II. An extensive study was undertaken on the propagation of laser-ablated plasmas in vacuum and in presence of air, nitrogen, helium, argon and oxygen at low and moderate laser irradiance. These studies form the basis of optimizing one of the most important parameters, the target-substrate distance for the deposition of various metal-oxide [136, 176,206] and metal-nitride films [143]. In the work presented, we deposited metal-oxide and metal-nitride films on silicon substrate [136, 143], and characterized them using XRD [207,208], SEM [209-213], RBS [214] and Micro-Raman [215,216]. This Chapter describes various experimental techniques developed/used for the work presented.

A Q Switched Nd:YAG laser (Spectra Physics, DCR-4G) was used to produce plasma for laser ablation studies. It delivers 1 J in 2.5 and 8 ns (FWHM) pulse at fundamental ($\lambda = 1.064$ μm) with a repetition rate of 10 pulses per second. The laser has a Gaussian limited mode structure, the beam divergence being less than 0.5 mrad. The energy of the laser was monitored both by using conventional method of reflecting a part of the laser beam on a calibrated photodiode and displaying the output on a storage oscilloscope (Iwatsu, TS-8123) with a 50 Ω terminator, the oscilloscope was triggered externally with a Q-switched synchronous pulse from Nd:YAG laser. The storage scope is interfaced to a personal computer through a general-purpose interface bus (GPIB) and an interface card (National Instruments, USA) where the output signal is stored for further analysis. Secondly, by measuring energy directly on a calibrated laser power meter (Ophir, Model 30 A) by placing the meter in the path of the main laser beam. Laser energy was varied by changing the voltage on the laser oscillator and the amplifier. Burn patterns taken at different energies showed no significant variation in the mode pattern. The pulse duration was measured using a fast photo diode (Antel, Model AS-2, rise time < 35 ps). The output form the detector was displayed on an oscilloscope (Tektronics, 11302A). The output signal was digitized using digitizing camera (Tektronics, DCS 01) attached to the oscilloscope.

Digitized signals were fed to a personal computer for further data processing. A typical temporal profile of 8 ns pulse at 1.06 μm is shown in figure 3.1.

The interaction chamber and the experimental setup used for our study is shown in figure 3.2. The interaction chamber is made of mild steel with eight output ports. One of the output ports is used for laser entrance and one of the two perpendicular ports was used for recording the optical emission from the ablated plume and imaging the expanding laser-ablated plasma plume on an Intensified Charge Couple Device (ICCD). The chamber was evacuated to a pressure better than 10^{-4} Torr using a rotary/diffusion pump. The ambient gas was fed into the chamber from a gas cylinder through a needle valve connected to the interaction chamber. Experiments were carried out in presence of air, helium, argon, nitrogen and oxygen at various pressures ranging from 10^{-4} - 100 Torr. The chamber was purged several times before filling in the gas for experiment.

Laser ablation and formation of thin film on a substrate involves the formation of laser-induced plasma and propagation of ablated species to the substrate. The optimization of the plasma parameters during thin film growth may act as an in-situ diagnostic to obtain the films of desired properties. Hence in order to optimize the deposition parameters, it is essential to study the plasma plume on its course towards the substrate. Table 3.1 shows various diagnostic techniques used for studying plasma parameters such as vapor temperature, vapor pressure, vapor density, electron temperature, electron density, velocity of plasma/plasma species etc.. We have used plume imaging, optical emission spectroscopy, time of flight mass spectrometry and charge collector device to characterize the laser created plasma for our work.

FAST PHOTOGRAPHY

The laser beam was focussed on to an aluminum target in a vacuum chamber in ambient (Ar, He, air, O_2 and N_2) atmosphere at various pressures. Fast side on (two-dimensional) views of the expanding plume were made by recording the overall visible emission from the plume with a gated ICCD (Princeton Instrument, 576G/2). The detector consists of an intensifier, a Micro-Channel Plate (MCP) with spatial response in the region 200-800 nm and 384 x 576 CCD array. In order to have a better insight of the plume dynamics and film deposition processes the images were recorded at various time delays
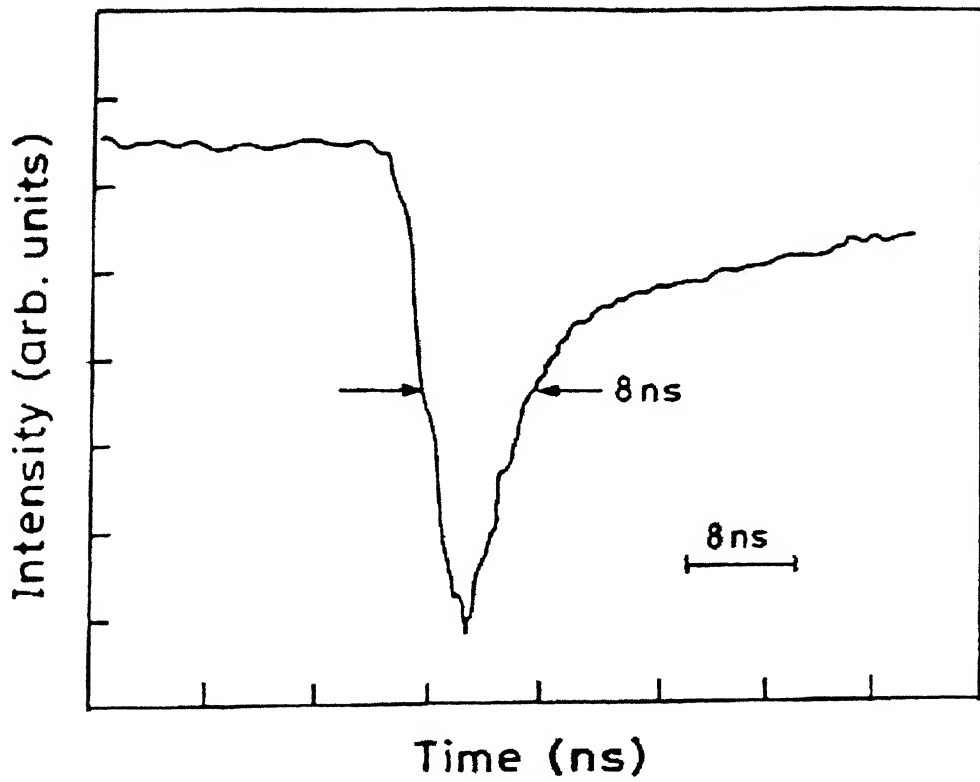
Fig. 3.1. Typical temporal profile of 8 ns (FWHM) pulse of Nd:YAG
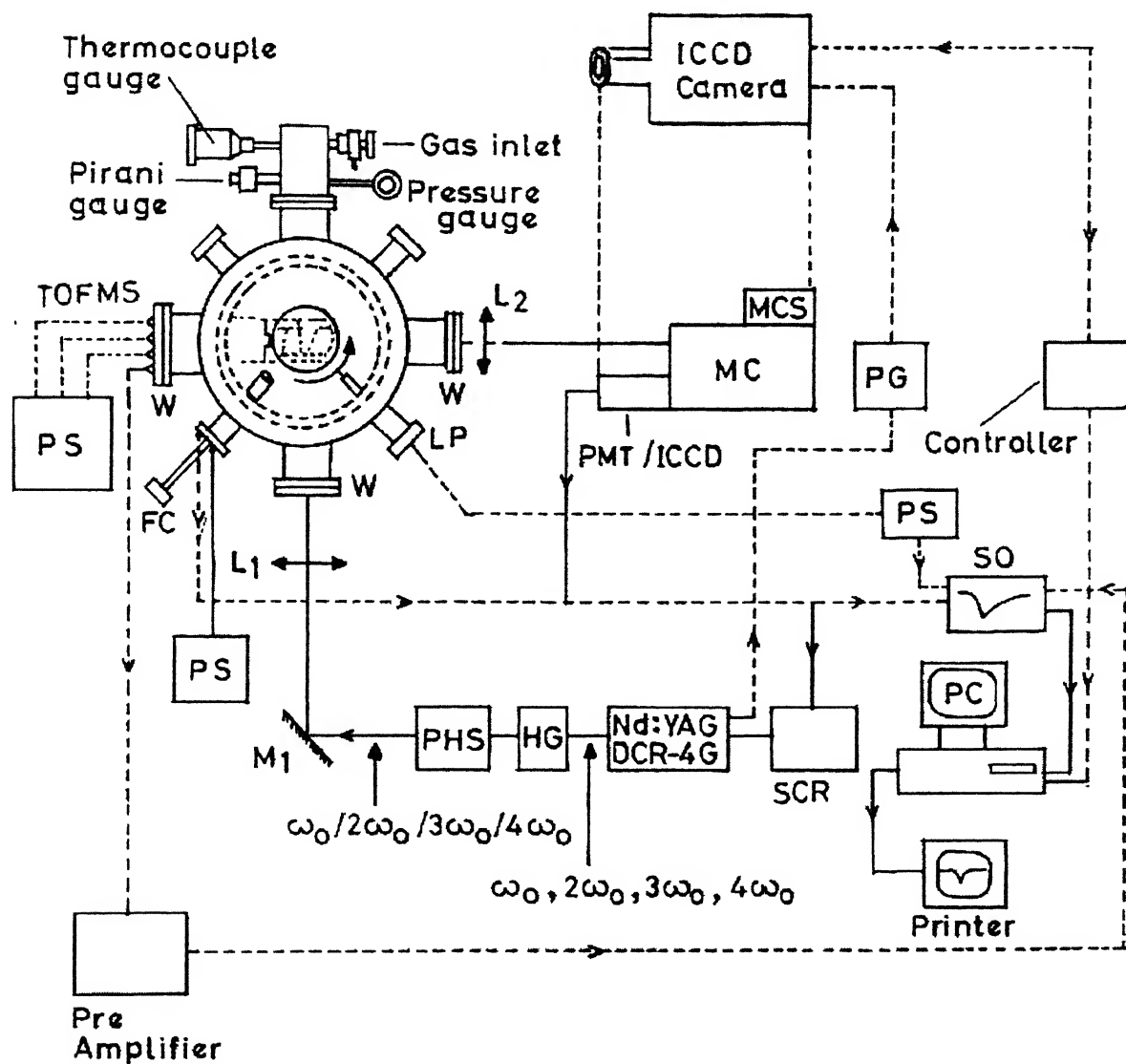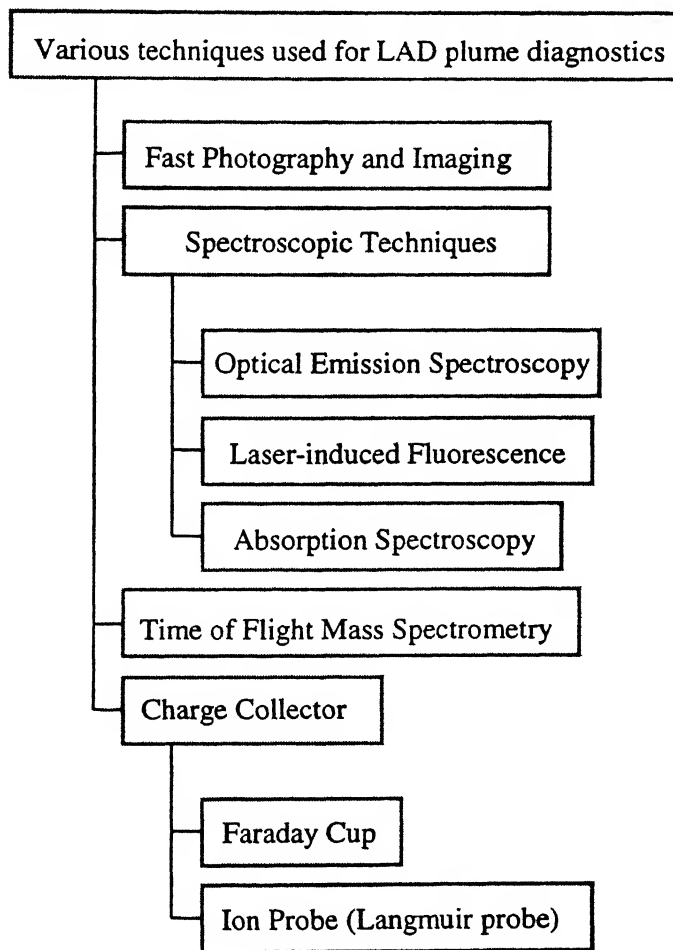
laser (λ = 1.06 μm)

Fig. 3.2. Experimental setup showing the interaction chamber and various diagnostics

Table 3.1.

Various diagnostic techniques used for studying plasma parameters

```
┌─────────────────────────────────────────────────┐
│ Various techniques used for LAD plume diagnostics │
└─────────────────────────────────────────────────┘
    │
    │   ┌──────────────────────────────────┐
    ├───│ Fast Photography and Imaging      │
    │   └──────────────────────────────────┘
    │   ┌──────────────────────────────────┐
    ├───│ Spectroscopic Techniques          │
    │   └──────────────────────────────────┘
    │       │   ┌──────────────────────────────────┐
    │       ├───│ Optical Emission Spectroscopy     │
    │       │   └──────────────────────────────────┘
    │       │   ┌──────────────────────────────────┐
    │       ├───│ Laser-induced Fluorescence        │
    │       │   └──────────────────────────────────┘
    │       │   ┌──────────────────────────────────┐
    │       └───│ Absorption Spectroscopy           │
    │           └──────────────────────────────────┘
    │   ┌──────────────────────────────────┐
    ├───│ Time of Flight Mass Spectrometry  │
    │   └──────────────────────────────────┘
    │   ┌──────────────────────────────────┐
    └───│ Charge Collector                  │
        └──────────────────────────────────┘
            │   ┌──────────────────────────────────┐
            ├───│ Faraday Cup                       │
            │   └──────────────────────────────────┘
            │   ┌──────────────────────────────────┐
            └───│ Ion Probe (Langmuir probe)        │
                └──────────────────────────────────┘
```

using a pulse generator (PG-200, Princeton Instrument, Inc.) and fixed gain of MCP. MCP has an adjustable gain from ~ 1-100 counts/photoelectron. The gain in the intensifier is set at 20 counts/photoelectron. The fast (5 ns or larger) gate pulses act as a shutter for the camera and hence the name fast photography. The read out time of the system is 50 kHz. These photographs are essentially photoelectric images of the plume. The results to follow are an average of five observations. The plume front is taken along the outermost axial position where the intensity falls to 25 % of the maximum intensity. These images are recorded on a personal computer which is interfaced to the controller. Figure 3.3 shows the typical experimental set up used for recording the plasma plumes.

ICCD Detector

Figure 3.4 gives a schematic sketch of the ICCD detector, showing various parts. The detector comprises of the following sections. The front enclosure contains the image intensifier and the CCD. The CCD is seated on a cold finger that in turn is seated on a thermoelectric cooler, driven by closed loop proportional control circuitry. The back enclosure contains the heat removal block where coolant is circulated. The electronics enclosure contains the preamplifier, the diode array driver, and the HV power supply. This keeps all signal, leads to the preamplifier as short as possible, and also provides complete RF shielding. Two swagelock connectors are used for circulating the coolant. Water is used as a coolant. ICCD are cooled by a Peltier effect thermoelectric cooler. A thermal sensing diode attached to the cooling block of the detector monitors its temperature. Heat generated at the exhaust plate of the cooler is conducted to the enclosure of the detector where it is carried away by water. ICCD is maintained at $\geq$ -35°C. The Detector is continuously flushed with dry nitrogen in order to avoid condensation. A pair of copper and brass fittings are connected to the two threaded coolant ports on the sides of the detector. Either of the ports can be used as the inlet for coolant.

ICCD detector uses an image intensifier both to gate light on and off (act as a shutter) and to increase the brightness of the image. The image intensifier detects and amplifies the light and CCD is used for readout. The coupling between the CCD and the intensifier is through fibre. A sensitive coupling arrangement combined with the high gain
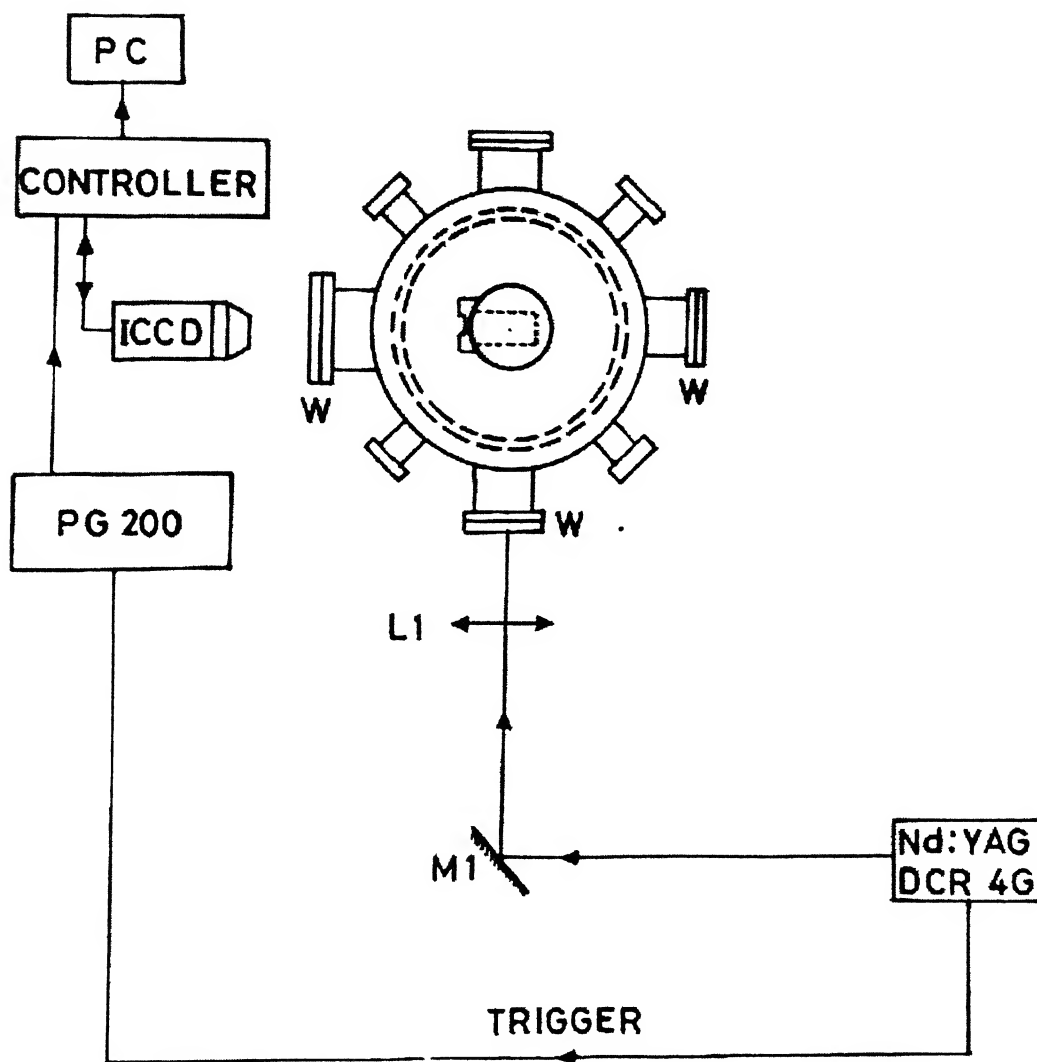
Fig. 3.3. Typical experimental set up used for recording laser-ablated plumes using ICCD
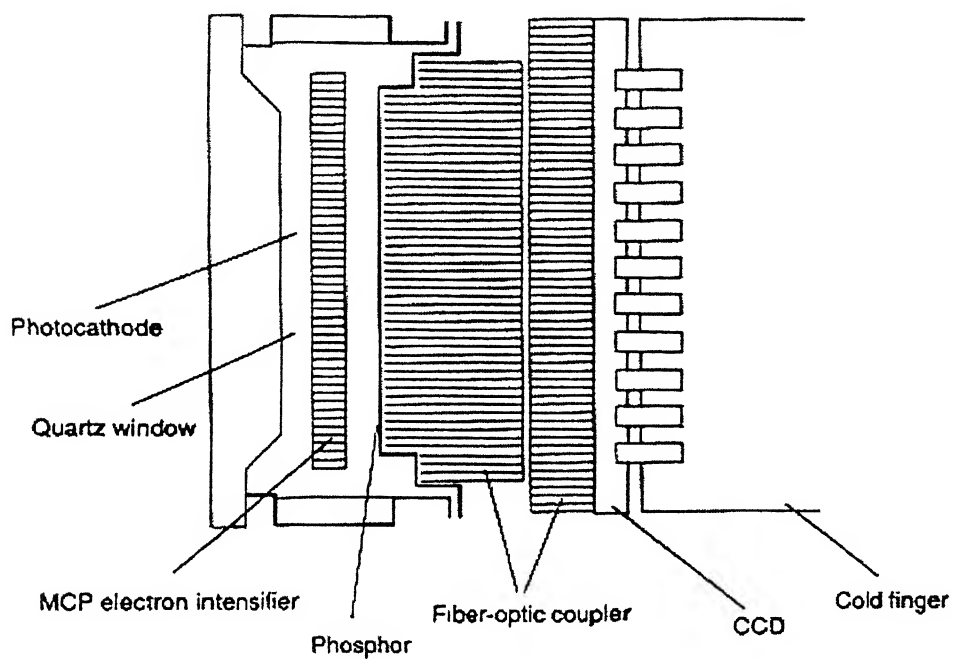
Fig. 3.4. Schematic sketch showing various parts of the ICCD detector

of the image intensifier and the low readout noise of the CCD array results in a detector capable of responding to a single photoelectron.

The MCP of the intensifier consists of more than 10^6 individual miniature electron multipliers with a precise input to output spatial geometric accuracy. Intensifier gain is varied by adjusting the voltage across the MCP i.e., the voltage across the MCP output and the phosphor. The second parameter is factory adjusted as it affects the gain and the resolution of the intensifier. The proximity-focussed MCP image intensifier is optically coupled to the diode array or CCD with an optical fibre coupled window. In CW mode of operation the photocathode potential is held approximately 200 volts negative than the potential of the MCP input. In the gated mode it is approximately 20-40 volts more positive and therefore the photoelectron image or spectrum cannot reach the MCP. At an exact predetermined time (from triggering onset), the pulse generator produces a negative pulse of approximately 200 volts amplitude. This pulse when applied to the photocathode renders it (for the duration of the pulse) more negative than the MCP and therefore the "photoelectron image or spectrum" is transmitted to the MCP and intensified. The MCP intensified "electron image or spectrum" is accelerated and focused (proximity focusing) onto the phosphor where it is converted to a "photon image or spectrum" with a further optical gain. This "photon image or spectrum" is transmitted to the individual pixels through the phosphor and the CCD optical fibre coupler. There it is detected, stored and then read out. CCD can be considered as a two-dimensional grid of individual photodiodes, called pixels each connected to its own charge storage 'well'. Each pixel senses the intensity of the light falling on its collection area and stores a proportional amount of charge in its associated 'well'. The imaging field of view of ICCD detector is shown in figure 3.5. A 50-mm Nikon telephoto lens attached at the detector front is used to image the plasma. Once enough charge accumulates the pixels are read out serially. CCD arrays perform three functions viz. transducing photons to electrons, integration and storage and finally read out. CCD's are very compact, rugged, and unintensified. They are easily cooled and can be precisely thermostated to within a few tens of millidegrees. The software allows to set the length of time the detector is allowed to integrate the incoming light, the exposure. During each scan the shutter or intensifier is enabled for the duration of the exposure period allowing the pixels to register light.
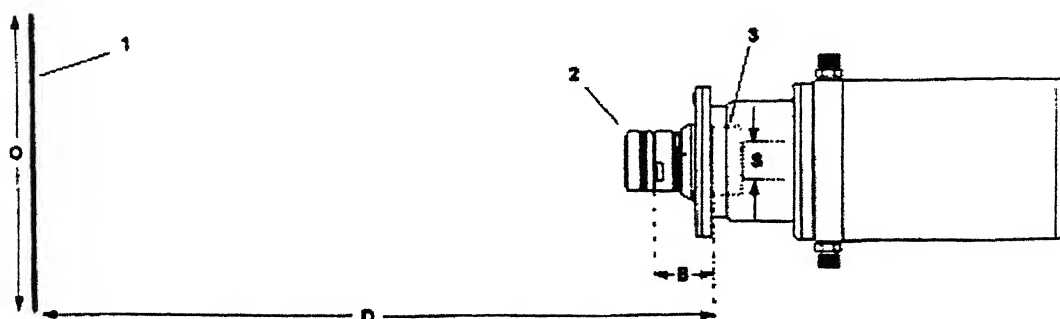
1. Object
2. Lens
3. Image intensifier

D = distance between the object and the image intensifier (the image intensifier is 46.5 mm behind the front edge of the lens adapter)

B = 46.5 mm

F = focal length of lens

S = horizontal or vertical dimension of CCD

O = horizontal or vertical field of view covered at a distance D

M = magnification

The field of view is:

$$O = S/M, \quad \text{where} \quad M = \frac{FD}{(D - B)^2}$$

Fig. 3.5. Schematic sketch showing the field of view of ICCD detector

Controller (ST-130)

As the name indicates, it controls the operations of the ICCD. The controller acts as an interface between the imaging and recording of the data. Firstly, the ICCD is to be guided to open the shutter and image the luminous object and secondly, before each image from the CCD detector appears on the computer screen, it is to be read, digitized and transferred to the computer. The algorithm of the process from imaging to recording is depicted in figure 3.6. The recorded images are then analyzed using software.

Pulse Generator (PG-200)

The PG-200 programmable gate pulse generator combines the function of a high voltage gate pulse generator and a sophisticated timing source/delay generator. It is primarily intended to provide high speed gating of proximity-focused MCP image intensifiers. The PG-200 extends pulse timings to the relatively long times, continuously variable pulse widths above 3 ns, simultaneous gating of two detectors, automatic sweeping of gate pulse delays and other automation and communication capabilities. It is interfaced to the ICCD series detector equipped with internal 1 MΩ terminator.

Plasma plume expansion was recorded using the overall visible emission from the plume with a gated, Intensified CCD camera system. The laser is the master, directly controlling the pulser which in turn controls the controller. The controller is operated in external synchronous mode and the pulser Trigger out is connected to the external synchronous input at the rear panel of the controller. As is already discussed the MCP prevents photoelectrons from the photo emissive detector surface from reaching CCD array until a gate voltage pulse is applied. Fast gate pulses (acting as shutter for the camera) were supplied at variable times w. r. t. the firing of the laser. Initial set up of gate width of 5 ns and a delay of 20 ns implies that the ICCD will open the shutter 20 ns after the laser pulse and will collect all the photons which will fall on the intensifier for 5 ns. Gradually gate width was increased with increasing delay times and the plume intensity was recorded at various times. The flow-chart and the timing mode for our experiment are shown in figure 3.7 (a) and (b) respectively. An important parameter for best image is the exposure or the gate width chosen for imaging i.e. this is the time for which the CCD is
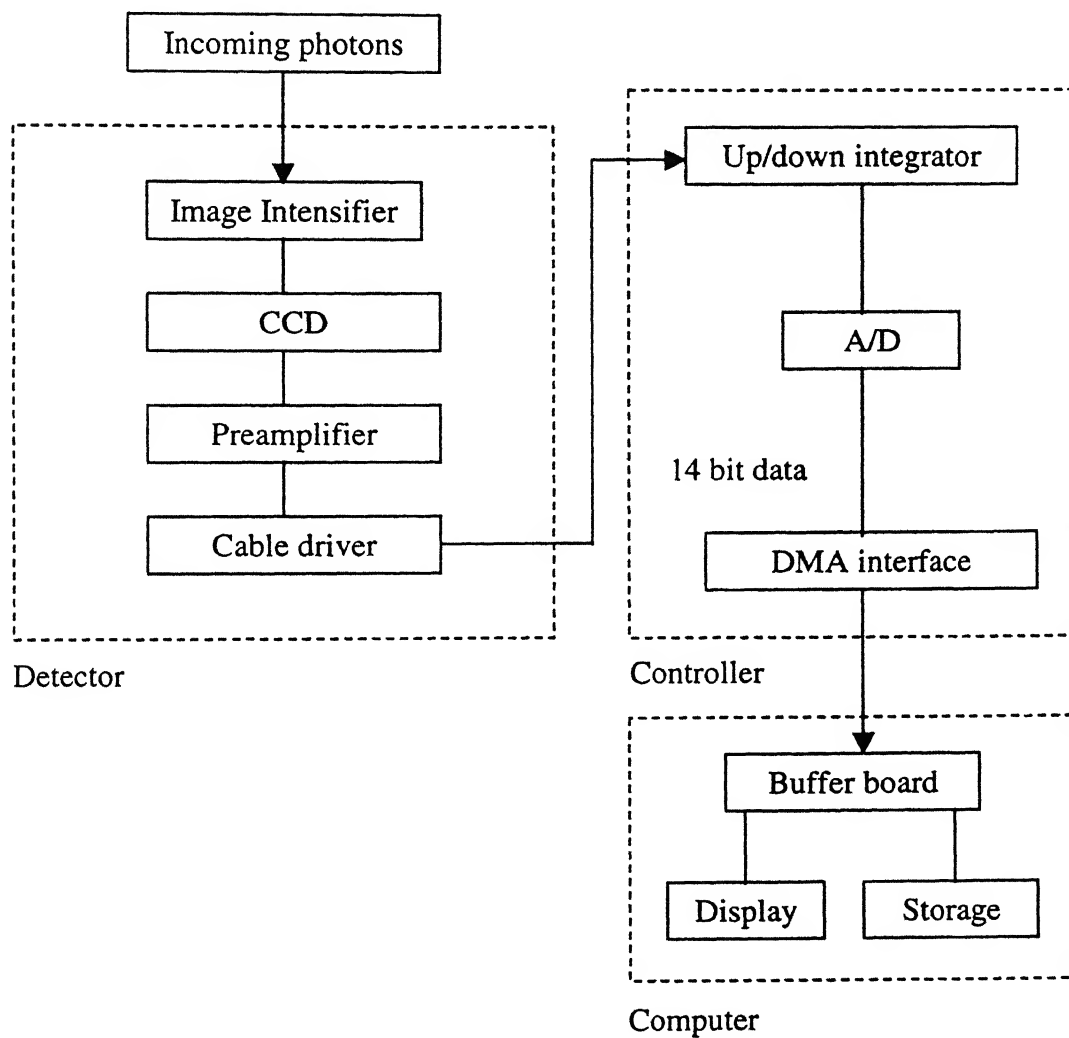
Fig 3.6. Flow chart of the process from imaging to recording by an ICCD

(a)

Laser (Nd:YAG, λ =1.06 μm)

Trigger in

Enable

HV Gate Pulser

Trigger out   Ext sync

Not scan

Controller

(b)

Laser trigger

HV gate pulse

Trigger out

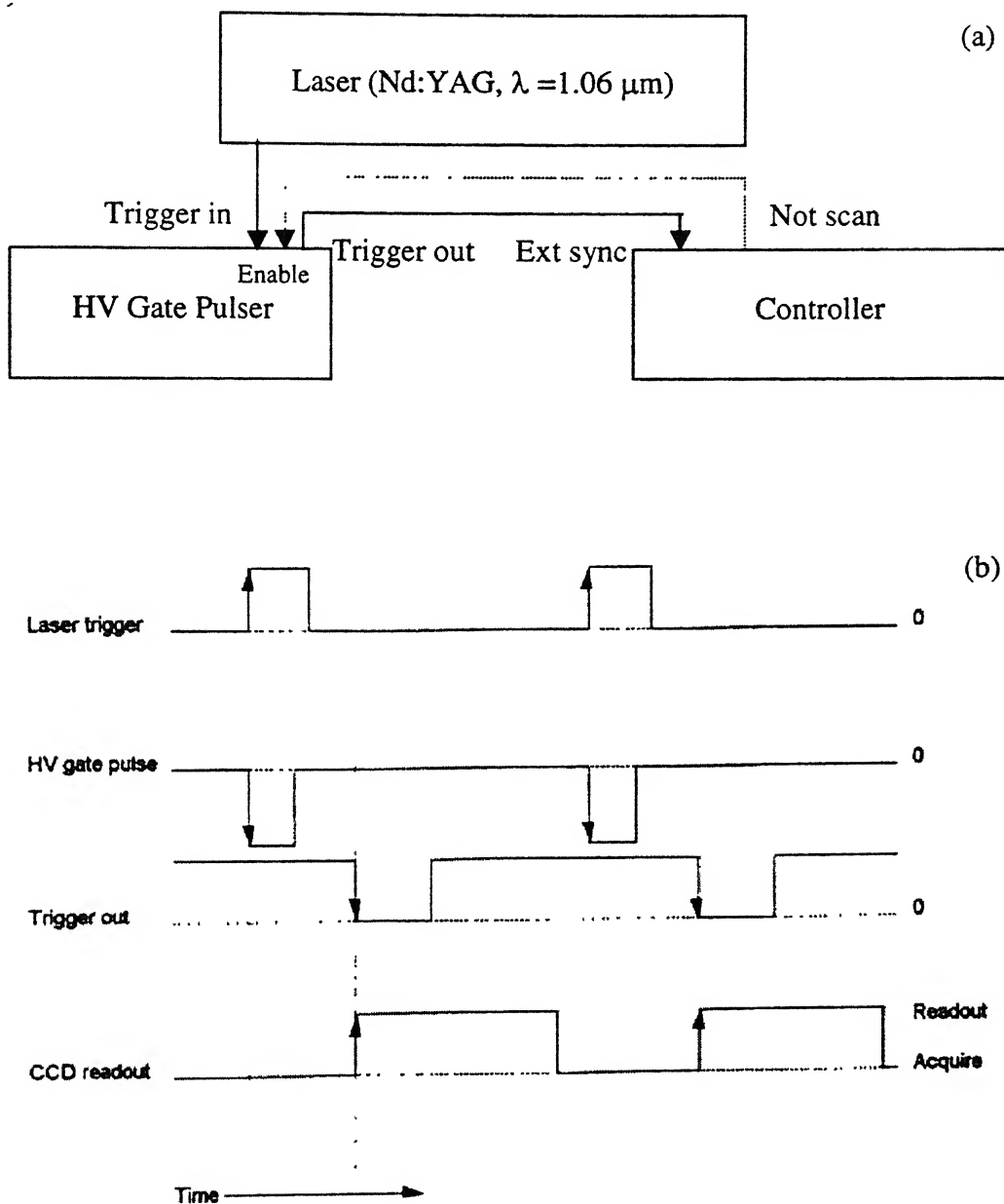CCD readout

Readout

Acquire

Time

Fig 3. 7 (a) Schematic layout of ICCD recording
(b) Timing modes of ICCD

exposed to the radiation. Over exposure results in loss of details in the bright regions of interest while under exposure misses the fainter regions.

Using the ICCD system, the front edge of the laser-ablated plume as a function of time was measured. The absolute velocities and hence the stopping distance of the plume is estimated [85,95,136]. The displacement of the front with time is used to compare theoretical results with the hydrodynamical model [136].

OPTICAL EMISSION SPECTROSCOPY

Diagnosing laser-ablated plasmas using emission spectroscopy is a well established technique [217] and has widely been used as a diagnostic tool during the deposition of thin films by laser ablation [218]. Investigation of the optical emission of the plasma plume gives information about the spatial and temporal evolution of the species of a LAP.

Laser beam from Nd:YAG laser was focused using a lens of focal length of 50 cm, onto a solid aluminum target in an ambient atmosphere or in vacuum and the plasma radiation emitted was imaged onto the entrance slit of the Monochromator (Jobin Yvon, HRS-2) with a lens of focal length 16 cm so as to have one to one correspondence with the plasma and its image onto the slit of the monochromator. The monochromator was continuously tuned using a microprocessor controlled scan system. The output from the monochromator was detected with a photo multiplier tube (Hamamatsu, IP28) and recorded on a strip chart recorder or displayed on the screen of the storage oscilloscope (Iwatsu, TS-8123) interfaced with PC. Figure 3.8 shows a typical Al spectrum in presence of oxygen at a pressure of 100 mTorr at a laser irradiance of 2.4×10^{10} W/cm^2 at 2 mm from target surface. The recorded optical emission is used to investigate the spatial evolution of the density and temperature of the laser-ablated aluminum plume.

Electron Temperature

Various methods of calculating electron temperature using spectroscopic observations are described in the literature [24,219,220]. We have used the relative intensities of the spectral lines from a given ionization state for estimating electron temperature. Assuming plasma in LTE, the electron temperature can be estimated using [216],
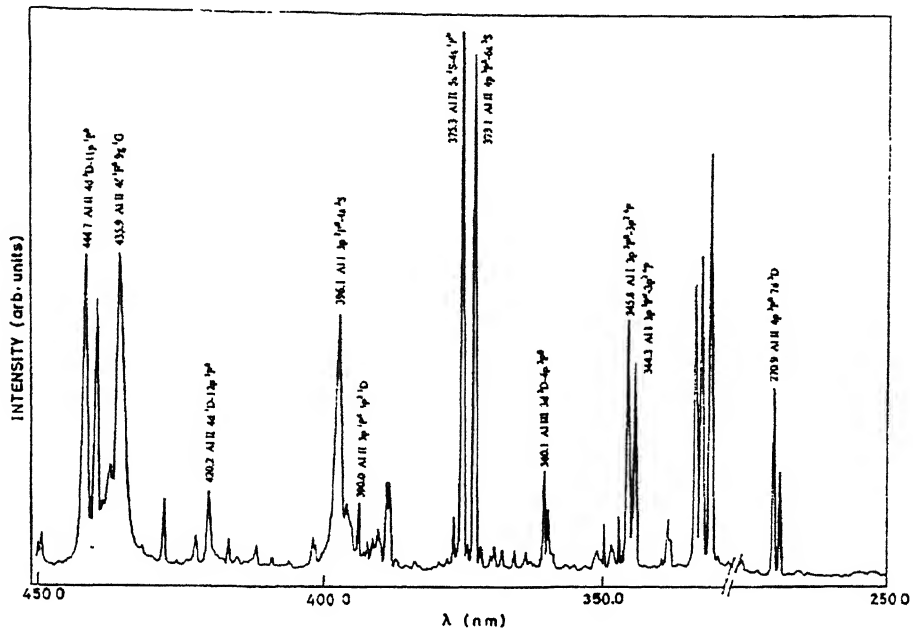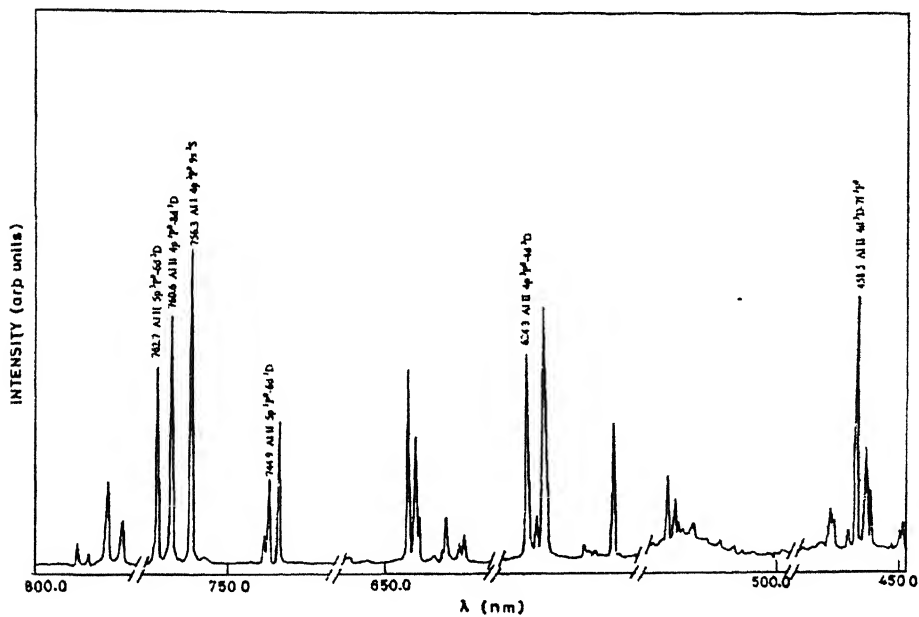
Fig. 3.8 Emission spectrum of the aluminum plasma in oxygen ambient at 100 mTorr at 2.4×10^{10} W/cm^2 of 1.06 μm laser radiation;

(a) 250 - 450 nm

(b) 450 - 800 nm

The prominent transitions are marked

$$k_B T_e = \left[\frac{E' - E''}{\ln\left(\frac{I_s'' \lambda'' g' A'}{I_s' \lambda' g'' A''}\right)}\right] \qquad (3.1)$$

where E'' and E' are the excitation energies of the lower and upper levels, respectively. I_s'' and I_s' are the intensities, g'' and g' are the statistical weights, A'' and A' are the transition probabilities and λ'' and λ' are the wavelengths of various transitions. k_B and T_e represent the Boltzmann constant and electron temperature, respectively. The slope of the curve (E' - E'') against [ln (I_s'' λ'' g' A' / I_s' λ' g'' A'')] gives electron temperature. The various parameters appearing in eqn. (3.1) are available in the literature [219,220]. The measured electron temperature of Al III species in our work lies between 1-2 eV in vacuum, and 5-13 eV in oxygen background at a pressure of 100 mTorr at same fluences. Figure 3.9 shows the variation of electron temperature with incident laser energy in oxygen ambient at a distance of 2 mm from the target surface.

Electron Density

The Stark broadened profile of a transition for which the Stark-broadening parameters are available in the literature, can provide electron density of the plasma [220,221]. Stark-broadening arises due to the coulomb interaction of the emitted species with both the electrons and ions expanding in the plume. Observed lines were fitted to Lorentzian profile with true half width given by,

$$\Delta\lambda_{true} = \Delta\lambda_{observed} - \Delta\lambda_{instrument} \qquad (3.2)$$

where $\Delta\lambda$ of a line (FWHM) is given by

$$\Delta\lambda = 2W\left(\frac{n_e}{10^{16}}\right) + 3.5A_1\left(\frac{n_e}{10^{16}}\right)^{1/4} x\left(1 - 1.2N_D^{-1/3}\right)W\left(\frac{n_e}{10^{16}}\right) \qquad (3.3)$$
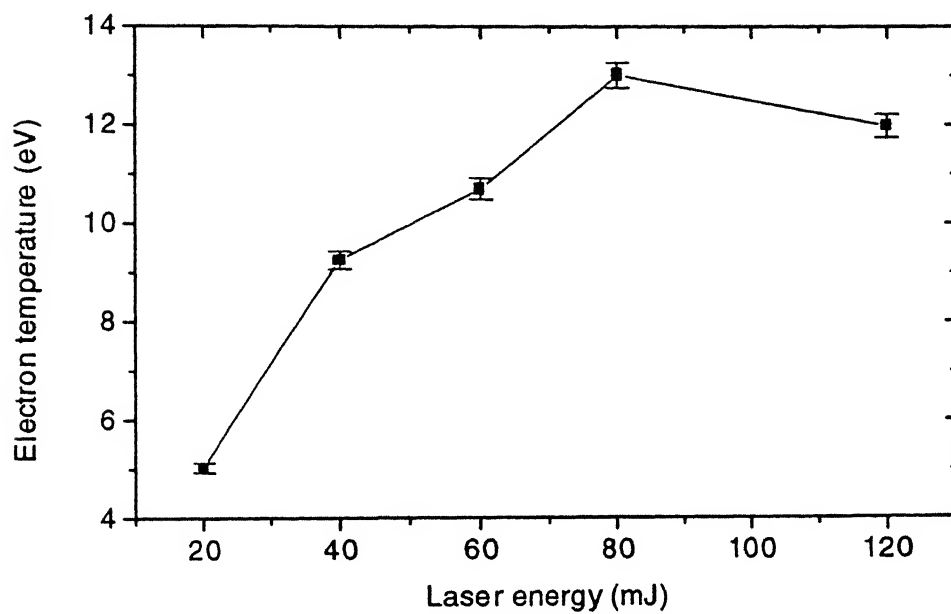
Fig. 3.9. Variation of electron temperature with incident laser energy in
oxygen atmosphere at 100 mTorr

First term in the eqn. (3.3) gives contribution from electron broadening and second term is the ion broadening correction; W is the electron impact parameter which can be interpolated at different temperatures and A_i is the ion broadening parameter. Both W and A_1 are weak functions of temperature, n_e is electron density and N_D is the number of particles in Debye sphere given by

$$N_D = 1.72 \times 10^9 \frac{[T_e(eV)]^{3/2}}{[n_e(cm^{-3})]^{1/2}} \qquad (cm^{-3}) \qquad (3.4)$$

Eqn. (3.4) is valid only if $N_D \geq 1$ and $0.05 < A_1 (n_e /10^{16})^{1/4} < 0.5$. Using our measured temperature of 6.0 eV (in oxygen ambient at a pressure of 100 mTorr and laser irradiance of 2.35×10^{10} W/cm^2) and density of 10^{16} /cm^3, we get the number of electrons in the Debye sphere equal to 80 and the parameter $A_1(n_e /10^{16})^{1/4}$ equals to 0.051. Accordingly the second term in eqn. (3.3) can be neglected. Considering only the electron impact broadening, eqn. (3.3) simplifies to

$$\Delta\lambda = 2 W \left(\frac{N_e}{10^{16}}\right) \qquad (A^0) \qquad (3.5)$$

Figure 3.10 shows a typical stark broadened profile of Al II (4p ^{1}P^o-4d ^{1}D) transition at 559.3 nm in vacuum. Figure 3.11 shows the variation of electron density with distance in oxygen ambient. It is observed that for both the vacuum and oxygen ambient, electron density increases with the increase in fluence and saturates at higher irradiances. The increase in electron density is due to coupling of larger energy to the target and the plasma resulting in the larger vaporization at the target and ionization in the plasma, respectively. The electron density decreases with increase in distance from the target. In our experiment n_e lies between $10^{15} - 10^{16}$ cm^{-3}.

Local Thermal Equilibrium

In Local Thermodynamic Equilibrium (LTE), it is assumed that collisional events, in particular the events involving electrons, determine the behavior of the system. These
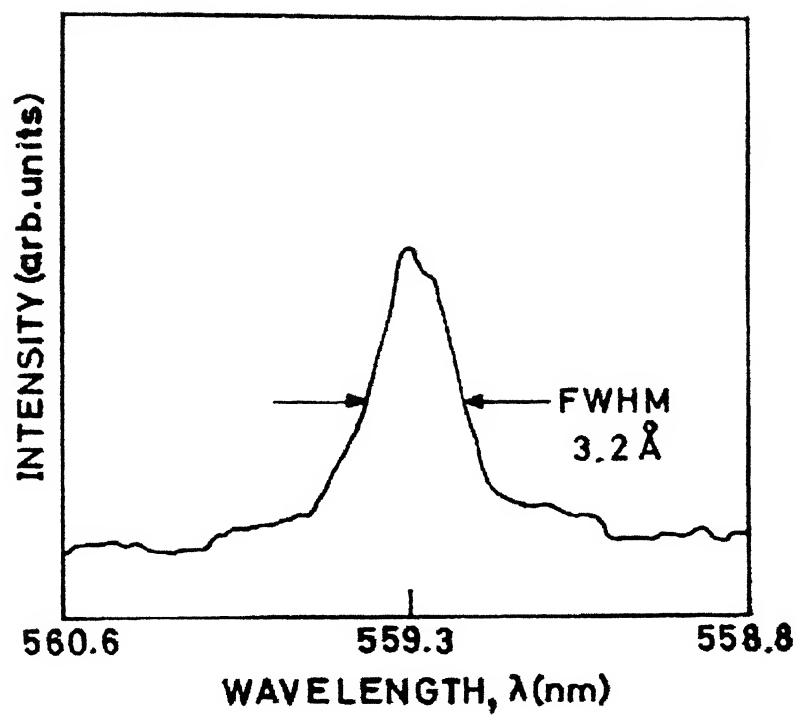
Fig. 3.10. Typical stark broadened profile of Al II (4p $^1P^o$ -4d ^1D)
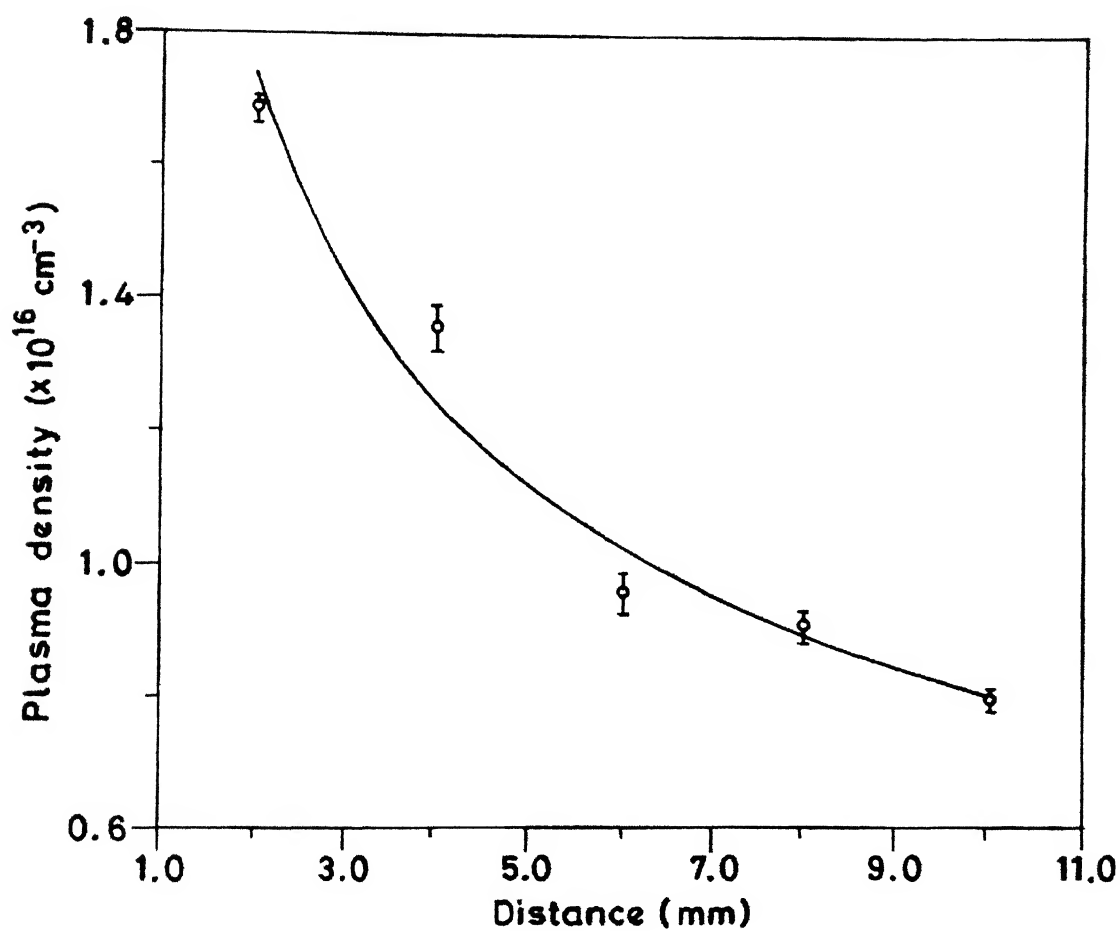
transition at 559.3 nm in vacuum

Fig. 3.11. Variation of electron density with distance in oxygen atmosphere at 100 mTorr and laser irradiance of 2.4×10^{10} W/cm^2

collisions are assumed to be governed by the same laws which hold in thermodynamic equilibrium. A necessary (but not sufficient) criterion for LTE to hold is [222]

$$n_e \geq 1.4 \times 10^{14} T_e^{1/2} (\Delta E_{mn})^3 \qquad (cm^{-3})$$

where T_e is the plasma temperature in eV, ΔE_{mn} is the energy difference between upper and lower energy levels (in eV). For a transition at 559.3 nm, ΔE_{mn}=2.21 eV, the lowest limit of n_e is 1.98 x 10^{15} /cm^3. Our calculated values of n_e ($\sim 10^{16}$ cm^{-3}) are greater by an order of magnitude thus implying that LTE approximation for this analysis is valid. The nature and characteristics of the laser-ablated plasma strongly depends on the laser irradiance. It is observed that the value of plasma parameters usually saturates at higher irradiance, this can be attributed to absorption or reflection of laser photons by the dense plasma itself [28]. The reflection of the incident beam depends on the plasma frequency ν_p, which should be lower than laser frequency. For our case with Nd:YAG laser (λ = 1.06 μm), the laser frequency corresponds to ν_l = 2.828 x 10^{14} Hz The plasma frequency is given as ω_p = 8.9 x $10^3 \, n_e^{1/2}$ Hz, where n_e is the electron density. In our experiment we determined the density of plasma species by measuring the Stark broadened profile [85] of Al II (4p ^{1}P^o-4d ^{1}D) transition at 559.3 nm. to be $\sim 10^{16}$ cm^{-1}. Thus, the plasma frequency ω_p works out to be 2.82 x 10^{12} Hz, which is smaller than the laser frequency. This implies that the energy losses from the plasma due to the interaction of the laser beam with plasma is insignificant.

TIME OF FLIGHT MASS SPECTROMETER (TOFMS)

A time of flight mass spectrometer is a device in which ions of differing masses are given the same energy and are allowed to traverse a field free space. Because of their differing velocities, the lightest ions arrive first at the end of the drift space where a collector is put. The amplified current signal from the collector is displayed on an oscilloscope. In our experiment, ions are produced by bombarding the aluminum target with a pulsed laser beam. The ions are accelerated by means of electrostatic fields and are injected into the field free drift region. They are detected by the detector, a channel electron multiplier (CEM). The output signal amplified by a preamplifier is fed to the storage oscilloscope which is interfaced with a personal computer for further analysis. The velocity of each ion in the field free path is proportional to the square root of their mass to charge

ratio. Thus at the end of the flight tube the ions are separated into bunches corresponding to the mass to charge ratio. An ion detector at the end of the drift tube receives ions with different masses at different times. The record of the detector signal as a function of time is deconvoluted to obtain the mass distribution of ions. The advantages of TOFMS over mass spectrometers are:

1. The large speed at which the complete spectrum can be displayed.
2. Entire mass spectrum can be recorded for each laser pulse.
3. The accuracy depends on electronic circuits rather than on extremely accurate mechanical alignment.
4. It has unlimited mass range, defined by the resolution of the instrument.

The only disadvantage of this device is its limited resolution.

A schematic of a linear time of flight mass spectrometer designed for our work is shown in figure 3.12. The design based on our requirements was optimised using a computer program. The fields in the extractor and accelerator regions were modeled with an optics program called Simion (The Idaho National Engineering Laboratory). The results for the optimum conditions are shown in figure 3.13. The TOFMS consists of stainless steel flight tube E_3, 20 cm long and 2.5 cm in diameter. The source region, 2 cm wide, consists of pusher electrode E_1 and puller electrode E_2 well separated with teflon insulators. The detector (CEM, Dr. Sjuts Optotechnik, Germany) is mounted at the end of the flight tube. The whole TOF assembly is mounted on four 3 mm diameter stainless steel rods which can be extended for extending the length of the flight tube. The pusher electrode E_1 is internally grounded and for optimum operating conditions voltage E_4 is applied on the cone of CEM with tail grounded through a load resistor.

TOFMS is attached to the interaction chamber on a port perpendicular to the laser beam entrance port, figure 3.2. The output is amplified and is stored on to a personal computer. A Typical TOF signal is shown in figure 3.14. The experiment was carried out at a pressure better than 10^{-5} Torr. In order to calculate the emission threshold of the target, the laser energy on an Al target was varied in steps of 1 mJ and the output signal was recorded on to the personal computer. It was observed that the first ionic signal appeared at a value of 5.89×10^9 W/cm^2, this value of laser irradiance is termed as threshold for aluminum. The value matches well with that available in the literature [223].
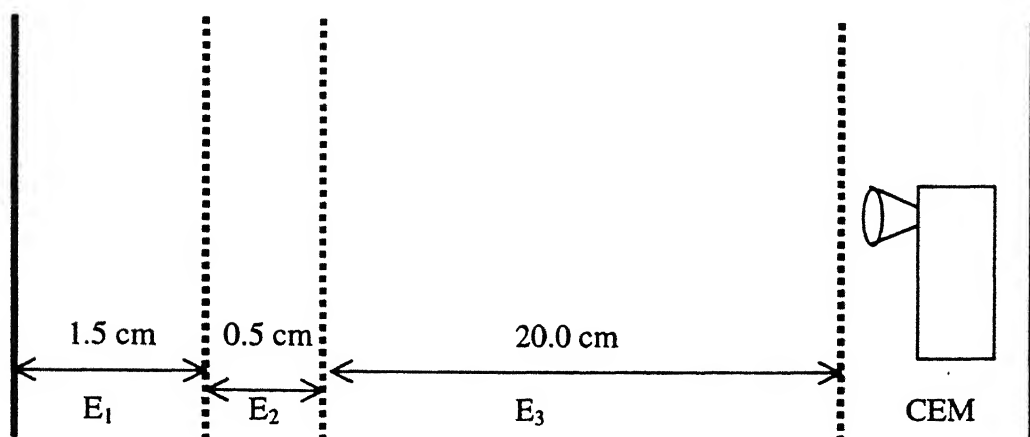
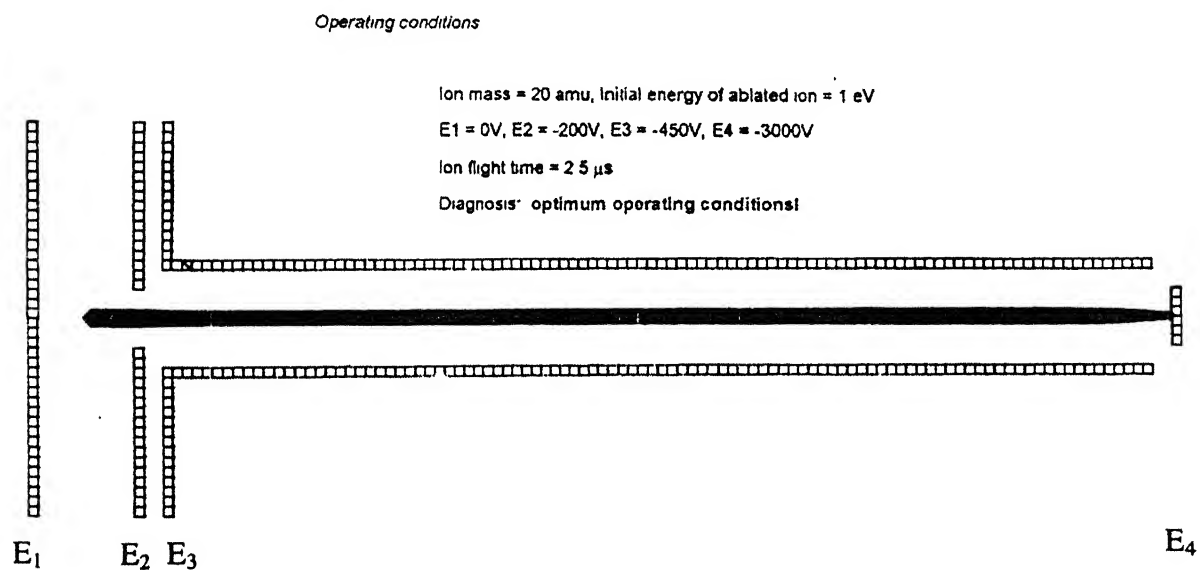Fig. 3.12. Schematic design of a linear TOFMS designed for our experiment

Operating conditions

Ion mass = 20 amu, Initial energy of ablated ion = 1 eV

E1 = 0V, E2 = -200V, E3 = -450V, E4 = -3000V

Ion flight time = 2 5 µs

Diagnosis optimum operating conditions!

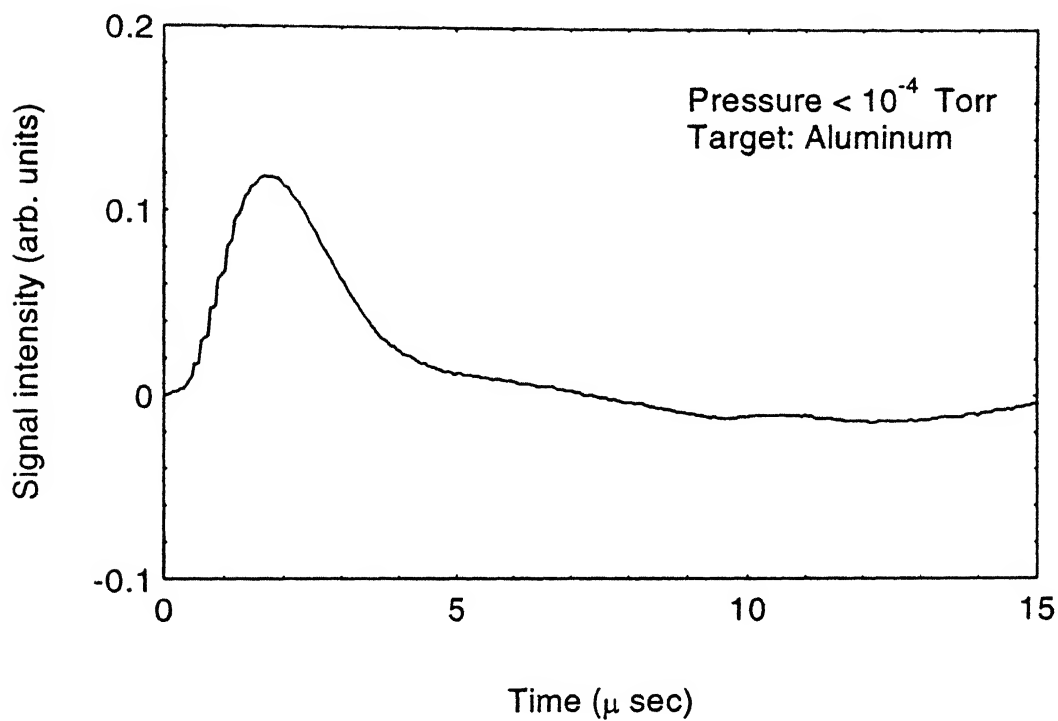Fig. 3.13. Optimum parameters for operation of TOFMS

Fig. 3.14. Typical time of flight signal as recorded using TOFMS

FARADAY CUP

In order to diagnose the laser-ablated plasmas for the behavior of electrons and ions within the plasma a charge collector was designed [224]. A simple approach would be to insert some kind of a probe that directly senses the particle flux. Langmuir probe [120,225] was the first of its kind used to investigate plasma. But the problem with this type of probe is that one could not obtain the information about the ion distribution function when it is repelling ions and vice versa. A practical solution to this problem is the use of "gridded energy analyzer", in which a system of grids at different potentials is used. This gridded analyzer is called "Faraday cup". The behavior of ions and electrons can be studied by biasing the grid accurately. The location of a Faraday cup used in our experiment is shown in figure 3.2. We have used Faraday cup in time of flight (TOF) mode for our work.

The three designs of Faraday cup, which evolved as a need for enhancing accuracy are shown in figure 3.15. All employ a biased grid for charge separation. The Type I Faraday cup utilizes a single grid in front of a flat plate collector. The grid voltage was referenced to the vacuum chamber ground and the collector potential allowed to float. This has two disadvantages; firstly, there is no reference plane for grid, hence the necessary charge separation could not be attained. Secondly, there is no provision for suppressing secondary electron emission. In order to overcome these problems, Type II was developed. In this design we have two grids and a flat plate collector. The function of the second grid is to provide a reference plane for the rejection of ions or electrons. In a two-grid system, the charge-separating region is screened from the collecting electrode so that any spurious current carried by the unwanted charges do not obscure the desired signal. The Type II Faraday cup has advantage over Type I, but it still had no means to suppress secondary emission. Hence Type III was designed with a honeycomb collector.

A honey comb collector Faraday cup is shown in fig. 3.15 (type III). A flat copper plate in type II is modified by drilling closely spaced 5 mm diameter holes with depth 15 mm resulting in depth to diameter ratio of about 3.33. Each small hole resembles a "deep cup". A large number of secondaries generated within the holes are recaptured. This drilled copper plate is inserted inside a hollow nylon cylinder. The plate can be moved to and fro inside the cylinder, if necessary, with the help of slot provided on the back of the plate. Then follows the two-grid arrangement as shown, the first grid is grounded along with the
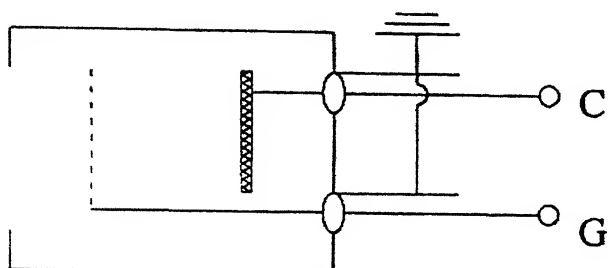
Type I
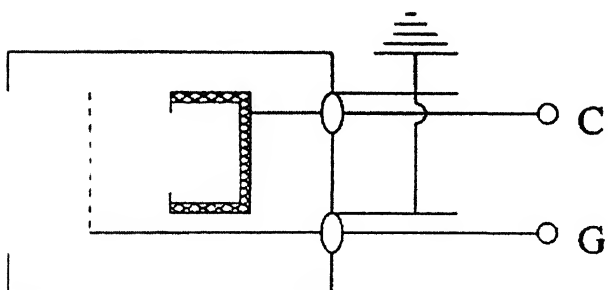
Type II
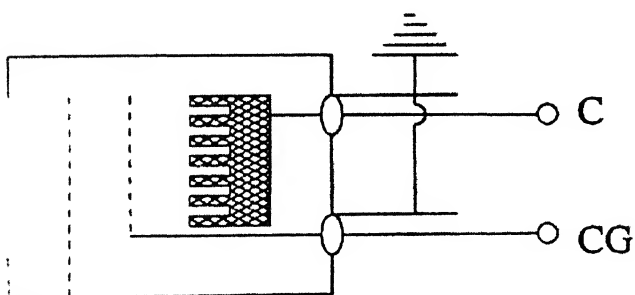
C = Collector

G = Grid

RG = reference grid

CG = Control grid

RG

Fig. 3.15. Schematic sketch of different designs of Faraday cup

apparatus and the second is given a floating voltage. In order to measure the electron current, a positive voltage is applied to the middle grid and vice versa for ions. The distance between the grids is maintained by nylon spacers. A provision is made in the nylon cylinder for feeding a copper wire which can be soldered on to the middle grid so that voltage can be applied to it. The distance between the front end of the honeycomb collector and the middle grid can be varied between 2.5 mm to 10 mm. Another copper wire is soldered on to the back of the honeycomb plate so that the current signal from the cup can be measured. The whole assembly is fitted in a hollow brass cylinder with nylon lining, which acts as an insulator. The brass cylinder is of length 60 mm and of diameter 30 mm and wall thickness of 2 mm. In front of the Faraday cup, a brass cap is attached for protection. A 1 mm diameter hole drilled on the front end of this push cap acts as an entrance for charges to Faraday cup. In order to spatially move the charge collector, a hollow brass rod is brazed on the rear end of the charge collector (CC). The inner and outer diameters of the brass rod are 10 mm and 13 mm respectively. Wiring is done in such a manner that the wires coming from inside of the CC pass through the length of the rod and are soldered on to BNC's at the end. The CC was mounted on a Wilson seal to one of the ports of the interaction chamber.

The Faraday cup was used in time of flight mode to measure the time of flight spectra of ions and electrons. A cylindrical aluminum rod is used as a target. The assembly was mounted on a port at an angle of 45° with respect to the laser beam. The interaction chamber was evacuated to a pressure better than 10^{-3} Torr using a rotatory pump. As the laser is focussed on to the target in a single shot operation, laser-ablated plasma evolves and enters into the charge collector. The polarity and the potential on the grid decides the type of charge (electron or ion) it would allow to reach the honey comb collector. The signal is fed to a storage oscilloscope which is interfaced with a personal computer. The time of flight data was used to estimate the average velocity and hence the kinetic energy of ions and electrons. The area under the signal curve gives the yield. Experiment was carried out at various distances between the collector and the target. The potential at the middle grid, collector were varied at various distances and the laser energy. The voltage at grid and the collector was varied in order to optimize the Faraday cup for detecting the ions. The collector bias voltage was optimized so that only ion signal was seen even at zero grid bias. The optimum collector bias voltage was - 40 V. A typical V_g-I_s (grid voltage-collector

current) characteristic curve is shown in figure 3.16. Once the potential at the charge collector was optimized, the middle grid was given a negative potential which was varied from 0 to -140 V in steps of 20 V, to record the effect of grid potential on ions.

It is observed that the intensity of ion increases with increase in collector bias voltage. The enhancement in intensity is because of suppression of electrons due to high potential barrier at the collector. The collector signal increases with the negative grid bias as shown in figure 3.17. With the increase in negative grid bias a large fraction of negative ions is blocked by grid and hence there is an increase in total number of positive ions reaching the collector resulting in increase of total ionic yield. The observed increase in intensity of the signal with the incident laser intensity is attributed to increase in ionization in the plume due to absorption of the laser photons. The yield decreases with the increase in distance of collector from the plasma.

In order to study the behavior of fast moving electrons, the Faraday cup was used with collector at ground potential and the ion electron separation was done only by the grid bias. Figure 3.18, shows a temporal profile of the plasma. It essentially gives the velocity distribution of the ions and electrons in the plume. The initial dip in the figure corresponds to fast electrons emitted from the plasma. The positive peak in the figure corresponds to the ion current. This peak is observed to increase with increase in energy (as more and more of plasma is ionized), while it decreases with the increase in distance (less electrons reach the detector) from the target. The second dip occurring at around 3 μs may be due to the slow electrons reaching at the collector. This peak correspond to electrons from double vaporization of the target. To understand this peculiar phenomenon we consider the basic process of plasma formation by laser ablation. For a long pulse (nsec) irradiation of a solid target, a part of the laser pulse removes a small amount of material from the surface which is further heated by absorption of the incoming laser radiation. The absorbing plasma prevents the light from reaching the target surface. The surface is effectively cut off from the incoming radiation for a large fraction of the laser pulse. Near the end of the laser pulse the blowoff material becomes so hot that it begins to reradiate. In addition, there may be ablation caused by the direct collisional interaction between the highly energetic plasma constituents and the material of the solid target. Some of this radiation may reach the target surface causing further vaporization and hence electrons. Thus there is a double emission of
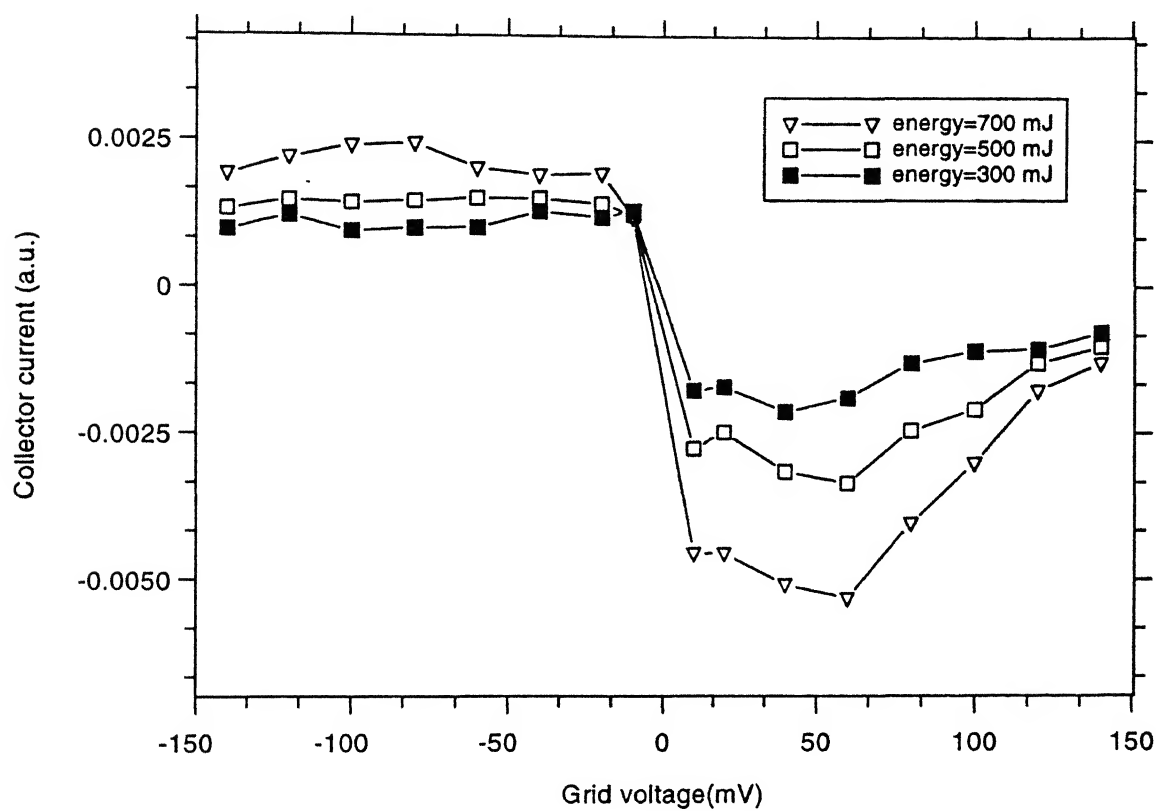
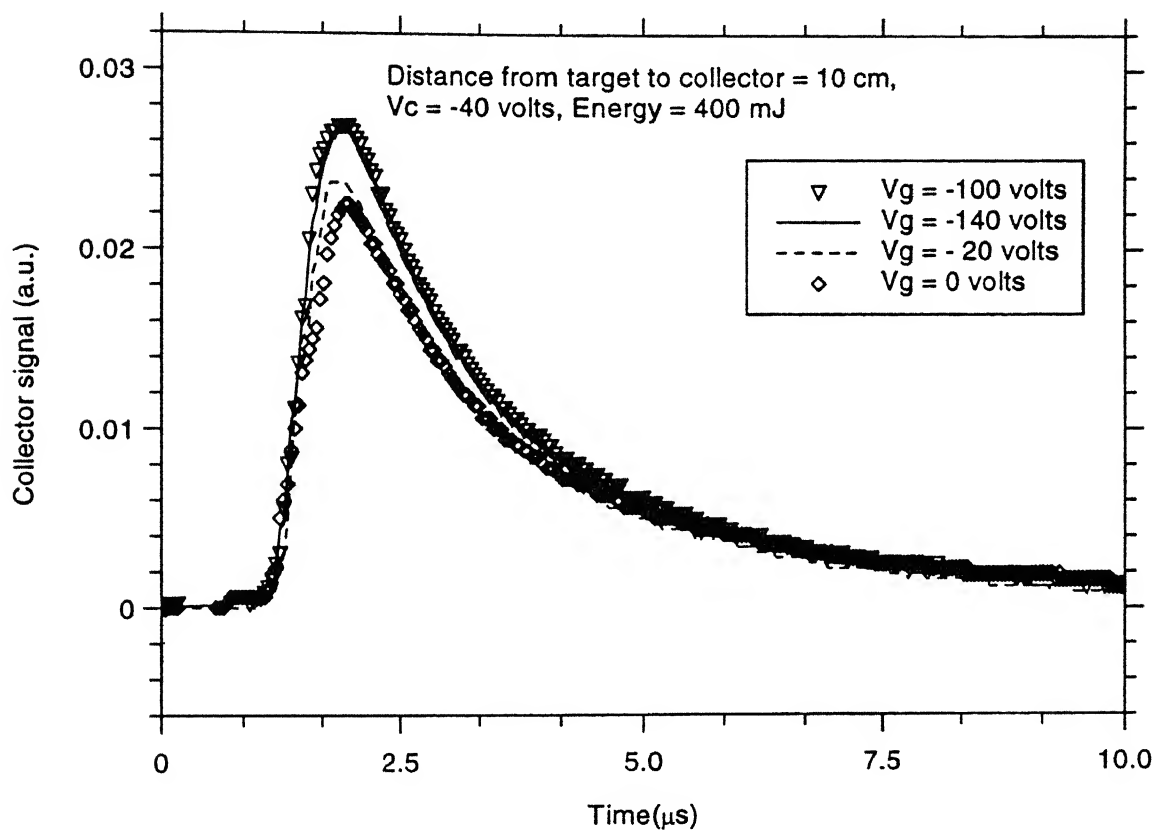Fig. 3.16 The collector current as a function of control grid potential

Fig. 3.17 Temporal variation of collector signal for various grid potentials

Vc = 0 volts, Vg = 0 volts, Distance from target to collector = 4cm

Energy = 100 mJ/pulse
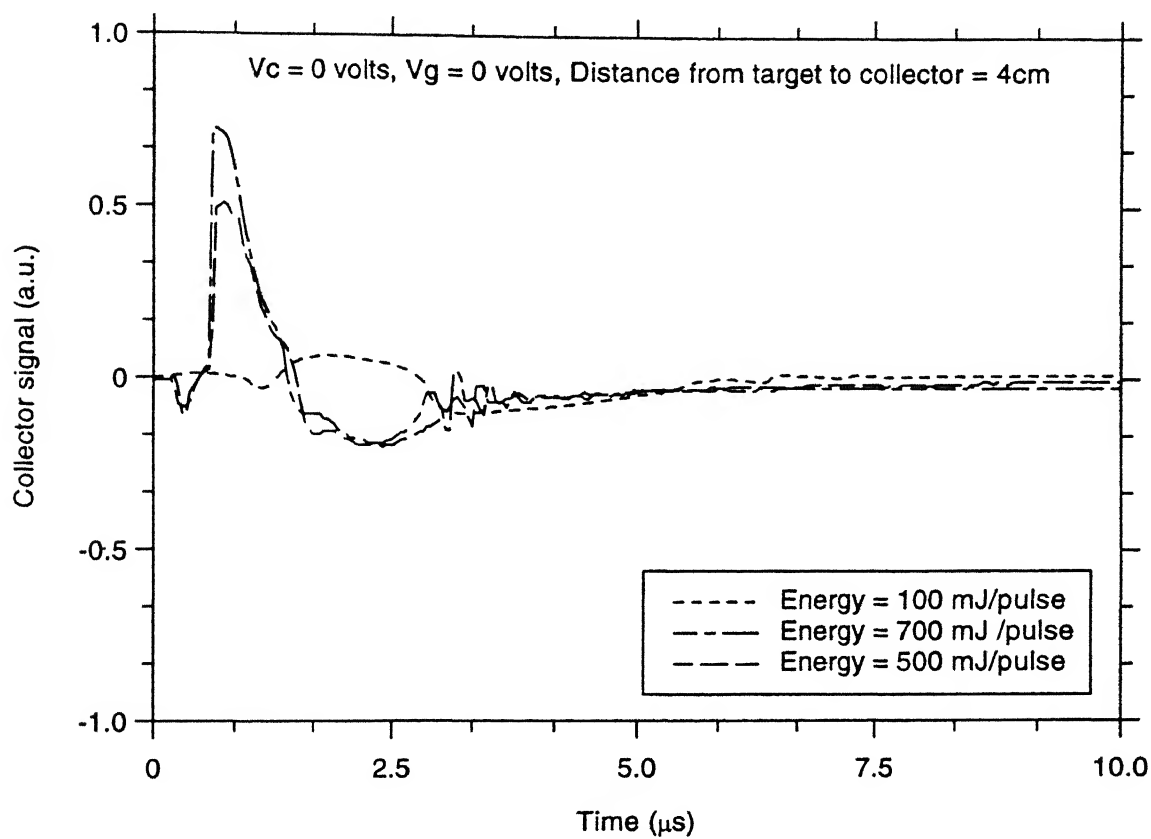Energy = 700 mJ /pulse
Energy = 500 mJ/pulse

Fig. 3.18. Temporal profile of a laser produced Al plasma

electrons during a single laser pulse. The double vaporization of the material from the target surface results in the stratification of the plasma and has been confirmed by Thareja et al [95] using Integrated Charge Couple Device (ICCD) camera system. Keeping the collector at 5 cm with a fixed grid bias the electron and ion currents were recorded by varying the laser energy on the target. Increasing laser energy enhanced the process of ionization in the plume and hence the intensity of both electrons and ions is seen to increase and their peak arrival time decrease. The increase of negative grid bias resulted in increase of the ion peak, however, it reduced the intensity and the arrival time of electron peak. The increase in the negative bias essentially implies repelling of slower electrons, the higher velocity electrons may still manage to cross the potential barrier of grid and reach at the collector surface. The retrenchment of the slow velocity electrons results in the distribution peak to shift towards lower time scale and decrease in intensity.

Most Probable Velocity and Kinetic Energy

Time of flight (TOF) measurement provides an excellent technique to determine the velocity distribution of the species in a plasma. We have used both TOFMS and Faraday cup to measure the velocity and hence kinetic energy of ions. Figure 3.19, shows a typical time of flight data obtained from a Faraday cup collector at 10 cm from the target at a laser energy of 200 mJ/pulse. The intensity on the TOF trace corresponds to the number of particles arriving at a particular time. The peak of the TOF curve corresponds to the most probable time. Knowing the distance between the target and collector (d) and the most probable time (t_p), one can calculate the most probable velocity and kinetic energy,

$$\text{most probable velocity,} \quad v_P = \left(\frac{d}{t_P}\right)$$

$$\text{and therefore, most probavle kinetic energy} \quad K.E_P = \frac{1}{2} m \left(\frac{d}{t_P}\right)^2$$

where m is mass of aluminum atom. Laser ablation from a solid surface produces a strong forward peaked distribution along the normal to the target surface [226]. Due to the collisions among the ablated species in the first stage of evaporation, the ablation process behaves like a nozzle source, relative to the plume expansion in vacuum, imparting a large
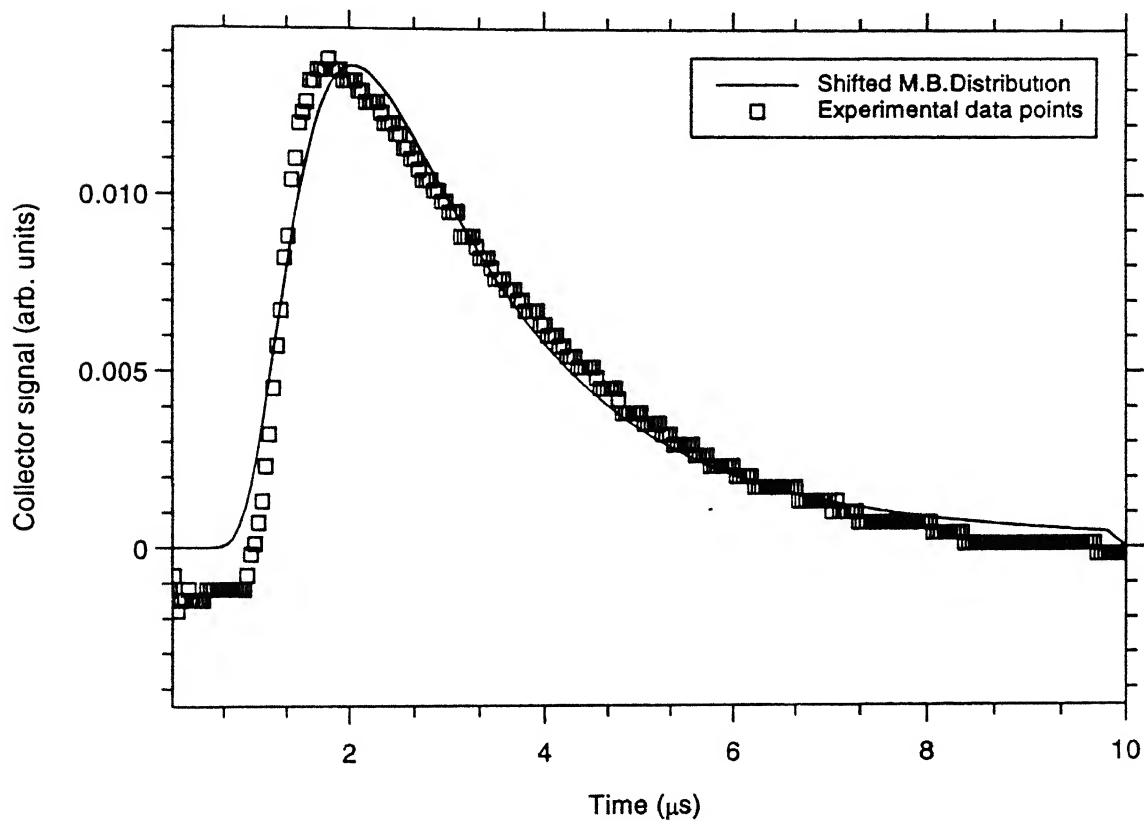
Fig. 3.19 Typical time of flight curve obtained from a Faraday cup at 10 cm from the target at laser irradiation of 4.8 x 10^{10} W/cm^2

center of mass motion to the generated ions. The equation of their motion can be obtained by modifying the classical Maxwell-Boltzmann distribution given by

$$S(t)dtd\Omega = Ct^{-4} \exp\left[-\frac{m\left\{\dfrac{d}{t}\right\}^2}{2k_BT}\right]dtd\Omega \tag{3.6}$$

where $S(t)$ is signal intensity at a distance d from the target and at a time t after the laser pulse hits the target. C is a dimensional normalization factor, T the temperature at equilibrium.

The experimental data from Faraday cup were fitted using a least square fitting on to a shifted Maxwell-Boltzmann distribution given by

$$S(t) = Ct^{-4} \exp\left[\frac{-m\left\{\dfrac{d}{t} - v_{com}\right\}^2}{2k_BT_{sl}}\right] \tag{3.7}$$

and is shown in figure 3.19. The variation of most probable kinetic energy with fluence is shown in figure 3.20. The typical velocity of ions is observed to be 10^6 cm/sec.

Ionic Yield

As mentioned earlier, TOF gives the number of particles reaching the detector at a particular time. The total number of ions reaching at the collector surface for the laser pulse period is obtained by integrating TOF spectra with respect to time,

$$\int S(t)dt = \int Ct^{-4} \exp\left[\frac{-m\left\{\dfrac{d}{t} - v_{com}\right\}^2}{2k_BT_{sl}}\right]dt \tag{3.8}$$

where the symbols have the same meaning as before. The dependence of ionic yield on laser fluence and distance from the target is shown in figure 3.21.
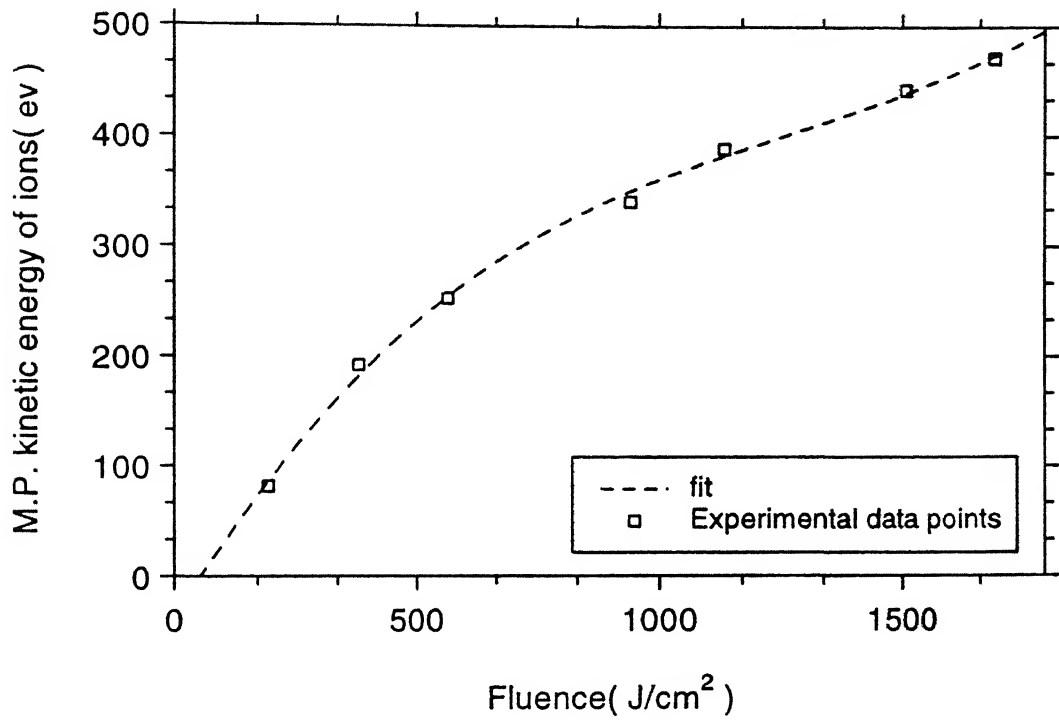
Fig. 3.20 Variation of most probable kinetic energy with fluence
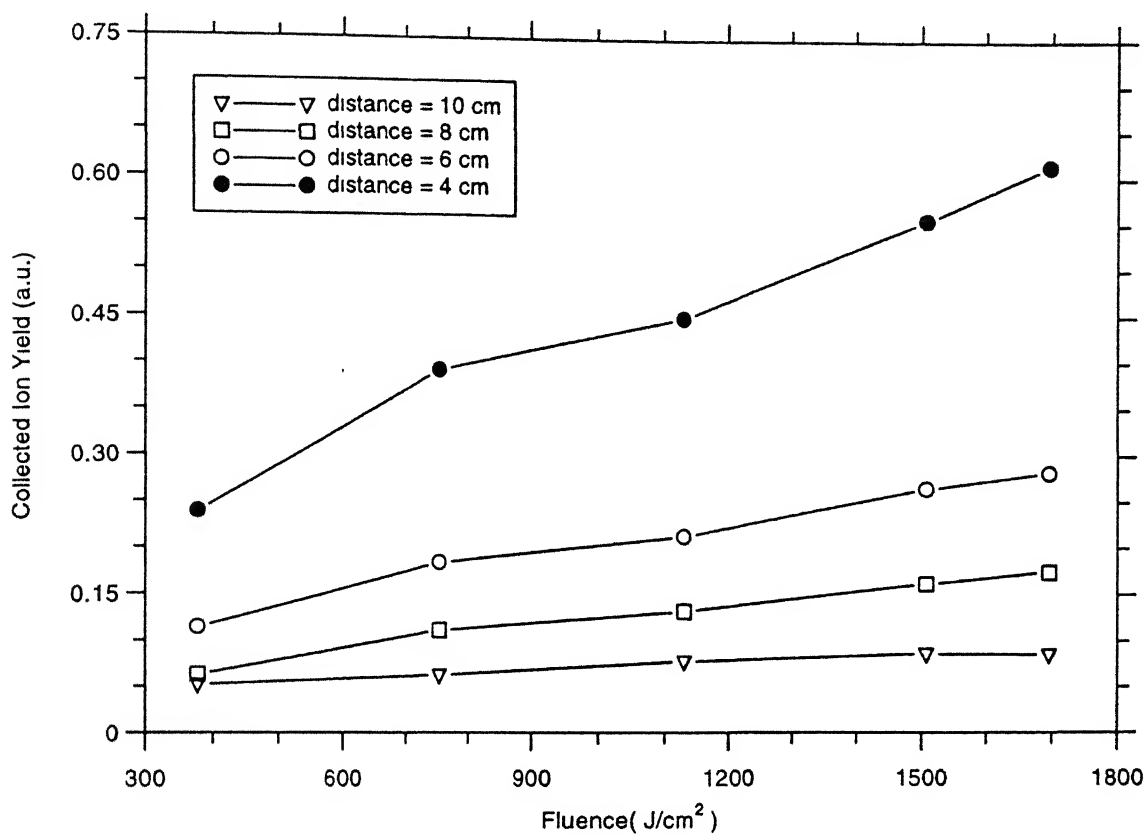
Fig. 3.21. Variation of ionic yield with laser fluence at various spatial
position of Faraday cup

It is worthwhile to mention here that the TOFMS is used perpendicular to the target, whereas Faraday cup is used at 45° to the incident beam. Hence, a correlation between the two diagnostics cannot be made with accuracy.

DEPOSITION AND CHARACTERIZATION OF THIN ALUMINUM OXIDE AND NITRIDE FILMS

A schematic of the experimental setup used for thin aluminum oxide and nitride film deposition is shown in figure 3.22. The focused spot at the target was 260 μm. The ablated aluminum was deposited on silicon substrates (010) placed at various distances from and parallel to the target surface in oxygen and nitrogen ambient at various gas pressures ranging from 10^{-2} to 100 Torr. The deposition time of 10 minutes for oxide films and 30 min for nitride films was kept constant.

Various techniques used for characterization of the thin films are listed in Table 1.1 (Chapter I). We have used Scanning Electron Microscopy (SEM), Energy Dispersive X-rays (EDX), X-Ray Diffraction (XRD), Raman spectroscopy and Rutherford Back Scattering (RBS) to characterize the deposited films.

Scanning Electron Microscopy

Scanning electron microscopy is one of the most widely used techniques for studying the structure and surface morphology of the deposited films. We used Scanning Electron Microscope (JEOL, JSM 840A) to investigate the morphology of the deposited films. The system has a resolution of 50 A^0. The characteristics x-rays produced when the incident electrons interact with the specimen can be used for microanalysis or elemental mapping. The x-rays generated in the analytical electron microscope are detected and stored by the Energy Dispersive Spectrometer (EDS); and are collected by a solid–state detector and sorted by a multi-channel analyzer, which is a part of the modern EDS computer system. The surface morphology of the deposited films showed a strong dependence on the target substrate distance.
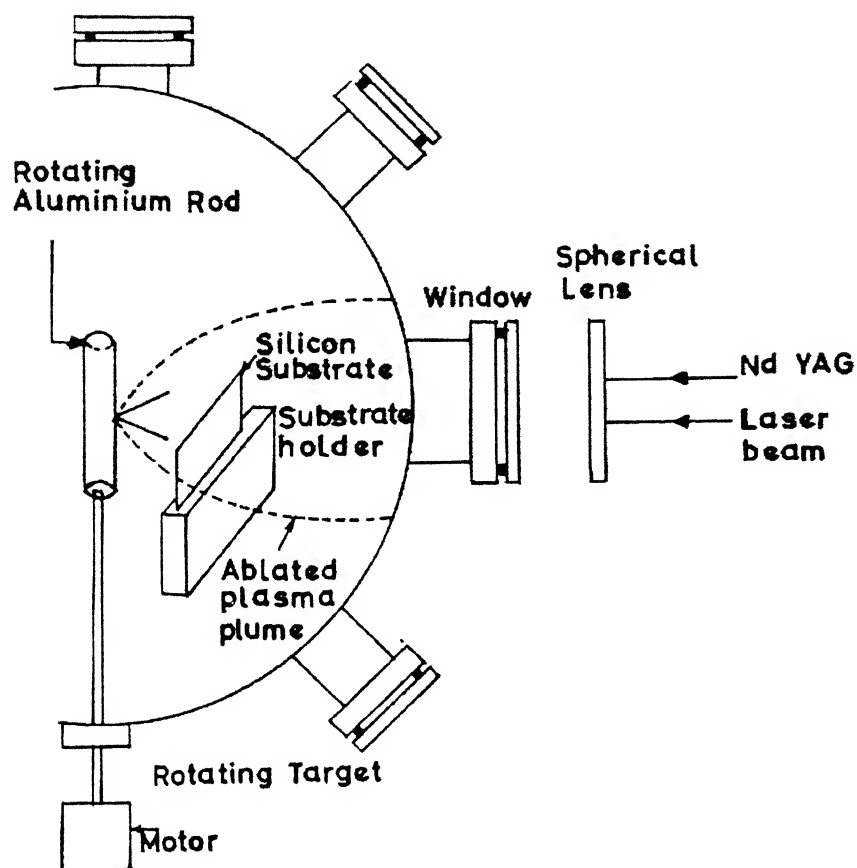
Fig. 3.22. Experimental setup used for deposition of thin films

X-ray Diffraction

To get the structural information, XRD patterns of the deposited films were obtained using an X-ray diffractrometer (Rich-Seifert, JSO-debyeflex 2002) with Cu-Kα source. The diffraction pattern gives the maxima in the intensity of the scattered x-rays. The position of the maxima provides information about the size and the shape of the unit cell while the width of the maxima can be used to measure its structural properties such as the size, orientation and strain of grains in polycrystalline materials.

Raman Spectroscopy

Raman spectroscopy has emerged as a very important technique in the characterization of thin films due to its ability to distinguish different bonding types, domain size and its sensitivity to internal stresses. The intensity of the Raman peaks is directly proportional to the concentration of the scattering species which provides a basis for quantitative analysis. We used linearly polarized 514.5 nm (Argon ion laser, Spectra Physics) laser radiation as the excitation source. The estimated laser power at the sample was 20 mW, focused to a 30 μm spot. A Spex-1877D Triplemate coupled with a photon counting system (with PMT and CCD) was used to record the spectra. The spectra are reproducible to within ± 2 cm^{-1} with a resolution of 2 cm^{-1}. The recorded micro-Raman spectra for the aluminum films deposited in oxygen and nitrogen ambient showed the presence of aluminum oxide and aluminum nitride.

Rutherford Backscattering Spectrometry

Rutherford Backscattering Spectrometry [227] is a well-established technique for determining the composition at the interface of two layers, identifying the mass of the impurity and the host atoms and thickness of the film etc. RBS is well suited for characterization of thin films or near surface region of bulk samples specially when the sample contains atoms of heavier species. In general, H$^+$, He$^+$ etc. ions in the energy range of 0.5 to 3.0 MeV are used for RBS. The well-collimated ion beam of size 1 mm^2 is made to impinge on the surface of the sample at an angle to the surface normal. The backscattered particles are detected using a semiconductor detector (EG&G ORTEC, USA) subtending a

small solid angle. The frequency of occurrence of the scattering as a function of energy of the backscattered particles, known as 'spectrum' is recorded by multi channel analyzer. Laser-ablated aluminum plasma was deposited on to a substrate as thin films and these films were investigated by RBS using 1.23 MeV He^+ beam obtained from 2 MeV Van de Graaf accelerator facility at IIT Kanpur. Experiments were performed in a clean vacuum of 1.5×10^{-6} Torr. The RBS spectrum was analyzed using the RUMP [228] simulation package. In simulation, firstly, a theoretical sample structure consisting of several layers of varying thickness is prepared. A backscattering spectrum is then constructed using this sample structure and the experimental parameters. This theoretical profile is then compared with that of the experimentally obtained RBS spectrum. The procedure is utilized in an iterative manner to arrive at a best set of parameters (sample structure) using which the given sample spectrum compares quite well with the experimental spectrum. The films with substrate at 2.0 cm were analyzed and were found to have correct stoichiometry for aluminum oxide, while for other films the stoichiometry was less. The thickness of the films was also calculated from the experimental data.

Chapter IV

DIAGNOSTICS OF LASER-ABLATED PLASMAS USING FAST PHOTOGRAPHY

To understand the process of laser ablation it requires an understanding of the various processes involved during the laser-target interaction, evaporation, plasma formation and its subsequent expansion in the ambient atmosphere. The ablation of the material depends upon laser characteristics such as the laser fluence, laser spot size, laser wavelength etc.. In the presence of an ambient atmosphere the hot vapor plasma interacts with the surrounding atmosphere in two ways. Firstly, the expansion of the high-pressure vapor drives a shock wave into the atmosphere, and secondly energy is transferred to the ambient atmosphere by thermal conduction, radiative transfer and heating by the shock wave. The nature of interaction is governed by the density, relative velocity, temperature, ion composition etc. of the plasma and background gas.

An important aspect of laser produced plasmas is the characteristic luminous plume. The spatial, temporal and spectroscopic dependence of the visible plume are a consequence of, and provide insight into, the processes of plume expansion in addition to laser-target, laser-plume, plume-ambient and plume-substrate interaction. Thus photography has emerged as one of the important diagnostic tools to study various features of expanding plasma. Fast photography using gated intensified ICCD has recently become very popular for laser-ablated plasma plume studies both in vacuum and gaseous background [82,84,85,92,95,99,100,102,105,107,111,112,115, 116, 136, 143, 176, 229-243] because of its high sensitivity. A very high sensitivity permits imaging of very fast emissions, not possible with ordinary photography. We report the study of the expansion dynamics of the laser-ablated aluminum plasma plume in different ambient gas environment and at different pressures using ICCD detector system. Time integrated, two-dimensional images of laser-ablated plasma plume are recorded with an ICCD system and are used to study spatial and temporal evolution of the expanding plasma.

EXPERIMENTAL SET UP

The experimental setup is discussed in Chapter III, figure 3.3. A Q-switched Nd:YAG laser (Spectra Physics DCR 4G) pulse (λ = 1.06 μm, 8 ns pulse width FWHM) delivering energy upto 1 J is focused by a spherical lens on to an aluminum target. The focal spot on the target was 260 μm. The target is mounted in a vacuum chamber which can be evacuated to a pressure better than 10^{-4} Torr. Target was continuously translated and rotated in order to avoid crater formation. Side on views of laser-ablated plume expansion of the overall visible emission from the plasma plume was recorded with an ICCD camera system (Princeton Instruments Inc., 576G/2). Experiments were carried out in different background gases (He,, N$_2$, Air, O$_2$, Ar) and at different pressures (10^{-3} - 100 Torr) from the target. The laser energies used in the experiment are 0.1-1 J/pulse

RESULTS AND DISCUSSION

The propagation of the laser-ablated plume in gaseous ambient is a complex hydrodynamic problem. Several authors have investigated the motion of plume in different ambient gases and at different pressures. To investigate and understand the behavior of the expanding plasma expansion process, the evaporation of the target material, formation of high-temperature plasma and the subsequent expansion in ambient gas is considered in detail.

Using gas dynamics equations, models have been proposed which describe temporal and spatial dependence of the plasma density, temperature and angular velocity distribution of the ejected particles. These models are tailored to give movement of the plume in the two lateral directions X, Y and in the direction Z normal to the target surface. In order to simulate the laser-ablated plume, we start with the discussion given in Chapter II. In the following relevant part is reproduced. The laser-interaction with target can be classified in four regions: (i) unaffected bulk target, (ii) evaporating target surface, (iii) region close to the surface absorbing the laser beam and (iv) rapidly expanding outer edge of the plume, transparent to the laser beam and were discussed in detail in Chapter II. Figure 2.2 shows different phases present during laser irradiation of target. The second and the third regimes start with the laser pulse and continue till the laser pulse duration. While the fourth regime

starts after the termination of the laser pulse. In this regime, no particles are evaporated or injected into the inner edge of the plasma. The thermal energy rapidly gets converted into kinetic energy and hence the plasma attains very high expansion velocities. The expansion can be considered as adiabatic. On the basis of the above assumptions Singh et al [19] have reported a flow model for the formation of high temperature and high-pressure gaseous plume in the vicinity of the target surface. It is assumed that the initial expansion is unaffected by the presence of ambient gas. The effect of gas is significant after a certain time when the collision between the ambient gas and the plasma constituents is appreciable. We have used the equations of continuity and motion to transform the expansion for time dependent density, pressure and velocity that gives the dynamics of the plume's maximum density boundary $(X(t), Y(t), Z(t))$ during isothermal expansion (Chapter II)

$$X(t)\left[\frac{1}{t}\frac{dX}{dt}+\frac{d^2X}{dt^2}\right]=Y(t)\left[\frac{1}{t}\frac{dY}{dt}+\frac{d^2Y}{dt^2}\right]=Z(t)\left[\frac{1}{t}\frac{dZ}{dt}+\frac{d^2Z}{dt^2}\right]=\frac{k_BT_1}{m}, \qquad t<\tau_L$$

2.11

where τ is the laser pulse width and T_1 is the isothermal temperature of the plume. The initial dimensions are of the order of 260 µm in transverse direction depending upon focused spot whereas in the longitudinal direction it is less than 1 µm.

After the termination of the laser pulse the plasma expansion is assumed to be adiabatic. Thus equating the plume's internal energy to the total isothermal energy in plume's volume at the end of the laser pulse, we arrive at (Chapter II),

$$X(t)\left[\frac{d^2X}{dt^2}\right]=Y(t)\left[\frac{d^2Y}{dt^2}\right]=Z(t)\left[\frac{d^2Z}{dt^2}\right]=\frac{k_BT_1}{m}\left[\frac{X_0Y_0Z_0}{X(t)Y(t)Z(t)}\right]^{\gamma_1-1} \qquad t\geq\tau_L$$

2.17

where X_o, Y_o, Z_o are solutions for the plasma boundary at the end of the isothermal region. The equations are solved numerically using Runge-Kutta iteration technique. For the initial expansion (i.e., in the isothermal region) the spot size of the laser beam on the target (260 µm in our case) is taken to be the boundary condition. The simulated velocities and dimensions of isothermal regime are taken to be the initial boundary conditions for

adiabatic region. From these simulations one can evaluate the dimensions of the plume at various time steps. We considered the evolution of Al-plume boundary at 50, 100, 200 and 500 ns in presence of ambient gases. The result of simulation is shown in figure 4.1. For times $\leq$ 1 ns (figure 4.1 inset) the expansion is more in the X and Y direction, while it is less in Z-direction. As the time progresses the expansion in Z-direction increases and after some time (few ns after the termination of laser pulse) the expansion in Z-direction is much larger than the expansion in X and Y-directions. Side on view of the expanding plume is imaged using ICCD camera system. The position of the plume front is located by comparing the observed plume front with the theoretical simulated front. It is found to be in good correlation as shown in figure 4.2. Figure 4.2 shows an ICCD image taken at 100 ns delay with respect to laser pulse and a simulated plume front. Figure 4.3 shows the intensity contour corresponding to ICCD image of figure 4.2 and it shows the variation of intensity as the plume progresses. Figure 4.4 shows the variation of plume's front edge with time at 10 mTorr pressure of He, Ar, Air and O_2 at laser energy of 900 mJ/pulse. From the slope of the curve at different time one can determine the velocity of the expanding front.

An interesting feature of the above model is the predicted greater extent of the plume expansion in the direction where the laser spot size is the least (along Z-axis in our case). Similar behavior is observed for a non symmetrical focus spot giving larger velocity in the direction where the spot is smaller at the beginning [19]. Thus, if the dimension of the focus spot are in the order $X_o > Y_o > Z_o$ in beginning then the order of displacement of the plume with respect to time will be in the order $X_o < Y_o < Z_o$. Figure 4.5 shows the plot of displacement of plasma front along Z- and X-axes respectively with time. It is observed that the displacement of the front is more in Z-axis as compared to X/2 (= Y/2, for circular spot) axis. This gives rise to the characteristic balloon shaped (elliptical) plume elongation outward from the surface. However, depending on the pressure of an ambient gas the shape of the plume can be spherical, figure 4.6. Similar behavior is observed for all the ambient gases used at various ambient gas pressures and at various delay times with respect to the irradiating laser pulse. Based on the displacement time plots the expanding plasma can be divided into three regions, (1) the region near the target where the ejected particles move with supersonic velocities unaffected by the ambient atmosphere or free flight zone (to the extent of Knudsen layer), (2) the region in which these particles slow down and start
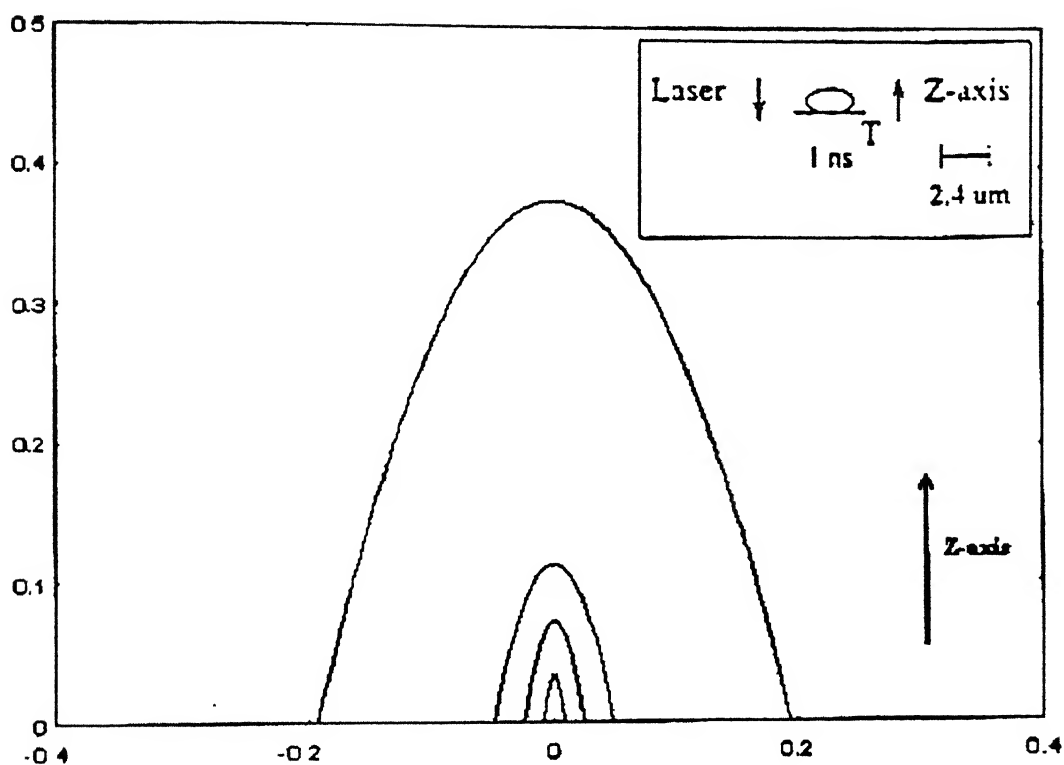
Fig. 4.1. Computer simulated Al-plume front along Z-axis for time delays of 50, 100, 200 and 500 ns. Inset is the computer simulated plume shape for time delay of 1 ns, T is the position of the target
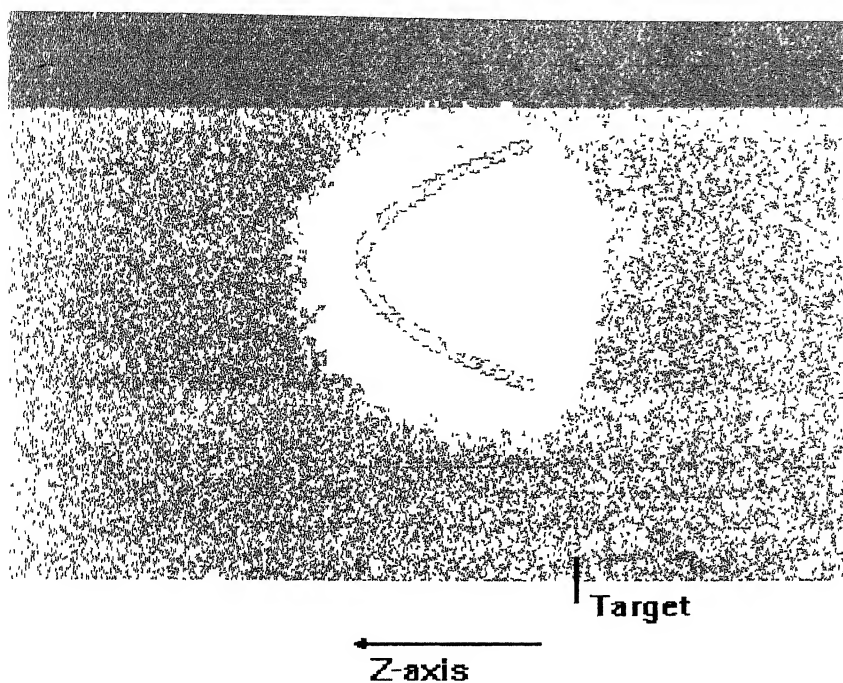
Target

Z-axis

Fig.4.2. Comparison of computer simulated plume front (□) and ICCD image recorded at time delay of 100 ns for laser-ablated Al-plume at a pressure of 100 mTorr of air
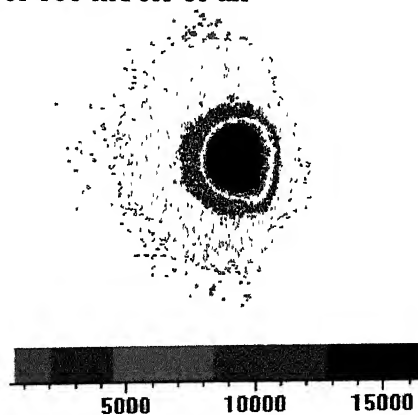

5000   10000   15000

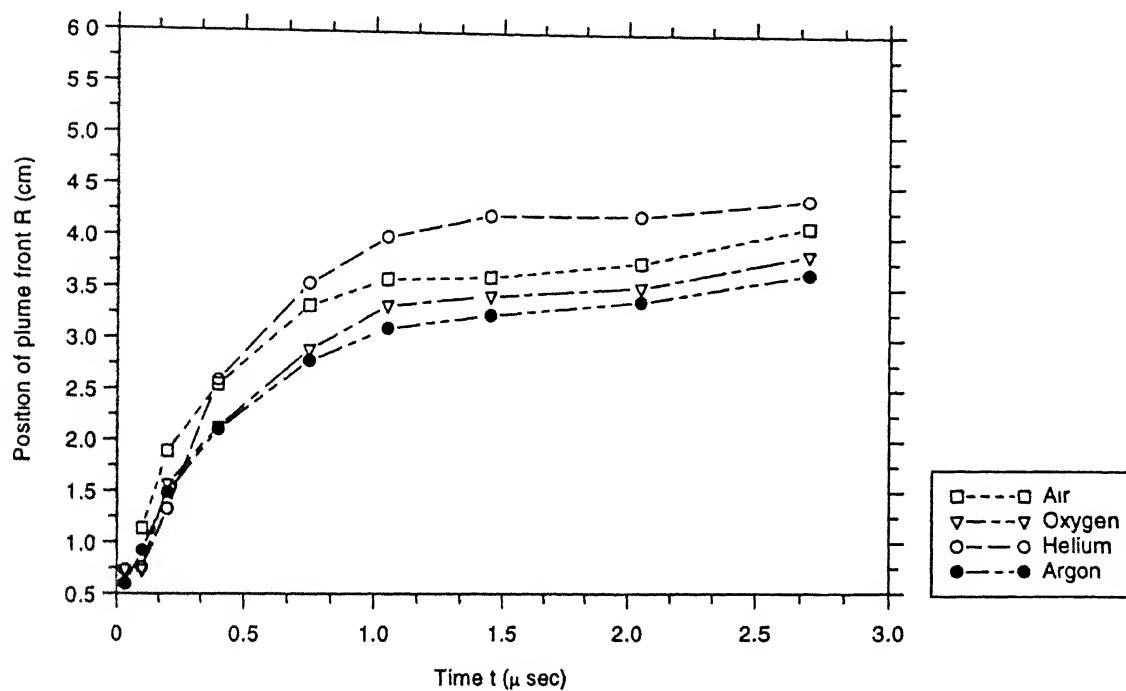Fig. 4.3. Intensity contour corresponding to fig. 4.2

Fig. 4.4. Variation of plume front position R of aluminum plasma with time t at 10 mTorr of ambient pressure of He, Ar, Air and O_2 at laser irradiation of 2.16×10^{11} W/cm^2
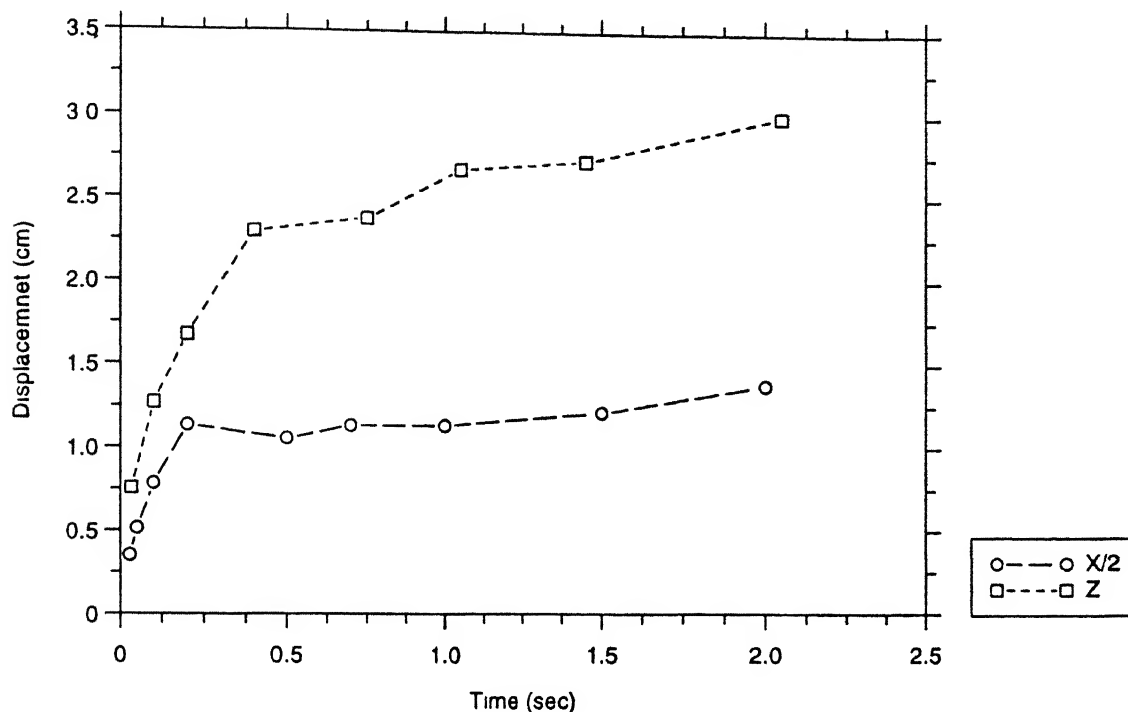
Fig. 4.5 Displacement-time plot for expanding plasma front along Z and X-axis in ambient atmosphere of oxygen at a laser irradiance of 2.4 x 10^{10} W/cm^2

50 ns

Argon ambient
100 mtorr

50 ns

Vacuum [<1 mTorr]

Fig. 4.6. Comparison of the shape of plume in vacuum and in argon atmosphere 50 ns after the ablating pulse at 100 mTorr

moving with increasing linear velocity and are affected by the background pressure and the nature of the gas (vaporized region) and (3) the region in which the ejected particles stop moving.

In order to get good quality films on the substrate, it is imperative to understand the evolution of the ablated plume. To investigate the expanding plume, we imaged the expanding aluminum plasma at various time delays with respect to the ablating pulse (figure 4.7 (a) in helium ambient & (b) in argon ambient) using ICCD, at various irradiances, in different ambient atmosphere (He, Ar, O and air) at various pressures. The displacement of the luminous front with respect to target initially increases with time and then becomes more or less constant at larger distance. A similar behavior was observed for all pressures and ambient atmosphere. The velocity of the plume front can be estimated from displacement of plume front (R) and time plot, figure 4.4. Figure 4.8 shows the variation of velocity with time of aluminum plume front at 10 mTorr pressure of He, Ar, O_2 and air. The velocity of the expanding front in various ambient environments (for He, Air, O_2 and Ar at 10 mTorr at 100 mJ of laser energy) is estimated to be 7.29 x 10^6 cm/sec, 6.84 x 10^6 cm/sec, 6.75 x 10^6 cm/sec and 6.21 x 10^6 cm/sec, respectively. It is observed that the velocity (dR/dt) of the plume front (figure 4.8) is maximum for expansion in helium and minimum for Argon background gas. This is attributed to greater degree of freedom per unit mass of helium than any other gas used in the experiment and hence the collisional volume of helium is less as compared to that of other gases. Thus, emitted species travel larger distances in helium atmosphere followed by air, oxygen and least for argon. The velocity of the expanding front is estimated to be 6.75 x 10^6, 5.53 x 10^6, 4.86 x 10^6 and 4.05 x 10^6 cm/sec for 10 mTorr, 100 mTorr, 10 Torr and 100 Torr respectively of ambient pressure of oxygen and 100 mJ of laser energy. The velocity of the expanding front decreases with increase in ambient gas pressure. This is attributed to the drag force, and will be discussed later. The measured velocity is used to calculate the vapor density, temperature and pressure using the hydrodynamic relations of adiabatic shock expansion.

Assuming that vapor pressure far exceeds the ambient pressure, which is true in our case, the maximum velocity attainable is given [244] by V_{max}:

$$V_{max}= 2a_o/(\gamma_1-1) \hspace{3cm} (4.1)$$

50 ns

100 ns

200 ns
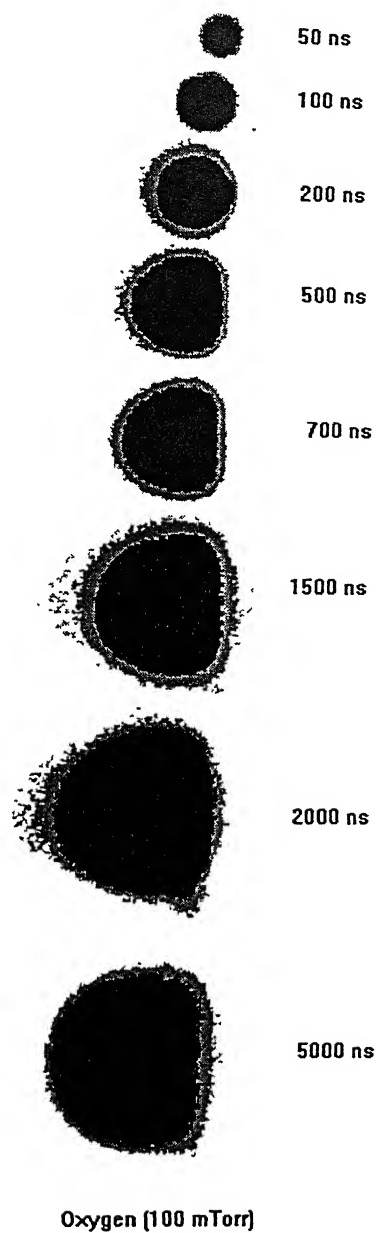
500 ns

700 ns

1500 ns

2000 ns

5000 ns

Oxygen (100 mTorr)

Fig. 4.7 (a) Typical ICCD photographs of laser-ablated aluminum plume in oxygen ambient at 100 mTorr at laser irradiance of 2.4×10^{10} W/cm^2
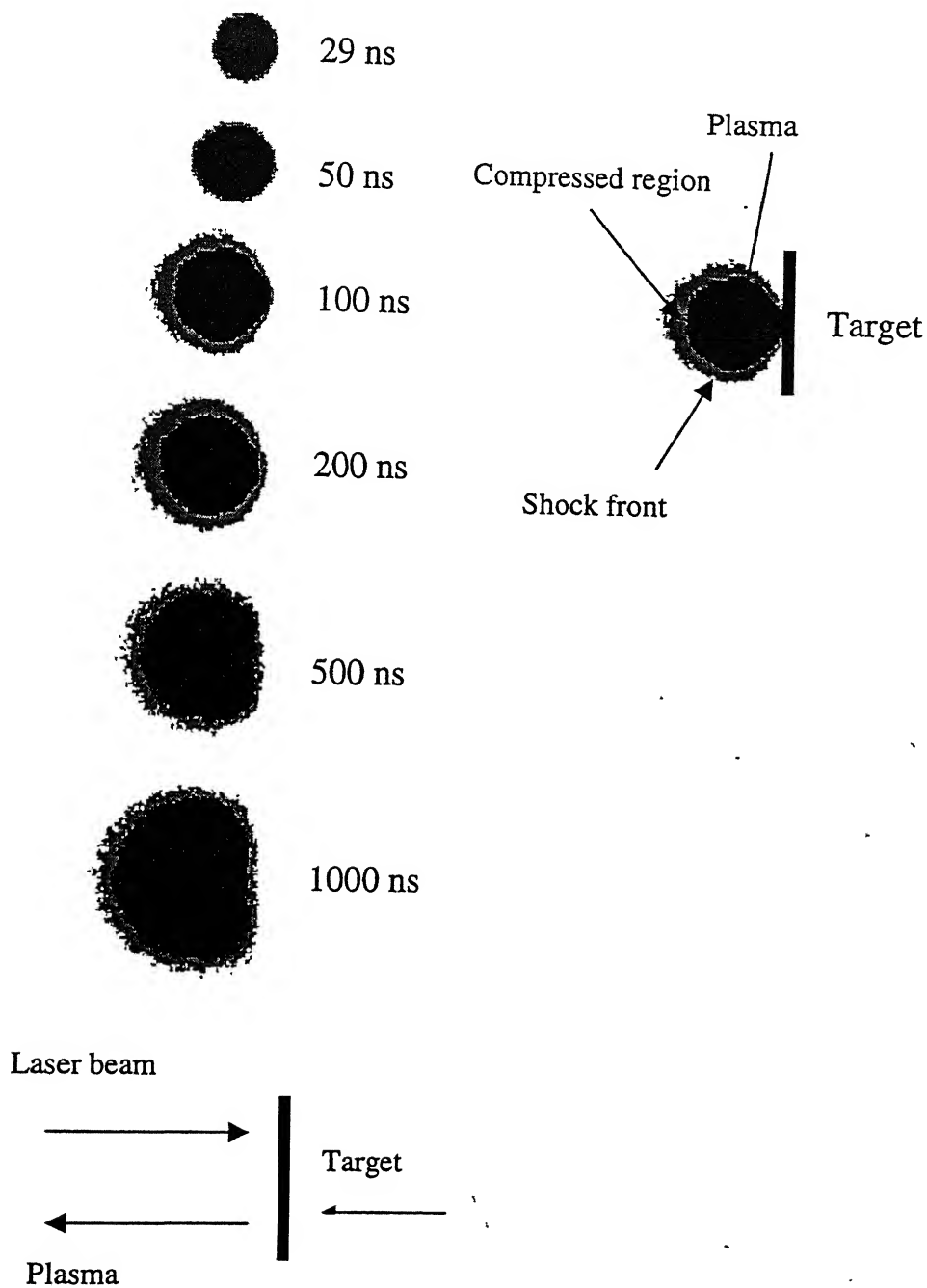
Fig. 4.7 (b) Typical ICCD photographs of laser-ablated aluminum plume in argon ambient at 100 mTorr at laser irradiance of 2.4 x 10^{10} W/cm^2
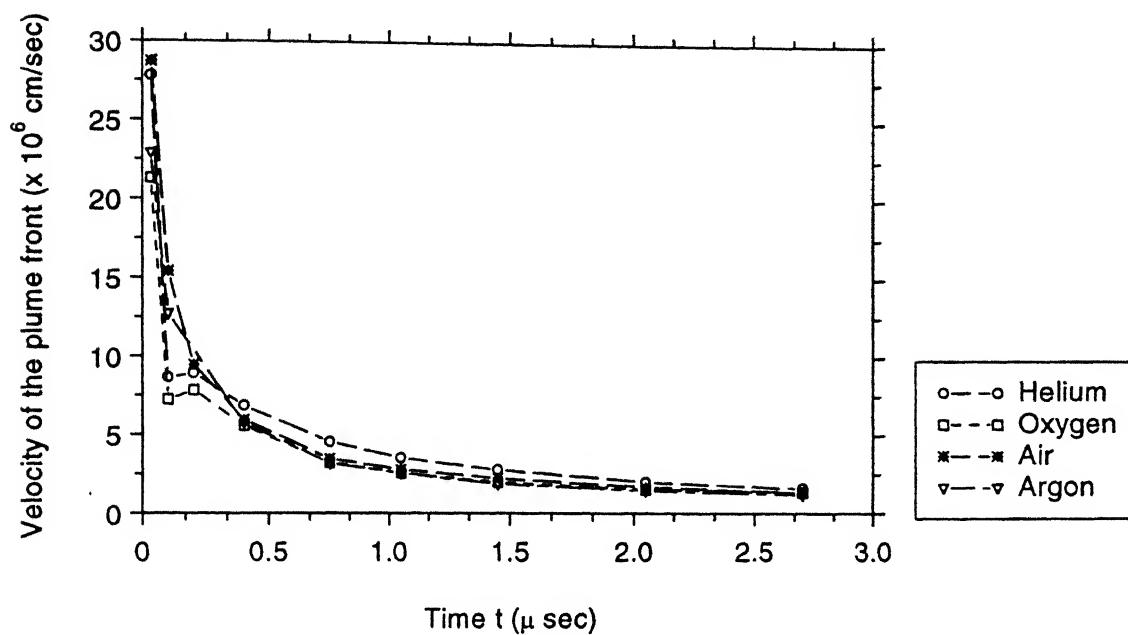
Fig. 4.8. Temporal variation of velocity of a laser ablated Al-plume for various ambient environments at a pressure of 10 mTorr and laser irradiance of 2.16 x 10^{11} W/cm^2

where a_o is the speed of sound [$a_o = (\gamma_1 k_B T_{su}/m)^{1/2}$]. Eqn. (4.1) is used to estimate the surface temperature T_{su} of the target, here γ_1 is the specific heat ratio of the vapor and m the mass of the vapor. The maximum velocity of the front is estimated with respect to displacement of the front at earlier times and close to the target. It is found that for an ambient pressure of 10^{-2} Torr and laser irradiance of 1.65×10^{11} W cm^{-2}, the velocity of the front is maximum (V_{max}) for helium (2.78×10^7 cm/sec), followed by air (2.66×10^7 cm/sec), oxygen (2.31×10^7 cm/sec) and argon (2.29×10^7 cm/sec). From the values of temperature at the surface of the target ($\sim 1.18 \times 10^6$ K) obtained one finds that these temperatures are much greater than the sublimation temperatures (~ 8500 K) of the metal and hence one can infer that no superheating of the surface can occur above the normal vaporization temperature.

As the pressure of the ambient gas is increased the expanding front slows down and hence the velocity of the front decreases. On increasing the ambient gas pressure the backward pressure on the plasma increases and as a result the velocity of the plasma front decreases and hence the vapor pressure. This is evident from our experimental observations of decreasing plume expansion with pressure of ambient gas, figure 4.4. Furthermore, the gas near the target is compressed by the ablated species leading to the breakdown of the continuity of the surrounding gas. The formation of the discontinuity in the gas is called a shock wave. The shocked region (discontinuity) at the interface of the vapor and the ambient gas weakens the backward pressure applied by the ambient gas. According to blast wave model a rapidly expanding plume in a background gas behaves like a piston which generates a shock wave in the ambient. The ambient gas is compressed into a thin shell between the shock and the plume front. The shock front expands and sweeps the background gas. The model holds reasonably well for higher pressures, however, it does not explain the observed deceleration of the plume. The deceleration may be accounted for by using drag model, the plume experiences a resistive force due to collision with the background gas which eventually stops the plume expansion as depicted in figure 4.7.

Consider the ablation of aluminum in various ambient environments, at different laser energies and at various pressures. Knowing the speed of the front at different time from R-t plot and using the following mass and momentum conservation equations, one can determine ρ_v, P_v and T_v (eqn.'s 2.34, 2.35, 2.36, Chapter II):

$$\rho_1 = \rho_o (1 + 1/\gamma_1) \qquad (2.34)$$

$$P_1 = 2 \rho_o u_1^2 / (1 + \gamma_1) \qquad (2.35)$$

$$T_1 = P_1 / (R_g \rho_1) \qquad (2.36)$$

Consider the motion of the plume front along the Z-axis. Figure 4.9 and 4.10 show the temporal variation of the displacement (R) of the laser-ablated aluminum plume front derived from ICCD images for different pressure of the ambient gas and at various laser energies respectively. The displacement of plasma front decreases with increase in pressure of the ambient gas showing essentially that the plasma is getting confined to a smaller region with the increase of the background pressure from 1 mTorr to 100 Torr at fixed laser energy, figure 4.9. The dimensions of the plume increase with the increase in laser energy for a given pressure as shown in figure 4.10. It is due to increase in the plume pressure as laser energy coupled to the target increases.

The condition for the formation of shock between the ambient gas and ablated species is that the thickness of the shocked region should be greater than the mean free path of the ambient gas. Mean free path in undisturbed He, Ar, Air and O_2 are $9.6 \times 10^{-3}/P_o$, $6.01 \times 10^{-3}/P_o$, $5.36 \times 10^{-3}/P_o$ and $5.95 \times 10^{-3}/P_o$ cms respectively, here P_o is the ambient gas pressure in Torr. This shows that for higher pressures the possibility of formation of shock is more as compared to that of lower pressures. Also if at all the shock develops for low pressures it will be generated far away from the target surface. If we consider our expansion to be conical at earlier times with vertex at the focusing point of the laser beam and spherical at later times, the shock thickness (Δ) and shock temperature (T_{sh}) are given by (eqn. 2.21 and 2.22, Chapter II):

$$\Delta = \begin{cases} R\left[\left(\dfrac{2\gamma_1}{\gamma_1 + 1}\right)^{1/3} - 1\right] & \text{for conical expansion} \\[3em] R(\gamma_1 - 1)/3(\gamma_1 + 1) & \text{for spherical expansion} \end{cases} \qquad (2.21)$$
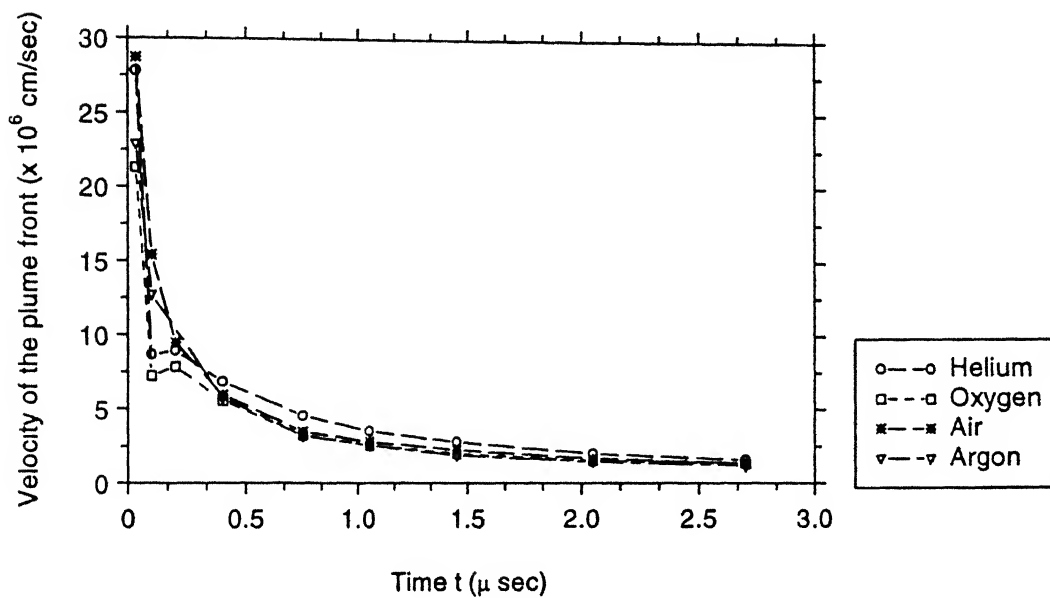
Fig. 4.9. Temporal variation of plume front edge at various pressure of oxygen at laser irradiance of 2.16×10^{11} W/cm^2
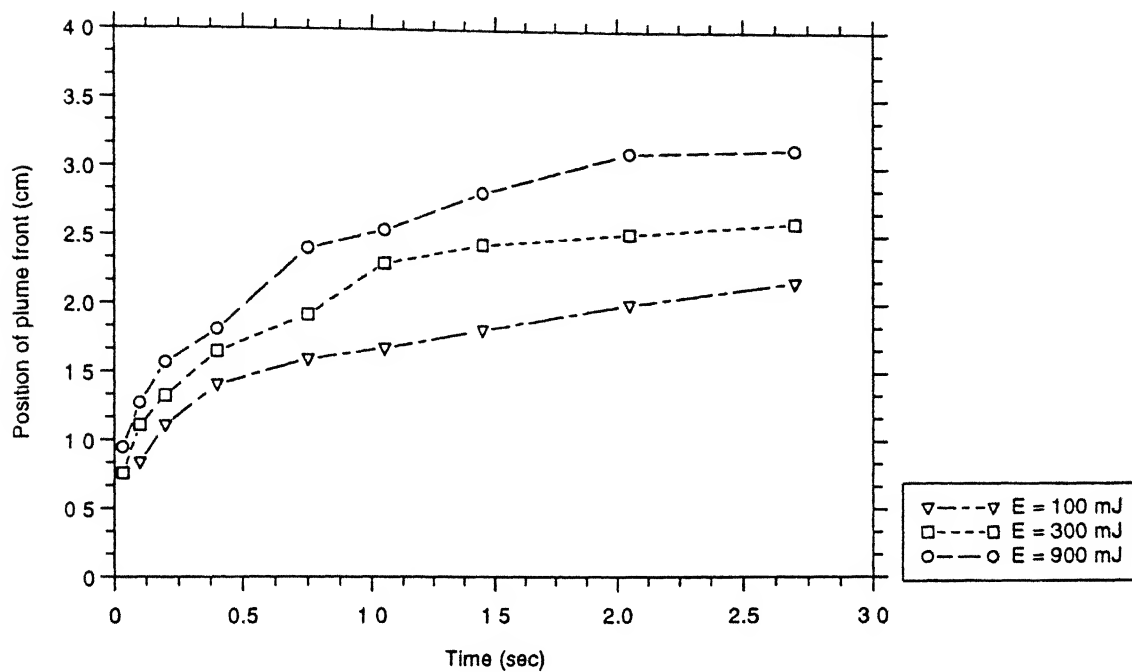
Fig. 4.10. Temporal variation of plume front edge at different laser energy

and $\qquad$ $$T_{sh} = \frac{2\gamma_1}{\gamma_1 + 1}\left[\frac{(\gamma_1 - 1)}{(\gamma_1 + 1)}M_a^2 + 1\right]T_o \qquad\qquad (2.22)$$

where M_a is the mach number ($=v_f/a_o$), a_o is the speed of sound, and is estimated to be 3.17 for region within 100 ns after ablating pulse. From the values of temperature and density of the shocked gas one can estimate the extent of diffusion. Diffusion coefficient and diffusion range are defined as (eqn. 2.23 and 2.24, Chapter II)

$$D = D_o (T_s/T_o)^{5/4}(\rho_o/\rho_{sh}) \qquad\qquad (2.23)$$

$$D_r = (4Dt)^{1/2}, \qquad\qquad (2.24)$$

where D_r is the diffusion range, t is the time. D_o for He, Ar, Air and O_2 is 1.601, 0.169, 0.165 and 0.2 cm^2 s^{-1} respectively [245]. The diffusion of the gas into the compressed region increases with time. It follows from the above arguments that some of the plasma material is also transported inside the compressed region and since the temperature of the shocked region is high, the particles inside the shock can undergo physical and chemical changes. Thus in case of laser-ablated plasma of metals in oxygen it is possible to obtain metal oxides. Whereas the laser-ablated plasma of organic compounds [28] results in fragment of C-N, C_2, CH etc. The effect of the ambient gases on these fragments can be inferred spectroscopically [105].

Knowing the velocity from R-t plot, the thickness of the shocked region was estimated. It is observed that the thickness of the shocked region increases with time, as the mass of the gas encompassed by the shocked region increases. With increase in ambient pressure the thickness of the shock decreases. The decrease may be due to no change in the pressure inside the plasma whereas the ambient pressure has increased, the ambient gas tries to diffuse into the shocked region and thereby decreases its width. On comparing the temperature of the shocked (compressed) gas with that of vapor temperature, it is observed that the shock temperature ($\sim 1.922 \times 10^6$ K in 100 mTorr of oxygen at 50 ns after the ablating pulse) is higher than the vapor temperature ($\sim 2.089 \times 10^5$ K in 100 mTorr of oxygen at 50 ns after the ablating pulse). This can be attributed to collisions occurring at the interface of the shocked gas and plume on one side and the ambient gas and the shocked gas on the other. Thus, at a distance (plume length) where the plasma pressure equals the

ambient pressure, probability of collision of gas particles with that of vapor is very high. These collisions are also responsible for the plume broadening as observed in ICCD images, figure 4.7. Since the temperature of the shocked region is higher than that of plume (vapor) temperature for all times and pressures implies a greater probability of chemical reaction at the edge. The collisions of the plasma species with that of ambient gas and higher temperature of the shocked region induce chemical changes at the interface and result in the formation of metal oxides/nitrides and clusters, depending upon the target properties and the ambient atmosphere.

Figure 4.11 and 4.12, shows the variation of plume pressure with time and ambient gas pressures (for oxygen), respectively. The plasma vapor pressure decreases with time i.e., with the expanding front and decreases with increase in ambient gas pressures and is true for all the other ambient gases used in this experiment. It is observed that at any given pressure the plasma temperature decreases with increasing time (or distance from the target). The temperature near the target is $\sim 10^6$ K (50 ns after the plasma initiation) and is found to remain unaffected with the increase of pressure. However, after 100 ns it is observed that the vapor temperature starts decreasing with the increase of ambient gas pressures. The decrease of the plasma temperature with oxygen pressures may be due to the difference of the heat capacities of the plasma species and that of oxygen. Figure 4.13 shows the variation of vapor temperature with the pressure of oxygen. The heat capacity strongly depends upon the density of each species. In our experiment we determined the density of plasma species by measuring the Stark broadened profile [85] of Al II (4p ^{1}P^o-4d ^{1}D) transition at 559.3 nm. Figure 3.11, shows the variation of plasma density with axial distance at an ambient pressure of 100 mTorr. The plasma density at 2 mm from the target is found to be $\sim 1.69 \times 10^{16}$ cm^{-3}. It is much larger than that of ambient oxygen density $\sim 3.2 \times 10^{15}$ cm^{-3}. It implies that at distances near the target the plume is hardly affected by the presence of the ambient gas, the plume expansion is similar to free expansion in vacuum. It justifies our earlier assumption that the expanding plume is conical in the initial stages of the expansion. With the increase in distance from the target surface the plasma density decreases [18] as $n_e = n_o(t)\left(1 - \dfrac{z}{Z(t)}\right)$, where n_o is the density at the centre of the laser irradiated spot (z = 0) at time t, the z coordinate is directed perpendicular
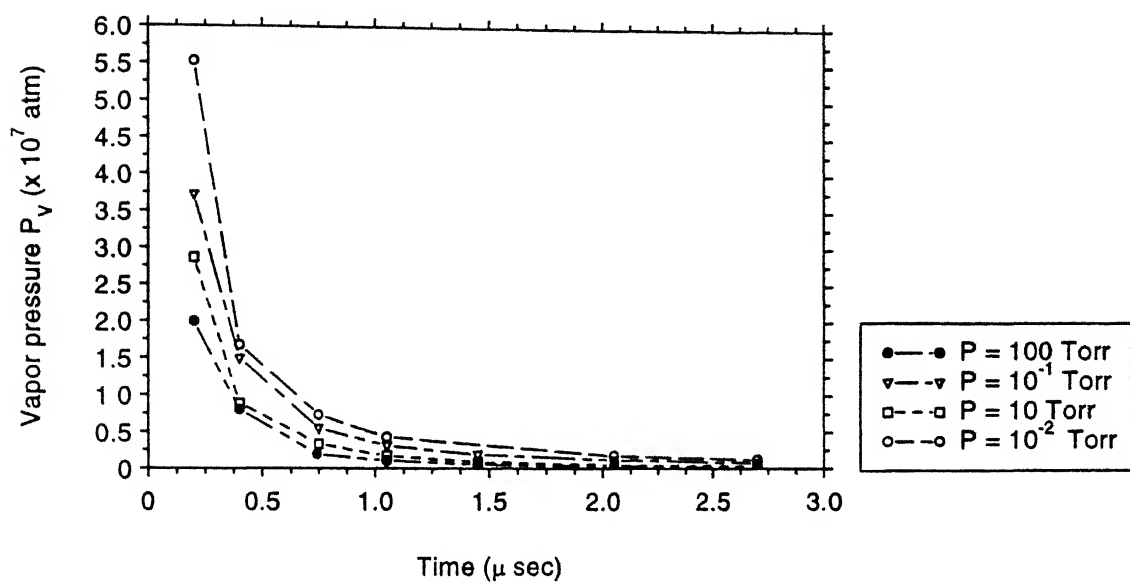
Fig. 4.11. Temporal variation of vapor pressure with oxygen gas pressures at laser irradiance of 2.4×10^{10} W/cm^2
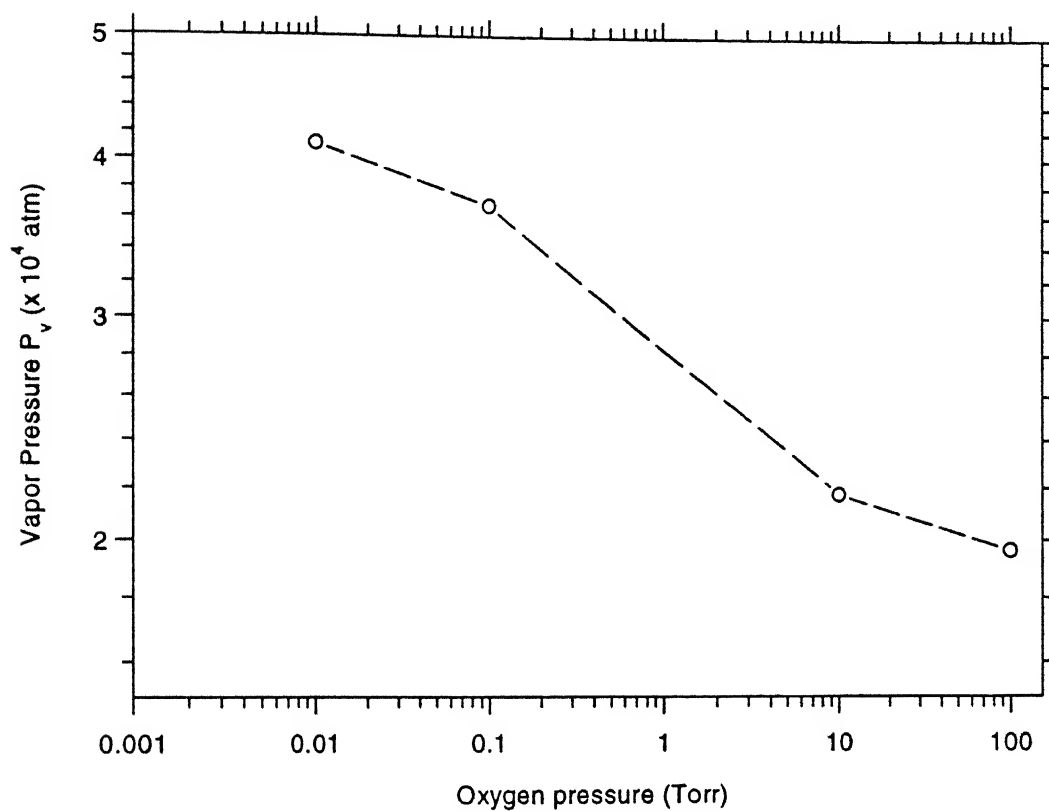
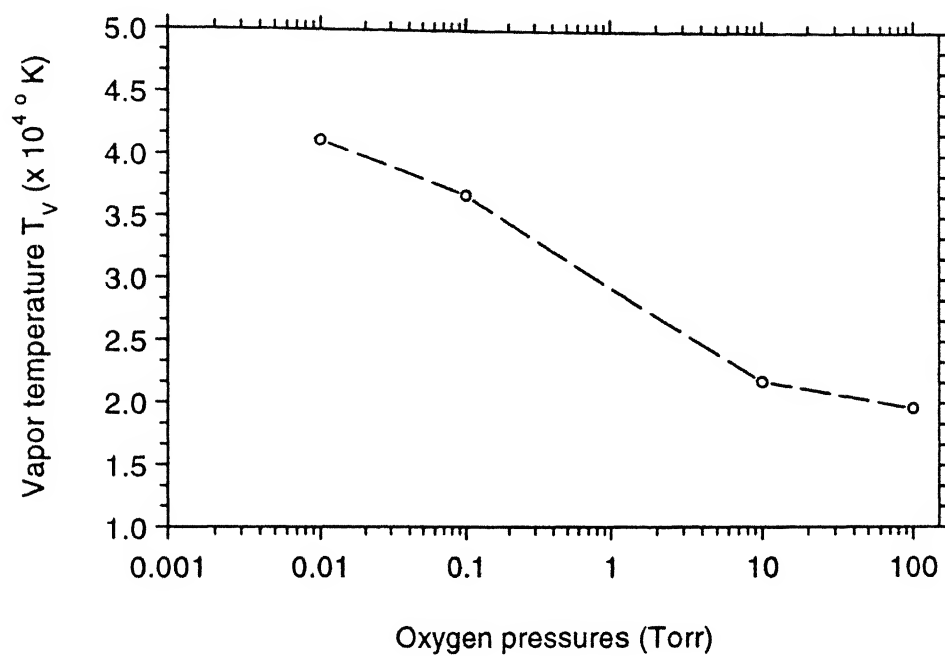Fig. 4.12. Variation of vapor pressure with ambient gas pressure at laser irradiance of 2.4×10^{10} W/cm^2

Fig. 4.13. Variation of vapor temperature with oxygen gas pressure at laser irradiance of 2.4×10^{10} W/cm^2

to the target and Z(t) refers to position of the leading edge of the plasma. At larger distances the density of the plasma falls sharply and attains a value below the density of ambient oxygen i.e., the heat capacity of the ablated species becomes smaller than that of the oxygen.

To explain the experimental observation of finite propagation of the plume in an ambient atmosphere we used drag model. As stated, the plume progressively slows down and eventually comes to rest due to the drag force. The position of the plume edge is given by eqn. (2.46),

$$x = X_{max} \{1 - \exp(-\beta t)\} \qquad (2.46)$$

where, X_{max} is called the stopping distance. The above equation can also be written as

$$x(t) = X_{max} [1 - e^{-t/t_o}] \qquad (4.2)$$

where $t_o = 1/\beta$ is the time constant at which the velocity drops to $1/e$ of its initial value.

Figure 4.14 shows fit of eqn. (2.46) to the experimentally observed plume front, which leads to the determination of X_{max}, the stopping distance at various pressures. It is observed that the stopping distance (X_{max}) of plume for the ambient pressure of 1 mTorr is maximum, while it is least for 100 Torr, in all ambient gas environments. If we compare the stopping distances in terms of background gas at same pressures one observes that the stopping distance in case of He (3.19 cm) is largest and is least for Ar (1.82 cm). As the viscous force increases the displacement of the plume front decreases. On increasing the ambient gas pressure the backward pressure on the plasma towards the target increases and as a result the expansion velocity decreases. While observing the images one finds that as the pressure increases, the stopping distance decreases and there is an increase in intensity of the plume. This is due to confinement and collision of the plasma particles in a small region, which results in the increase in emission intensity. Hence, one of the controlling parameters 'stopping distance' or 'plume length' which defines the film characteristics, can easily be estimated from real time observations. The value of stopping distances for Al-plasma in various gases and ambient pressures are listed in Table 4.1.
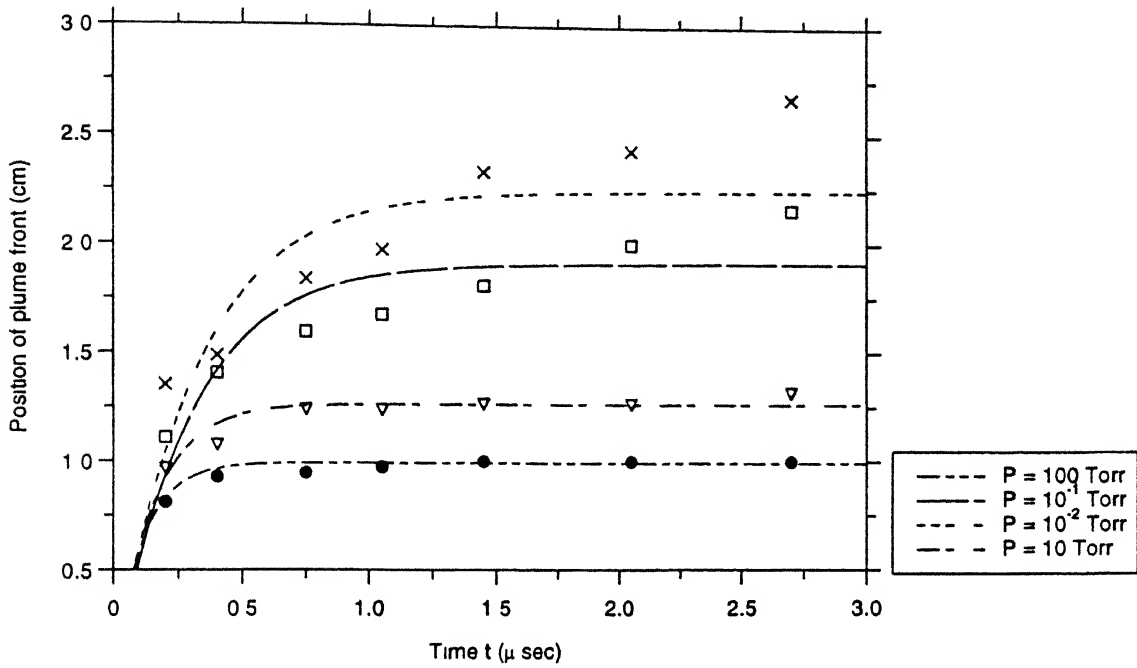
Fig. 4.14. Plot of eqn. $x = X_{max}\{1-\exp(-\beta t)\}$ (dashed line) and experimentally observed variation of plume front edge with time for various pressures of oxygen (data points)

Table 4.1.

Plume length (or stopping distance) in various ambient atmosphere and at various pressures at laser irradiance of 2.4 x 10^{10} W/cm^2

Ambient	Stopping distance (X_{max})				
	10^{-3} Torr	10^{-2} Torr	10^{-1} Torr	10 Torr	100 Torr
Argon	4.622	4.145	1.671	1.311	0.753
Oxygen	4.503	4.417	2.046	1.358	0.845
Air	4.905	4.836	2.960	1.377	0.992
Helium	5.851	5.234	5.420	1.768	1.033

On increasing the fluence, (at lower ambient pressures) though the velocity of the luminous front increases the value of the shock temperature remains larger than the value of vapor temperature. However, on increasing laser irradiance to 1.65×10^{11} W/cm^2 at background pressures higher than 10 Torr, breakdown of the ambient gas is observed (air, oxygen and argon). No breakdown is observed for same energies and pressures lower than 10 Torr. Figure 4.15 (a) shows the breakdown of oxygen at 100 Torr of pressure with laser irradiance of 1.65×10^{11} W/cm^2. The blob close to target is aluminum plasma and second blob corresponds to breakdown of oxygen. The maximum intensity of first and second blob in figure 4.15 (b) occurs at 0.7 cm and 1.2 cm respectively from the target surface. Since this breakdown is observed at the extremities of the plume (edge) it appears that the high shock temperature might be responsible for the breakdown of the gas. However, the possibility of high energetic electrons (cascade breakdown and thermal run away, discussed in Chapter II) from the target ionizing the ambient gas cannot be ruled out [21]. At the irradiance used in our experiment such a possibility is very low. On focussing laser beam with an irradiance of 1.65×10^{11} W/cm^2 in only O$_2$ at 100 Torr pressure no breakdown of oxygen was observed, as reported earlier [245]. Similar results are obtained with nitrogen at an ambient pressure of 100 Torr and moderate laser intensities, figure 4.16.

The blast wave theory predicts the position of the shock front R as (eqn. 2.48, Chapter II)

$$R = \xi_o \, (E_o/\rho_o)^{1/5} \, t^{2/5} \qquad\qquad (2.48)$$

From the propagation distance R, dR/dt the speed of propagation can be estimated. It follows from eqn. (2.48) that for a particular experimental condition ξ_o, E$_o$ and ρ_o being fixed, R can be written as $R = K_l^{0.2} \, t^q$, where K$_l$ is a constant. The exponent q can be taken as a parameter which can be varied to fit the theoretical curve to experimental data. Figure 4.17, shows the fit of eqn. to the experimentally observed data, one notices that the model is best fitted for $0.22 \le q \le 0.28$ for 100 mTorr pressure of argon, oxygen and air, whereas q = 0.47 for He. For ideal blast wave one expects q = 0.4. The discrepancy observed in the exponent q may be due to instability, which grows at moderate laser intensities and high pressures.
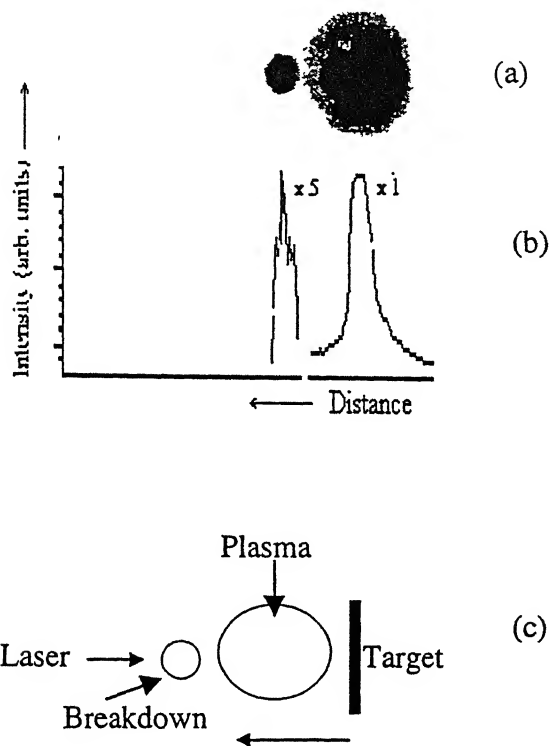
Fig. 4.15. (a) An ICCD image showing the breakdown of oxygen at 100 Torr at
laser irradiance of 1.65×10^{11} W/cm^2,
(b) Intensity profile of (a), maximum intensity of first and second
peak occurs at 0.7 cm and 1.2 cm respectively,
(c) Schematic showing the plasma and breakdown lobes

Nitrogen Breakdown
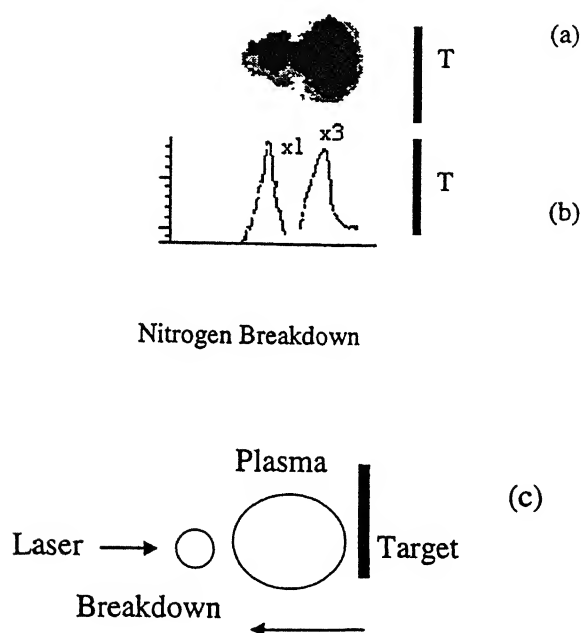
Fig. 4.16. Breakdown of Nitrogen at a pressure of 100 Torr at laser irradiance of
1.65×10^{11} W/cm^2,
(a) ICCD image, showing the breakdown of nitrogen gas
(b) Intensity profile of (a) showing relative intensity of the peaks, and
(c) Pictorial representation of the breakdown

Fig. 4.17. Plot of eqn. $R = K_1^{0\,2} t^q$ (—) and experimentally observed plume front

edge for laser-ablated Al-plume at a pressure of 1 mTorr in presence

of He, Ar, O_2 and air

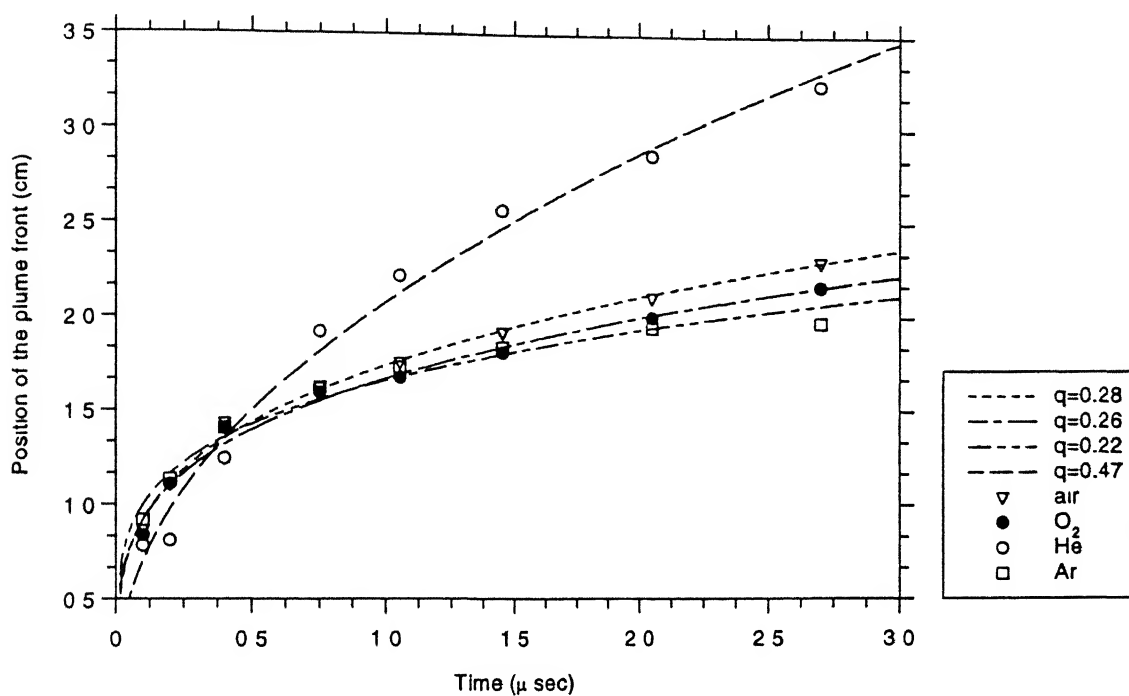To sum up, it follows that plume particles eventually diffuse into the compressed region, eqn. (2.23). The temperature of the shocked front is higher than the plasma vapor temperature for all times. Further, at and after stopping distance the gas particles diffuse into the compressed region. Thus inside the compressed region due to high temperature and presence of both the plasma and the gas particles there is a finite probability for the plasma particles to undergo physical and chemical changes.

An interesting feature observed in the ICCD images and the intensity profile of aluminum (fig. 4.18) is the splitting of the plume into two components. This is clearly evident in figures, where the intensity profiles show two peaks at earlier times which merges into one at later times. To understand this peculiar phenomenon we look into the fundamental processes involved in the production of plasma by laser ablation. For high laser flux density, the earlier part of the laser pulse removes a small amount of material from the surface that is further heated by absorption of the incoming laser radiation. It makes the material thermally ionized and opaque to the incident radiation. The absorbing plasma prevents the light from reaching the surface. Therefore, the material in front of the target surface absorbs most of the energy in the laser pulse. The surface is effectively cut off from the incoming radiation for a large fraction of the laser pulse. Near the end of the laser pulse the blow-off material becomes so hot that it begins to reradiate thermally. In addition, there may be ablation caused by the direct collisional interaction between the highly energetic plasma constituents and the material of the solid target. Some of this radiation may reach the target surface causing further vaporization. Double vaporization of the material from the target surface during a single laser pulse results in the stratification of the plasma as viewed by the ICCD. As the plume progresses (after stratification) in the direction away from the target, due to the difference in velocity of the components, the overall plume comprises of two bunches P_1 and P_2. The peak P_1 (fig. 4.19) starts to slow down due to the drag (viscous) force and eventually stops at a position where plasma pressure equals the ambient pressure. While peak P_2 which is not influenced by the drag keep moving towards the peak P_1. The slowing and moving of peaks can best be explained by measuring the velocities of the two peaks [232]. After a few hundred nano seconds peak P_2 merges with peak P_1. The stratification observed earlier [232] has been explained on the basis of measured velocity of P_1 and P_2 peaks. Due to the merger of P_1 and P_2 the intensity
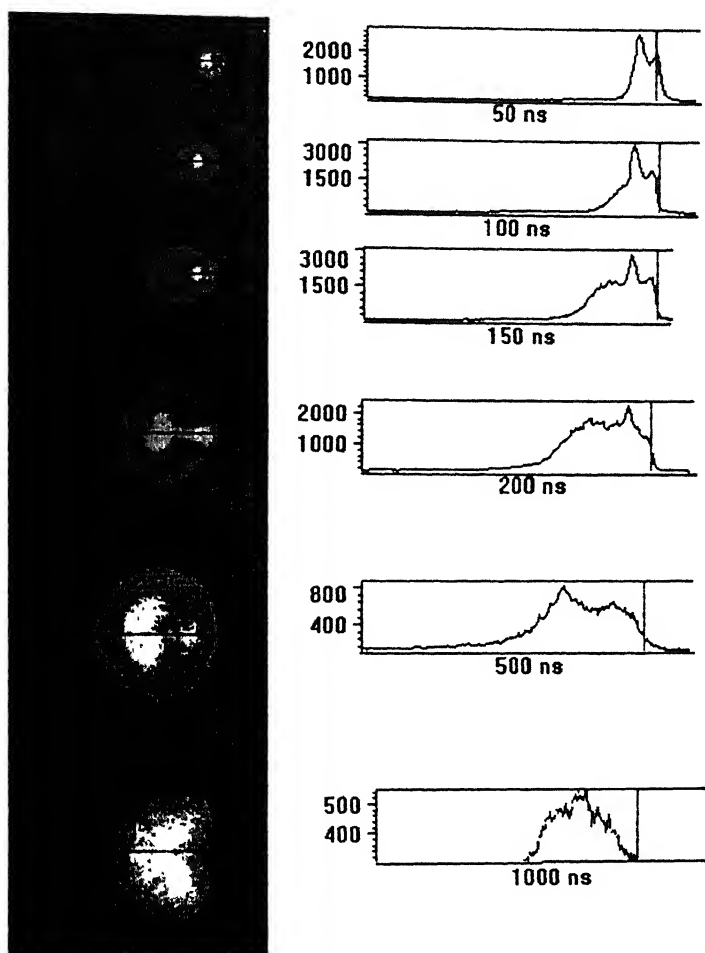
Fig. 4.18. Typical ICCD photograph of expanding aluminum plasma front at 1 mTorr of helium ambient pressure at various time delays. Intensity profiles of the images are also shown (right)

of the merged peak increases, implying the increase in pressure close to the compressed region. This results in diffusion of plasma particles into the compressed region.

Using ICCD to Estimate Particle Size in the Plume

The collision of the plasma species with that of ambient gas may result in the formation of clusters [246,247]. The size of the particles can be estimated from the calculated values of vapor temperature T_1, eqn. (2.36). To do so we assume our plasma to be an ensemble of small spherical particles radiating like a blackbody [115] at temperature T_1 which results in the cooling of the particles. For a particle of radius r at temperature T_1, the internal energy of the particle will be $\frac{4}{3}\pi r^3 \rho_d T_1 C_v$, where C_v is the molar specific heat and ρ_d the molar density of the particle. The particle emits radiation in accordance with the Stefan-Boltzmann law. The radiation emitted (energy loss) per unit area of the particle is $P_r = e_m \sigma_s T_1^4$ where σ_s is the Stefan's constant, and e_m is emissivity (=1 for a perfect blackbody)

The cooling of particles by blackbody radiation results in the loss of internal energy given by

$$\frac{dE_{int}}{dt} = \frac{4}{3}\pi r^3 \rho_d C_v \frac{dT_1}{dt} = -e_m \sigma_s T_1^4 (4\pi r_p^2) \qquad (4.3)$$

or

$$r_p = \frac{3e_m \sigma_s T_1^2}{\rho_d C_v \frac{dT_1}{dt}} \qquad (4.4)$$

the value of dT_1/dt is determined from the slope of the T_1-t plot shown in figure 4.11, T_1 here is the vapor temperature at which the particle size is calculated. The size of the particle 'r_p' at pressures 10 mTorr, 100 mTorr, 10 Torr and 100 Torr is calculated to be 1.20, 1.02, 0.12 and 0.11 μm respectively. Thus increasing pressure of the ambient gas decreases the particle size. The particle size was calculated at 400 nsec after the laser pulse. The size of particles increases with temperature. The temperature with in the plume falls rapidly and hence the size of the particle decreases accordingly, figure 4.19. However, depending on the pressure of the ambient gas the temperature within the plume falls rapidly but at
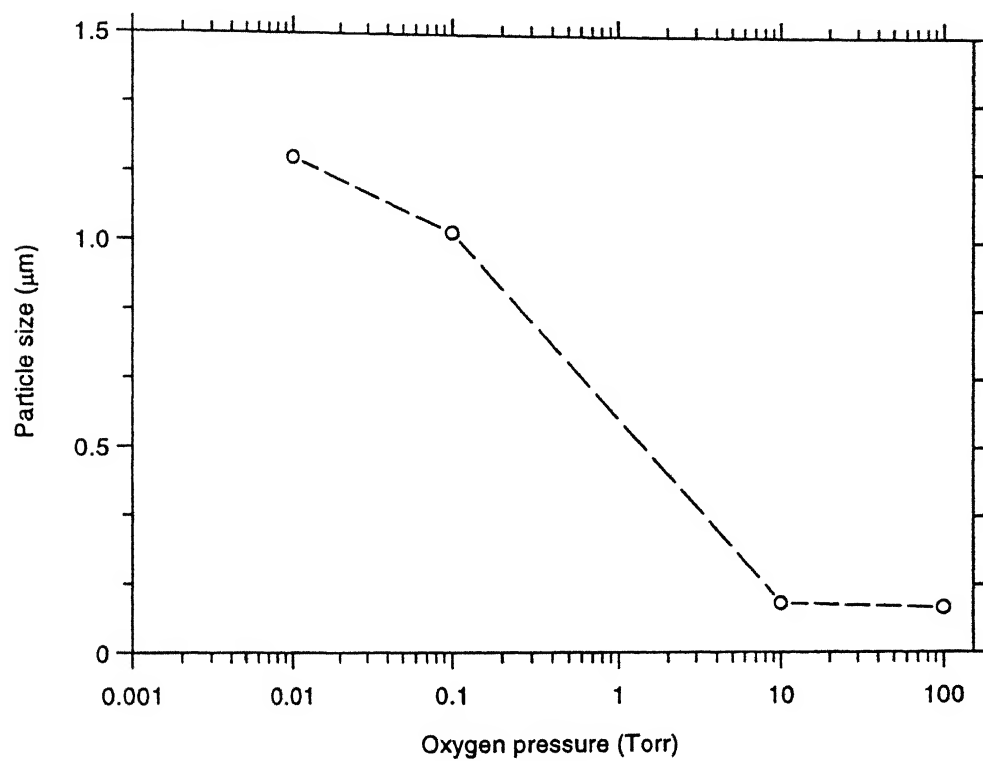
Fig. 4.19. Variation of size of particles (400 ns after the ablating pulse) with oxygen pressure at laser irradiance of 2.4 x 10^{10} W/cm^2

the plasma-gas interface it increases. Thus at a particular pressure strong mixing may occur at the interface and the conditions may be well suited for the formation of metal oxides or clusters

To conclude, the motion of laser-ablated plumes is simulated, which matches well with the ICCD images. The velocity of the expanding front is used to calculate various plasma parameters. An important parameter 'plume length' or 'stopping distance' is defined to optimize the target substrate distance. The particle size is estimated using ICCD. This can be a valuable technique for estimating the size of clusters. However, it will require a detailed information on emissivity at different temperature and wavelength.

Chapter V

LASER ABLATION DEPOSITION OF ALUMINUM OXIDE/NITRIDE FILMS

With the advent of the high power lasers both in the visible and in ultra violet regions laser ablation and deposition has become a topic of research for various applications [8,10,12,13]. The studies aim at the deposition of high quality thin films of wide range from superconductors, semiconductors to ferroelectrics, dielectrics and III-V nitrides. Deposition of Al_2O_3 thin films is of significant interest in microelectronic, optical and magnetic packaging application [188,248]. Whereas, AlN and their alloys are important because of high band gap, high refractive index, high thermal conductivity and doping capabilities [177,249]. There is currently an immense interest in the search for new non-linear optical materials for the fabrication of non-linear waveguides for potential applications in high speed electro-optic devices as well as for the generation of blue-green laser [250]. Most of the current research in inorganic materials focuses on $LiNbO_3$, $LiTaO_3$, and KDP waveguides. However, the fabrication of these waveguides requires the use of expensive single crystals. Hence, the commercial viability of these non-linear waveguides remains unclear. Since high optical quality films can be obtained using vapor deposition techniques, aluminum and gallium nitride films are of considerable interest [251]. Additionally, these metal nitrides have large band-gap energies and therefore are suited for short wavelength applications [197]. Almost all the growth processes require high substrate temperature [191,196,198,252] that plays a vital role both in deposition and in the quality of the nitride films. Oxygen impurities degrade the quality of the nitride film and influence the electrical and optical properties of the semiconductor [196]. Thus, the need for oxygen free nitride film is an essential part of development for the best quality films. The surface of AlN thin film is chemically very stable and cannot react with oxygen below 850 °C, whereas the surfaces of AlN powder are sensitive to moisture and atmospheric oxygen only above 100 °C. Thus the need for the growth of films at lower substrate temperature cannot be underestimated. On the contrary, it has been shown that the excess oxygen is necessary

for good quality high T_c superconducting films, which can be introduced during the plume evolution in oxygen ambient. It has been shown in Chapter IV through the plume dynamics of the laser-ablated plasmas in oxygen atmosphere that a strong chemical reaction at the boundary of the plume can occur [85, 136, 143, 176]. This also indicates that for films to be oxygen rich, the relative position of the substrate to that of target surface is important, which in turn depends on plume size. Thus to optimize the deposition process and the quality of the films, a detailed study of the in vivo plume characteristics is necessary. The best deposition conditions will depend on laser energy, target substrate distance, velocity distribution of ablated species, plume composition, background gas and interaction with the environment. In the present work we have used imaging as a tool to optimize the laser-ablated plume parameters with respect to laser parameters for the growth of metal oxide/nitride films at room temperature. The correlation of characteristics of the deposited film with that of the plasma is discussed. The results on the characterization of pulsed laser deposited thin aluminum films in oxygen/nitrogen background are presented.

EXPERIMENTAL SET UP

The experimental set-up used for the thin aluminum film deposition is shown in figure 3.24. The ablated aluminum in oxygen ambient was deposited on silicon (010) substrates placed at distances of 1.0, 2.0, and 3.0 cm from the target surface, whereas, for nitrogen background the films were deposited at the position where the breakdown of the nitrogen gas occurred. The position of breakdown and plume length and hence of the substrate was located using ICCD images. Substrate of sizes 1 cm x 1cm were cut from a highly polished silicon wafer. Substrates were cleaned using high purity acetone, trichloroethylene and ethyl alcohol to de-grease the surface using ultrasonic cleaner. The ambient pressure of N_2 and O_2 were kept at 100 mTorr and 100 Torr respectively during the deposition and the substrate was kept at room temperature. The laser irradiance used was 2.35×10^{10} W/cm^2 and 2.12×10^{11} W/cm^2 for films with oxygen and nitrogen ambient, respectively. The deposition time for oxide films was kept 10 min, whereas, for nitride it was 30 minutes.

RESULTS AND DISCUSSION

Various techniques used for characterization of the deposited films are listed in Chapter I. We have used SEM, XRD, micro-Raman and RBS to characterize the deposited films.

Aluminum films in oxygen background

It has been shown in Chapter IV that the temperature of the shocked region is always greater than the plume temperature. At a distance "plume length" or "stopping distance" the plasma pressure is equal to the background pressure. At this interface, with plasma on one side and ambient gas on the other, the probability of diffusion of the ambient gas into the plume is very large. Thus, due to high temperature of the shocked region and diffusion at the plasma-ambient gas interface, the metal plasma fuses with the ambient gas to form metallic oxides. In order to confirm the occurrence of chemical reaction, we deposited the aluminum films in oxygen background at a pressure of 100 mTorr. Plume length was estimated as discussed in Chapter IV. We maintained the target-substrate distance at plume length, greater than plume length and less than plume length. Films were deposited at all the three distances for same duration and irradiances. Films characterized using SEM, RBS, XRD and micro-Raman indicated the formation of aluminum oxide in the films. Although the films deposited near to the target (at a distance less than plume length) were found to be more denser than the films deposited at other distances. RBS of the films showed the correct stoichiometry for the film deposited at plume length. The micro-Raman studies showed that the intensity of the Si peak is maximum for film at greater distance followed by the film at plume length followed by the film grown at a distance less than the plume. It implies that the thickness of the film is greater near to the target followed by the film at the plume length and is least for the film deposited at a distance greater than plume length.

Scanning Electron Microscopy (SEM)

Scanning electron microscopy (SEM) was used to investigate the surface morphology and nucleation density of the deposited films.

Figure 5.1, shows SEM images of the aluminum films deposited on silicon substrates using 2.35×10^{10} W/cm^2 laser irradiance of 1.064 μm radiation. The films deposited at a distance less than the plume length are denser compared to the films deposited at distances at and greater than plume length. The plume length was 2.0 cm as observed using ICCD images. Higher magnification (x 10,000) showed that the single particle at plume length is larger than the particles at other two positions of the substrate. Further, the films deposited at plume length show a kind of aggregation of particles due to reaction of particles with oxygen. The EDS of the films confirm the stiochiometry of aluminum oxide (Al:O::2:3) at plume length.

Micro-Raman Scattering Measurements

To correlate the properties of the film with that of the characteristics of the plume at the edges, we undertook an extensive study of the spatial variation of the Raman spectra of the deposited films. The micro Raman spectra were recorded at five spots on each of the three deposited films. Figure 5.2 shows pictorially the boundary of an expanding plume and the position of the substrate w r t the target for the three films f_1, f_2 and f_3. For clarity the deposited film is shown as a block and the five spots, f_{11}, f_{12}, f_{13}, f_{14}, f_{15} on film f_1; f_{21}, f_{22}, f_{23}, f_{24}, f_{25} on film f_2 and f_{31}, f_{32}, f_{33}, f_{34}, f_{35} on film f_3 where Raman probe was focussed and spectra observed are shown enlarged. To examine structure and composition of deposited films an extensive study of c-Si band and isolated typical Al$_2$O$_3$ bands was carried out. It is observed that each of the deposited films exhibits inhomogenity over its cross-section. Figure 5.3 shows a typical micro-Raman spectra (spot size of ~ 1 μm) of the three films at f_{11}, f_{21} and f_{31}, depicting the two bands on the films. The Raman spectrum of bulk Al$_2$O$_3$ is also given for comparison. The positions of the observed Raman bands are given in Table 5.1 along with their assignments. The Raman data [253] for single crystal is also given in Table 5.1 for comparison. The other prominent Raman bands appearing in the spectra of the film, bulk and single crystals are at 491 and 594 cm^{-1}. These bands have been identified as the IR active (for D$_{3d}$ space group of the corundum). They appear to be strong in the Raman spectra due to distortion of the micro-crystal structure in the film.
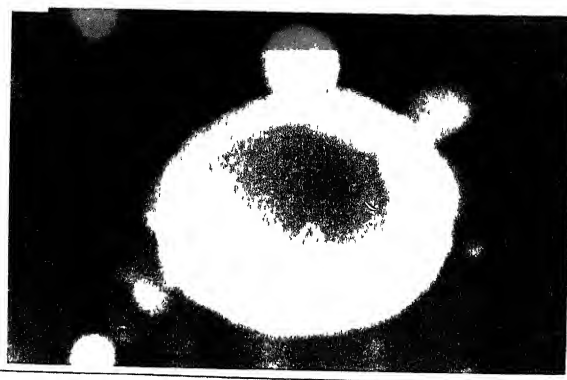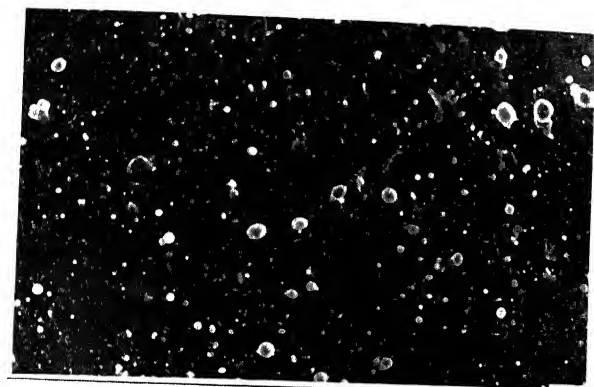
d = 1.0 cm
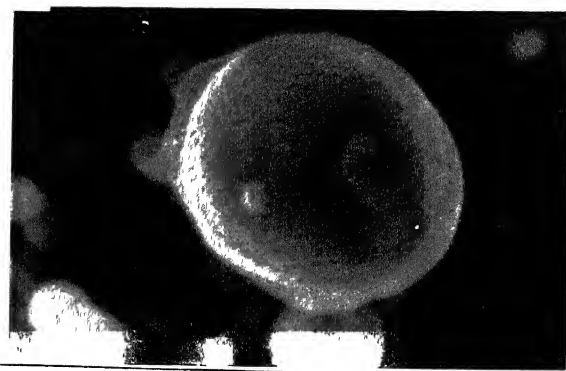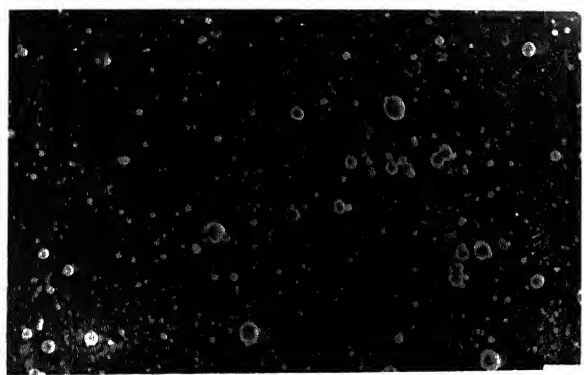
d = 2.0 cm
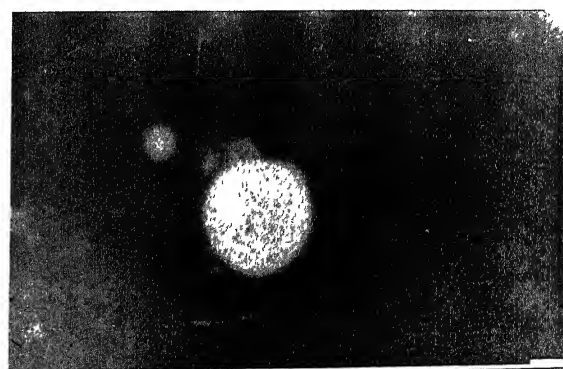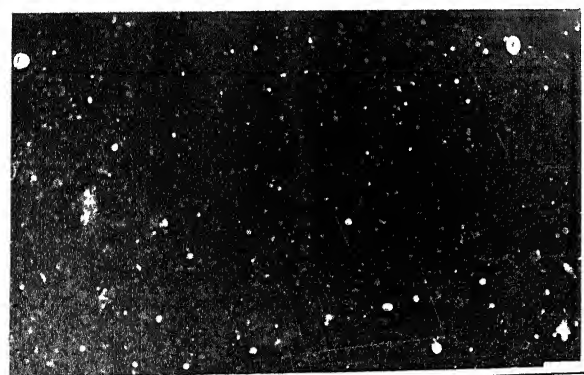
d = 3.0 cm

Fig. 5.1. Typical SEM photographs of laser ablation deposited aluminum films
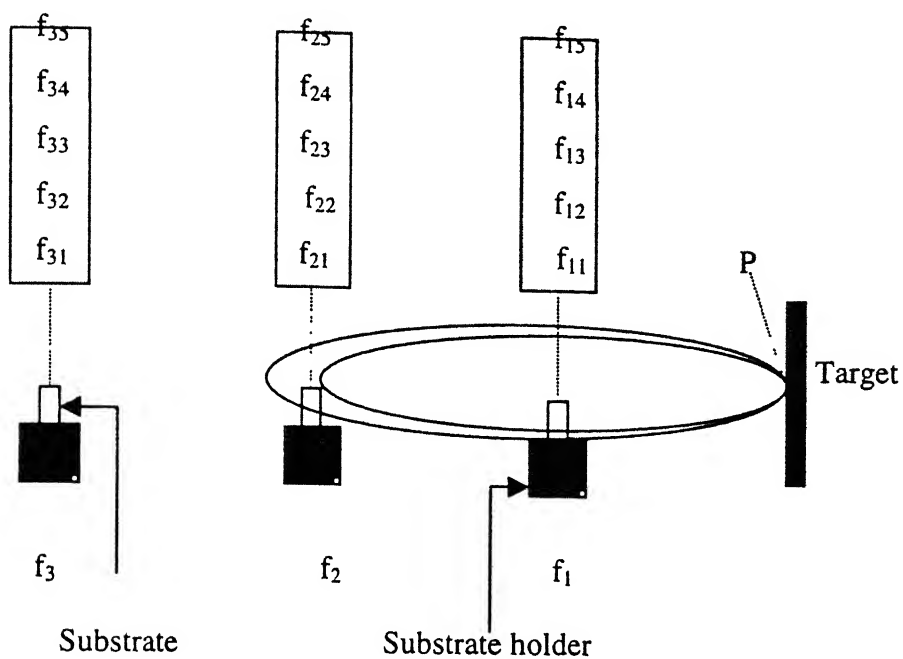in oxygen ambient at 1.0, 2.0 and 3.0 cms from the target surface

Fig. 5.2. Schematic of the positions of the films and the spots,
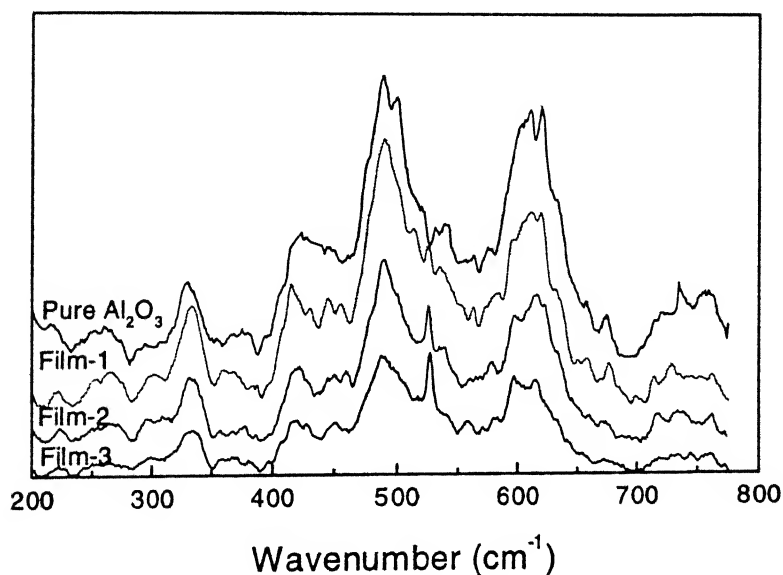where micro-Raman was taken

Fig. 5.3. Micro-Raman spectra of bulk Al_2O_3 and that of the films 1 mm
above the substrate holder (f_{11}). The substrate was placed at 1, 2, 3
cm respectively from the target surface

Table 5.1.

Observed frequency difference Δv (cm^{-1}), FWHM $\Delta v_{1/2}$ (cm^{-1}), and integrated intensity I (arb. units), of the Raman lines in aluminum oxide films at f_{11}, f_{21}, and f_{31} spots, pure bulk sample and single crystal of corundum; with their assignments

Film 1 (f_{11})	Film 2 (f_{21})	Film 3 (f_{31})	Bulk	Single Crystal	Assignment
Δv ($\Delta v_{1/2}$, I)	Δv ($\Delta v_{1/2}$, I)	Δv ($\Delta v_{1/2}$, I)	Δv ($\Delta v_{1/2}$, I)	Δv ($\Delta v_{1/2}$, I)	
372 (8, 0.8e4)	332 (41, 3.27e5)	373 (58, 6.75e4)	---	378	E_g (external)
418 (20, 1.81e5)	420 (23, 2.70e5)	422 (26, 1.35e5)	419 (21, 1.45e5)	418	A_{1g} (internal)
441 (40, 2.77e5)			431 (24, 7.41e4)	432	E_g (external)
448 (22, 4.51e5)	446 (13, 4.47e4)	450 (18, 4.77e4)	445 (14, 7.54e4)	451	E_g (external)
491 (41, 8.48e5)	491 (49, 1.4e6)	491 (36, 5.73e5)	492 (49, 1.39e6)	491 (502)[*]	(IR)
524 (8, 4.55e4)	526 (5, 5.57e4)	524 (5, 9.58e4)			c-Si (521 cm^{-1})
591 (28, 1.98e5)	559 (99, 4.2e5)	576 (86, 4.28e5)		578	E_g (internal)
608 (56, 1.51e6)	605 (47, 1.21e6)	612 (51, 5.86e5)	600 (48, 3.96e4)	594 (605)[*]	(IR)
674 (20, 3.66e4)	625 (21, 6.96e4)	648 (41, 9.27e4)		648	A_{1g} (internal)
746 (47, 1.37e5)	745 (51, 1.22e5)	745 (58, 1.12e5)	748 (49, 2.64e5)	755	E_g (external)

[*]observed in infra red spectra

here 1.37e5 means 1.37 x 10^5

(a) The silicon band

The laser deposited films are inherently non-uniform in thickness and hence the band of c-Si (521 cm^{-1}) are observed to be of varying position, width and intensity in all the films. In our analysis this band act as a probe for the thickness of the Al_2O_3 film and the interfacial stress exhibited by the deposited film. Figure 5.4 shows the variation of intensity of the c-Si band at 521 cm^{-1} of film 1 at spots f_{11}, f_{12}, f_{13}, f_{14} & f_{15}. The relative intensity of this band is minimum at the spot f_{11} and increases as one approaches the center of the plume. This implies that the maximum deposition occurs at a spot on its edge. Referring to figure 5.2 it is seen that the optimum deposition on film 1 occurs at the plume-gas interface. The minimum intensity of the Si band correspond to the possibility of maximum deposition of ablated material.

In order to compare the quality of the deposited films at the three position, we consider the frequency shift and intensity of Si band at 521 cm^{-1} at spots f_{11}, f_{21}, f_{31}. Figure 5.5 shows the variation of intensity and frequency shift of Raman band due to c-Si. The large frequeny shift implies high deposition. The smallest intensity correspond to large thickness of the deposited film on the substrate. It follows from figure 5.5 that the substrate at a distance of 3 cm from the target has the least deposition. The frequency shift exhibit maximum stress at f_{21} position, near the shock region, figure 5.2. This observation supports our earlier work [85,136,143,176] that a strong mixing (deposition) occurs at the shock front (extremities of the plume).

(a) The bands associated with Al_2O_3

Figure 5.6 shows the spatial variation of intensity of the isolated prominent E_g mode at 755 cm^{-1}, for film 1 and 2. It is observed that the intensity of thin Al_2O_3 Raman active mode increases for film 2 as we move from spot f_{21} to f_{25}. For film 1 the corresponding intensity decreases on moving from f_{11} to f_{15}. This observation agrees with the optimum deposition near (in) the shock (ed) region. This observation corroborates the results that follow from Si-bands.

The intensity of the observed c-Al_2O_3 at 755 cm^{-1} at spot f_{14}, f_{24}, f_{34} (falling near the axis of the plume) show a marked difference in the film deposited at three positions of substrate. Intensity of the band for film 2 is observed to be greater as compared to other
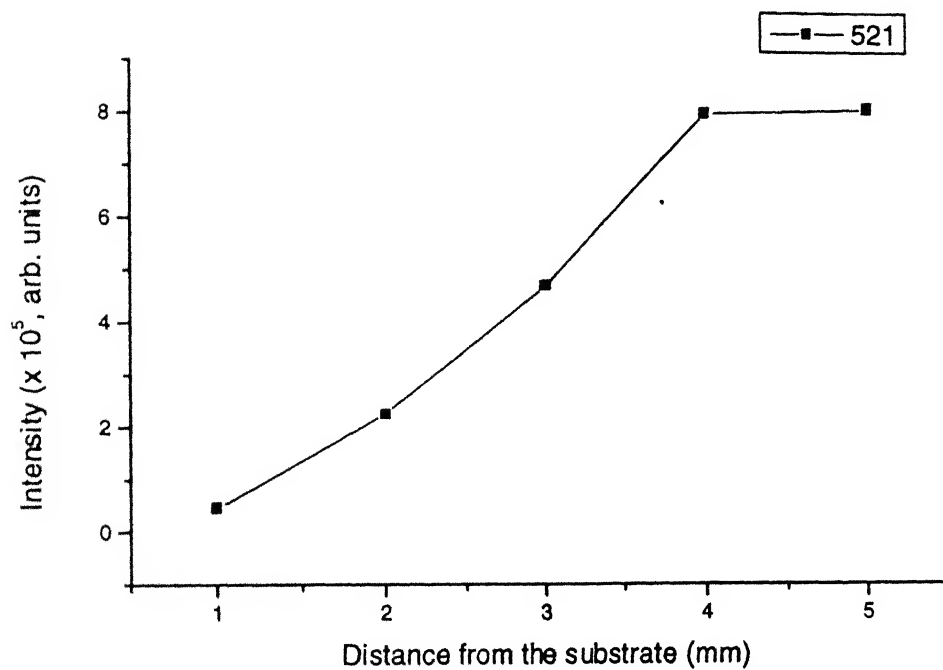
Fig. 5.4. Variation of intensity of Raman of c-Si at 521 cm^{-1} band at spot

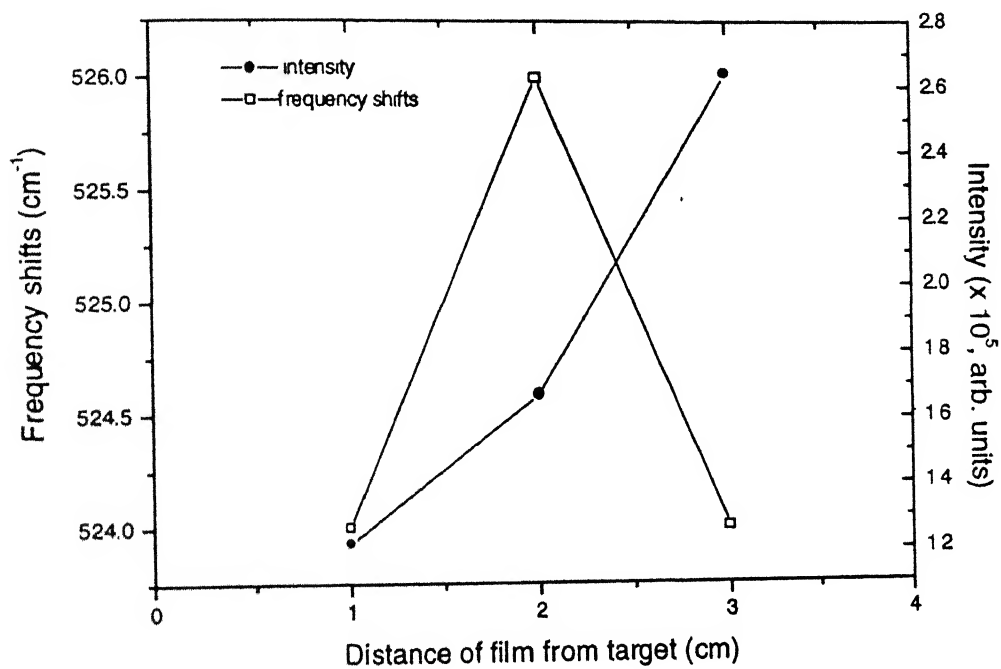f_{11}, f_{12}, f_{13}, f_{14} and f_{15}

Fig. 5.5. Variation of intensity and frequency shift of the 521 cm^{-1}
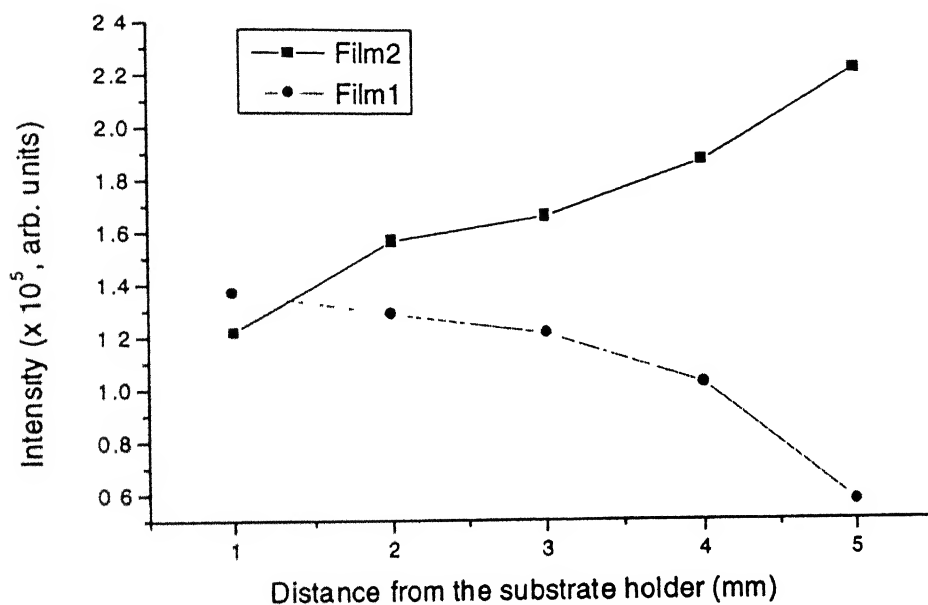band at spots f_{11}, f_{21} and f_{31}

Fig. 5.6. Variation of intensity of E_g mode of Al_2O_3 (755 cm^{-1} band) at spots f_{mn} (m, n: m = 1,2 & n = 1,2,3,4,5) normal to the plume axis for film 1 and film 2

films. Figure 5.7 gives the intensity and half width of the band at f_{14}, f_{24}, f_{34} spots. Half width is observed to be minimum for film 2 as compared to film 1 and 3. This shows that film 2 is more crystalline in character as compared to other films.

Rutherford Backscattering Spectrometry (RBS)

Rutherford Backscattering Spectrometry is a well-established method for determining the composition at the interface of two layers, identifying the mass of the impurity and the host atoms and thickness of the film etc.. We have used 1.23 MeV He$^+$ beam obtained from the 2 MeV Van de Graaf accelerator for the RBS analysis. Experiments were performed in a vacuum at 1.5 x 10^{-6} Torr. Figure 5.8 (a), (b) & (c), shows a typical RBS spectrum of the film deposited at 1.0, 2.0 and 3.0 cm. The deposited oxide films were of thickness 350, 240 and 140 nm respectively. The corresponding deposition/growth rate is 11.6, 8.0 and 4.7 nm/min. The chemical composition of the film deposited at 2.0 cm showed the composition of Al:O to be 2:3, while the film deposited at 1.0 and 3.0 cm showed no such compositional changes. The chemical composition of the film is in the ratio of (Al:O) 1:1.33, 2:3 and 1.2:3 respectively. The film deposited at all the three distances showed the formation of SiO$_2$ layer at the interface of the Si and Al. This layer is formed most probably due to oxidation of Si substrate in oxygen ambient.

Aluminum films in nitrogen background

When a laser beam of laser intensity 1.65 x 10^{11} W/cm^2 was focussed on to a solid target, it resulted in a high density, high temperature and pressure plasma propagating in a direction perpendicular to the target surface. When such an expansion takes place in an ambient atmosphere, a shock wave is formed which propagates with the expanding plume. Hydrodynamic equations along with other models were used to estimate the temperature, pressure and density of the plasma and the shocked region as discussed in Chapter IV. This plasma alongwith the shock are imaged by an ICCD. The ICCD images of laser-ablated aluminum plasmas show a breakdown in the nitrogen ambient, when an aluminum target was ablated in an nitrogen ambient at a pressure of 100 Torr at laser irradiance of 1.65 x 10^{11} W/cm^2. The breakdown of the gas is attributed to the high shock temperature at the

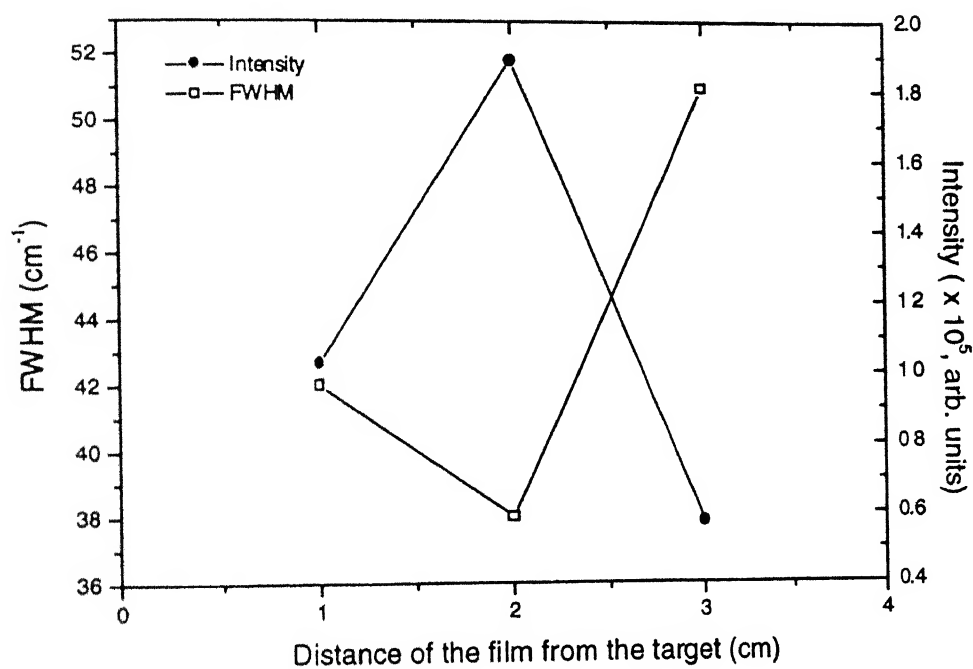Fig. 5.7. Comparison of intensity and half-width of 755 cm^{-1} band recorded at spots f_{14}, f_{24}, f_{34}
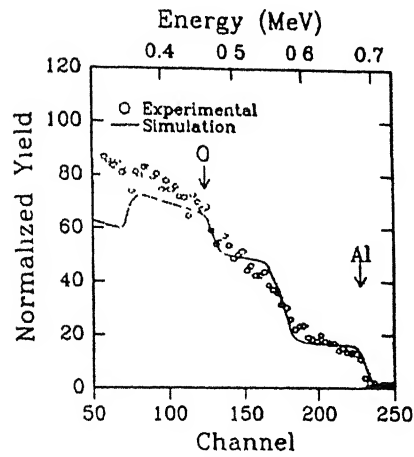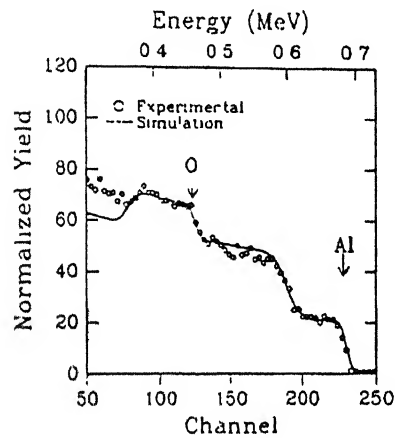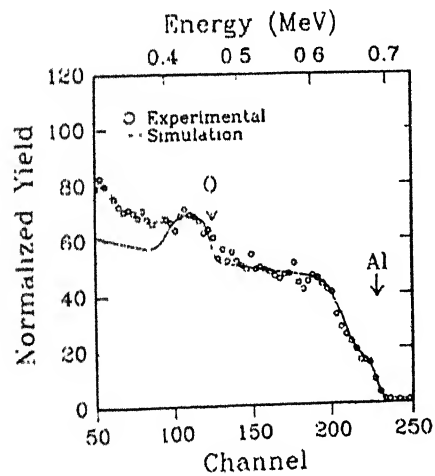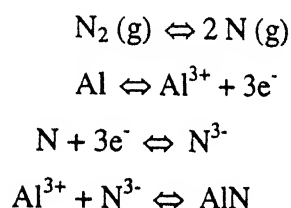
Fig. 5.8. RBS spectrum for the Al films deposited at 1.0, 2.0 and 3.0 cms in oxygen ambient at a pressure of 1 mTorr

edges of the Aluminum plasma. . The possibility of high energetic electrons from the target, ionizing the ambient gas cannot be ruled out [21]. However, it is very low at irradiance levels used in our experiments. No breakdown is observed for same energies and pressures lower than 10 Torr. To deposit a film, the substrate was placed at a position where the breakdown in nitrogen is observed (through ICCD images). Aluminum reacts with nitrogen atom to form AlN [255]. The kinetics of the chemical reaction which takes place in the vapor phase, can be written as [255,256],

$$N_2 \text{ (g)} \Leftrightarrow 2\,N\text{ (g)}$$

$$Al \Leftrightarrow Al^{3+} + 3e^-$$

$$N + 3e^- \Leftrightarrow N^{3-}$$

$$Al^{3+} + N^{3-} \Leftrightarrow AlN$$

The ICCD images were used to locate the exact position of breakdown. In order to deposit the nitride film we placed our substrate at a position where we observed (through ICCD images) the breakdown front in nitrogen. Films of aluminum ablated in nitrogen ambient in such a set up resulted in the formation of aluminum nitride films.

Scanning Electron Microscopy (SEM)

Aluminum films were deposited on a silicon substrate in nitrogen ambient at a pressure of 100 Torr with laser irradiance of 2.12×10^{11} W/cm^2. Figure 5.9 shows the SEM photograph of the films. The SEM analysis shows that the density of the films formed on the substrate is very high. At higher magnification, depending on the deposition time, particles were seen to be deposited one on the top of the other leading to the formation of multi-layers. The size of the particle is estimated approximately equal to 1.0 μm.

Micro-Raman Scattering Measurements

Figure 5.10 shows the Raman spectrum of a deposited films. The Raman peaks observed at 239, 252, 607, 610, 614, 667 and 673 cm^{-1} match well with that available in the
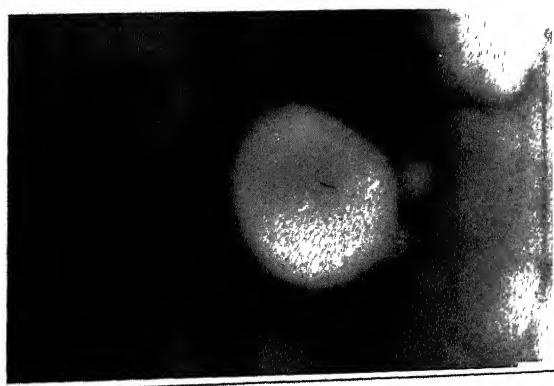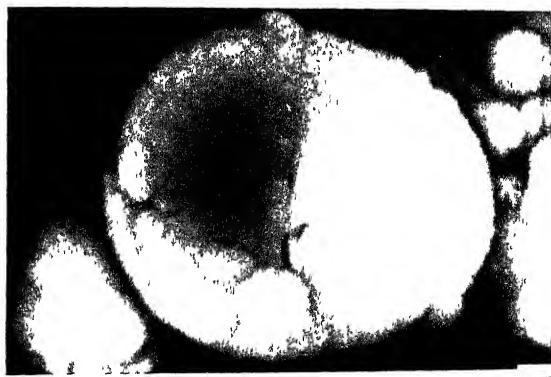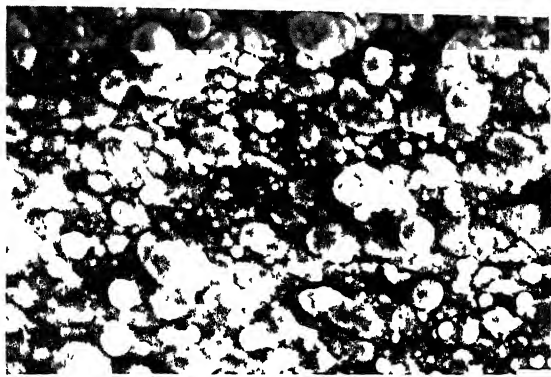
Fig. 5.9. SEM photographs of the AlN films deposited at room temperature. The magnification in (b) & (c) is higher than for (a)
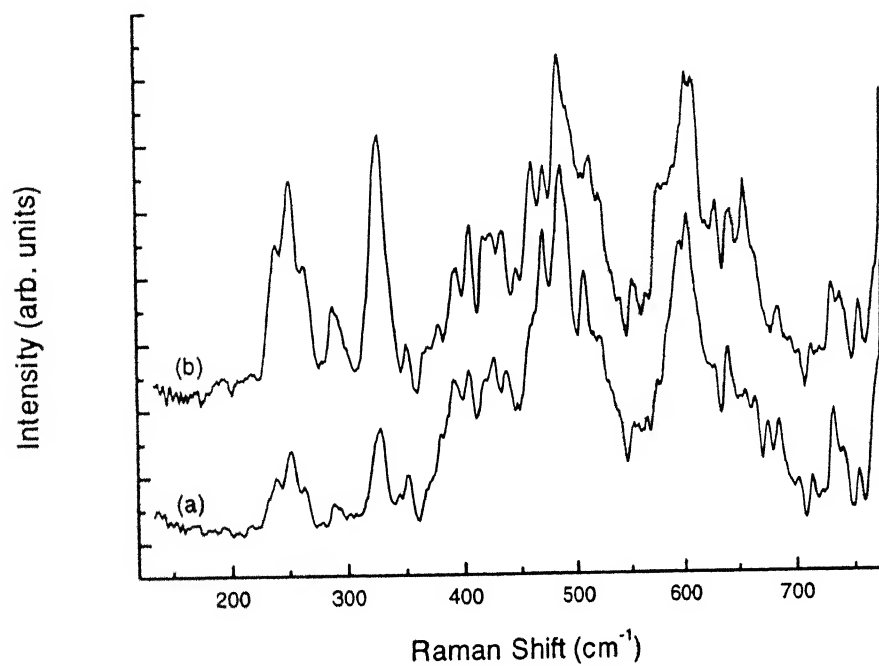
Fig. 5.10. Raman spectrum of the deposited film, (a) room temperature (b) annealed for one hour in flowing Nitrogen at a temperature of 750°C

literature [143,155,177]. The Raman spectrum was recorded with a resolution of 2 cm^{-1}. The Raman and XRD spectra indicate that the films are crystalline in nature. The films were annealed for one hour in flowing nitrogen at 750° C. The Raman spectrum of the annealed film showed a considerable increase in the intensity of the observed peaks. On annealing, two additional peaks at 611 and 656 cm^{-1} were also observed. There are six Raman active phonon modes viz., two E_2, and E_1 and one each of (TO), E_1 (LO), A_1 (TO), and A_1 (LO). All the observed peaks correspond to lattice phonon modes of AlN and are summarized in Table 5.2. The increase in intensity and the appearance of two peaks in the annealed films is attributed to impregnation of the flowing nitrogen at high temperatures.

X-ray Diffraction (XRD)

XRD of the films showed the formation of aluminum nitride. It is worthwhile to mention that films were also deposited at various other lower pressures (10 Torr, 100 mTorr, 10 mTorr), at various distances and laser energies. However, these films did not show the formation of AlN and were rich in Al. Figure 5.11 shows typical XRD spectrum of the deposited AlN film. The peaks are observed at 38.5°, 44.7°, 65.2°, 78.4°, 82.5°, and 116.7° which match well with that available in the literature [177,143].

To conclude, the deposition and characterization of the films using SEM, XRD, RBS and Raman spectroscopy suggest that the films deposited at the stopping distance are oxygen rich and are of good quality. However, the nitride films were deposited at room temperature at a position where the breakdown of the nitrogen gas takes place. The evaluation of deposition characteristics have potential for the growth of good quality metal-oxide, metal-nitride, ceramic and superconducting films.

Table 5.2.

The comparison of Raman shifts observed in our experiment (AlN) with that of already existing in the literature

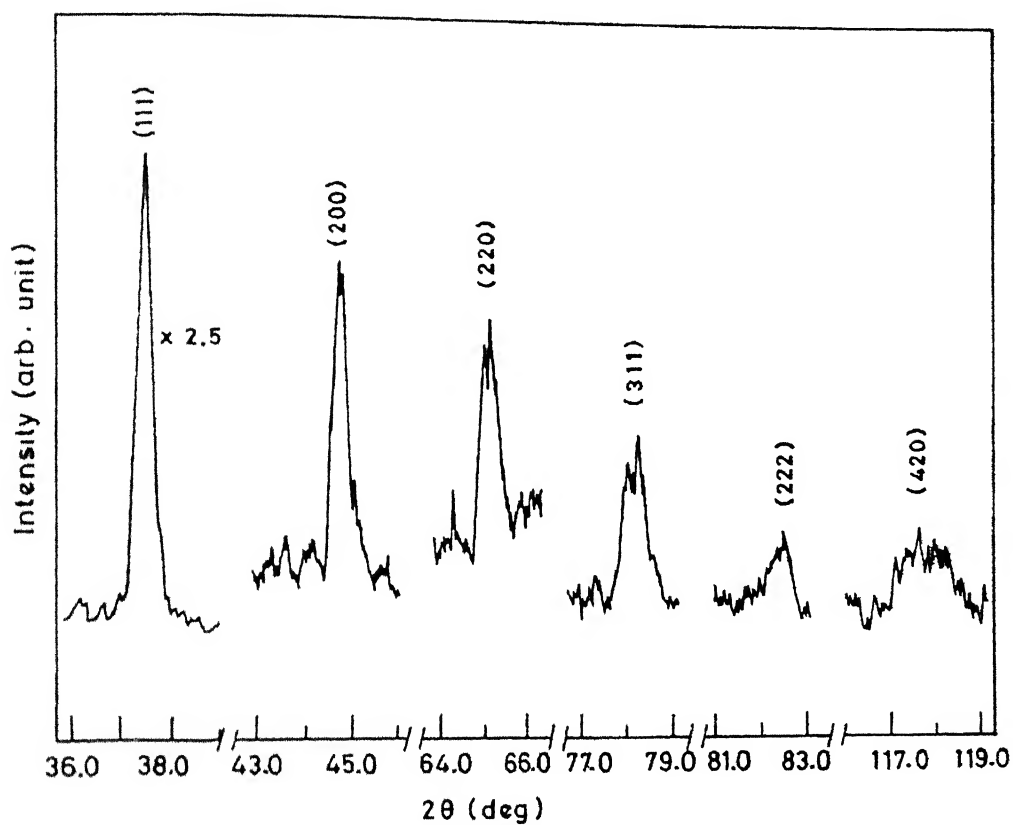| Phonon modes	Raman Shift (cm^{-1})		
	Crystalline [155,177]	Amorphous [155,177]	Observed
$E_2^{(1)}$	241, 252, 303		239, 252
$A_1(TO)$	607, 610, 614, 659, 660, 667	514	607, 610, 611, 614, 667
$E_2^{(2)}$	655, 665, 426, 660		656
$E_1(TO)$	614, 667, 671, 672, 673		673
$A_1(LO)$	663, 888, 893, 910	650, 746	
$E_1(LO)$	821, 895, 910, 916, 924	788, 825	

Fig. 5.11. XRD spectrum of an AlN film deposited at room temperature

Chapter VI

CONCLUSION

The thesis reports studies on the laser-ablated aluminum plumes in vacuum and ambient atmosphere (He, Ar, N_2, O_2 and Air) at various ambient pressures (> 0.1 mTorr - 100 Torr) at moderate laser irradiances (10^{11} - 10^{12} W cm^{-2}) used for deposition of thin metal oxide and metal nitride films. The diagnostic techniques like, fast photography, Faraday cup, emission spectroscopy and time of flight mass spectrometer were developed to investigate the evolution dynamics of the plume. A Q-switched Nd:YAG laser ($\lambda = 1.064$ μm) was used to generate the aluminum plume. Two-dimensional view of the plume expansion at various time delays with respect to the ablating pulse was made by recording the overall visible emission from the plasma plume with a gated ICCD camera system (ICCD 176G/2, Princeton Instrument Inc.). The plasma (pressure, temperature, velocity, density) and shock (temperature, velocity, density) parameters of an expanding front were estimated and compared with theoretical values obtained through hydrodynamical analysis of the plume. Optical emission spectroscopy was used to estimate density and temperature of the aluminum plumes used for film deposition as a function of distance from the target surface and laser energy. Using Faraday cup, kinetic energy and ionic yield of the ablating plasma were estimated at various distances from the target surface at an angle of 45 ° with respect to the target surface normal and at a pressure less than 0.1 mTorr. The kinetic energy and ionic yield of the ions were seen to increase with the increase in laser fluence. Time of flight mass spectrometer was used to estimate the ionization threshold of aluminum in vacuum. Plume and the target-substrate distance is optimized for deposition of aluminum films in oxygen and nitrogen. SEM, XRD, micro-Raman spectroscopy and RBS were employed to characterize the deposited films.

Evolution and dynamics of the laser-ablated plasmas is studied using ICCD images and recorded at various time delays with respect to the ablating pulse in various ambient atmospheres at various ambient pressures and laser energies. The isothermal and adiabatic equations of motion for laser produced plasmas were simulated to understand the dynamics

of plasma. It is observed that the simulated laser-ablated plume match well with the recorded images of the plume. It is shown that the plasma elongates more along the target normal as compared to transverse directions with increase in time. The velocity of the plume front is estimated from the displacement of the plume front with time. The maximum velocity corresponds to the velocity at minimum delay (29 ns, limitation of the experimental set up) with respect to the ablating pulse and was used to estimate the temperature at the surface of the target. The expansion of the plasma is observed to be more in case of lighter gas (He) as compared to heavier gases (Ar, O_2, N_2 and air). This is attributed to the difference in the degree of freedom per unit mass in different gases. The observed velocity of the expanding front is 7.29 x 10^6 cm/sec, 6.84 x 10^6 cm/sec, 6.75 x 10^6 cm/sec and 6.21 x 10^6 cm/sec for He, Air, O_2 and Ar respectively at 10^{-2} Torr. Various plasma parameters were evaluated using hydrodynamic equations. Vapor pressure and temperature of plasma decrease with increase in time and ambient pressure. Classical drag and blast models are used to study the dynamics of the plume in an ambient atmosphere. A plume propagating in an ambient atmosphere experiences a viscous force (drag force) proportional to its velocity which progressively slows down the plume, eventually bringing it to rest. The distance from the target at which the propagation ceases is termed as stopping distance or plume length. As the pressure of the ambient atmosphere increases, the stopping distance decreases and the intensity of the plume increases due to confinement and increased collisions of the plasma particles in a small volume. At plume length the plasma pressure equals the ambient gas pressure and hence the velocity of the ablated species is minimum at this point. The blast wave equation ($R = K_1 t^q$) is used to define the expansion of the shock front at various irradiances. The exponent q for our experimental conditions lies between 0.22 and 0.48 compared to 0.4 for an ideal shock. The discrepancy in the value of exponent may be due to the growth of instability at moderate laser intensities and low pressures.

The estimated plume length for aluminum plasma in oxygen ambient at a pressure of 100 mTorr is ~ 2.0 cm. The calculated temperature in the shocked region is 10^6 K at 29 ns after the ablating pulse in 100 mTorr of oxygen pressure compared to the vapor temperature of 10^5 K. Thus at the plume length, the gas particles diffuse into the shocked region from one side and the plasma species from the other. It is proposed that due to high

temperature in the shocked region a vigorous chemical reaction takes place at the interface resulting in the formation of aluminum oxide. Thus films deposited at the interface are expected to be oxygen rich. The result obtained is of immense importance for the growth of superconducting films.

In order to confirm the possibility of chemical reaction at the interface (shocked region), films of aluminum in oxygen background were deposited, keeping the substrate at a distance of 1.0, 2.0, and 3.0 cm. The plume length was located by imaging the expanding plasma and was 2.0 cm. SEM analysis showed the morphological structure of the deposited films. RBS of the deposited films showed that the film at plume length show a stoichiometric chemical composition (Al:O) as 2:3, whereas, for the films at 1.0 and 3.0 cm showed the chemical composition to be 1:1.33 and 1.2:3 respectively. This confirms the occurrence of chemical reaction at plume length. The estimated growth rate of the film at plume length is 8.0 nm/min. Micro-Raman studies of the film were carried out and the bands observed were compared with those obtained for a pure Al_2O_3 pellet and a Ruby crystal. The observation confirmed the formation of aluminum oxide in the films. Further investigations of the Raman bands of c-Si (521 cm^{-1}) and c-Al_2O_3 (755 cm^{-1}) justified the optimum target-substrate distance, for the deposition of oxygen rich films, of 2.0 cm in our case.

Breakdown of ambient gas (Ar, N_2 and O_2) was observed at higher laser irradiances on the target. The breakdown of the gas is attributed to the high shock temperature at the edges of the aluminum plasma. The deposition of aluminum nitride films by laser ablation deposition requires a high substrate temperature. Further, the presence of oxygen impurities influences the electrical and optical properties of the film. However, the films deposited at lower substrate temperature are free from oxygen impurities. Aluminum nitride films were deposited on silicon substrate at room temperature at 100 Torr of nitrogen gas and laser irradiance of 1.65×10^{11} W cm^{-2}. ICCD images are used to locate the breakdown front of nitrogen gas. A silicon substrate was placed at the breakdown front. Deposited films were characterized using SEM, XRD, RBS and micro-Raman. SEM analysis showed that the density of the films was high. XRD peaks of 38.5°, 44.7°, 65.2°, 78.4°, 82.5° and 116.7° match well with those of c-AlN available in the literature. Raman bands are observed at 239, 252, 607, 614, 667 and 673 cm^{-1} in the mciro-Raman spectra of the deposited film.

These bands agree with those of c-AlN in the literature. The AlN films were annealed in flowing nitrogen at 750 °C for one hour. The Raman spectra of the annealed films showed an enhancement in the observed Raman bands, which is attributed to impregnation of nitrogen at high temperature.

FUTURE SCOPE OF WORK

We have employed fast photography to study the evolution and dynamics of the laser-ablated aluminum plasmas. It would be of interest to record the overall images of expanding plasma using narrow band pass filters to understand the process of transport of ejected species to the substrate. It will also provide mechanism for various chemical reactions involved between ejected species and ambient gas at the edge of the plume. We have optimized target-substrate distance for aluminum oxide and aluminum nitride films using ICCD. The developed technique can be used for depositing other oxide films such as zinc oxide, which finds its use in second harmonic generation, transparent conducting films and fabrication of UV semiconductor laser etc.. Experimental parameters optimized using ICCD images can be used to simulate properties of the film.

ICCD camera system can be coupled with a monochromator to record the emission spectra of the expanding plume at various time delays. The analysis of the emission spectra in the shocked region may help to study the transient species during the chemical reaction-taking place at the plasma gas interface.

Time of flight mass spectrometer can be used to identify various ions and clusters. Its length can be increased so as to increase its resolution. The system can be modified for various experiments on Resonance Ionization Mass Spectrometer (RIMS). The principle involved in RIMS is the selective excitation of atoms or molecules with resonant laser light followed by ionization. The resulting photo-ions are extracted by an electric field and detected with suitable detectors. This technique can be used for estimating spectroscopic parameters e.g., excitation and ionization cross-section, isotope shifts, etc.. The system can also be used for trace element analysis.

Faraday cup has been used to study the behavior of electrons and ions in vacuum. The experiment can be repeated spatially, at various angles and in various ambient atmospheres to give an exact distribution of the charged species. A substrate can replace the

collector plate of the Faraday cup for depositing film. The plasma parameter, the ionic yield optimized at the charge collector may help to get a film of desired morphology and stoichiometry.

Oxide films find their use as insulators, antireflection coatings and protective films for mirrors, thin film capacitor, piezoelectric films, high T_c superconducting films etc.. In all the above applications the idea of depositing films at plume length may help in depositing thin oxide films of required stoichiometry by laser ablation deposition. Laser ablation deposition of high T_c superconducting targets results in films which are oxygen deficient and results in films of varying electrical and mechanical properties. Hence, one deposits the film in oxygen ambient to take care of oxygen deficiency in the film. The proposed technique of plume length may yield oxygen rich films of desired stoichiometry.

It will be of importance, to use other techniques of characterization such as Tunneling Electron Microscopy (TEM) and Atomic Force Microscopy (AFM) to study the surface morphology of the deposited films in order to determine their role for device applications. Further, characterizing the films for hardness, band gap, frictional coefficients etc., can provide a better understanding of the films for various technological applications. Specific applications of the deposited films require different substrate materials. The deposition can be tried on various substrates to study their possible role in thin film growth.

References

1. F. Breech, and L. Cross, Appl. Spectrosc. **16**, 59 (1962).

2. R. E. Honig, and J. R. Woolston, Appl. Phys. Lett. **2**, 138 (1963).

3. J. F. Ready, Appl. Phys. Lett. **3**, 11 (1963).

4. H. M. Smith, and A. F. Turner, Appl. Opt. **4**, 147 (1965).

5. J. T. Cheung and H. Sankur, CRC Crit. Rev. Solid State Mater. Sci. **15**, 63 (1988).

6. J. Berkowitz, and W. A. Chupka, J. Chem. Phys. **40**, 2735 (1964).

7. T. G. Dietz, M. A. Ducan, D. E. Powers, and R. E. Smalley, J. Chem. Phys. **74**, 6511 (1981).

8. J. C. Miller, and R. F. Haglund, Jr. (eds.), *Laser Ablation Mechanism and Applications,* (Springer, Berlin, 1991).

9. E. Fogarassy, and S. Lazare (eds.), *Laser Ablation of Electronic Materials*, (North-Holland, Amsterdam, 1992).

10. J. C. Miller, and D. B. Geohegan (eds.), *Laser Ablation: Mechanism and Applications-II*, (American Institute of Physics, New York, 1994)

11. R. Wagner, S. -Y. Chen, A. Maksimchuk, and D. Umstadter, Phys. Rev. Lett. **78**, 3125 (1997).

12. R. Singh, D. Norton, L. Laude, J. Narayan, and J. Cheung (eds.), *Advanced Laser Processing of Materials-Fundamentals and Applications,* (MRS, Pennsylvania, 1996).

13. I. A. Aksay, G. L. McVay, and D. R. Ulrich (eds.), *Processing Science of Advanced Ceramics,* (MRS, Pennsylvania, 1989).

14. I. W. Boyd, and J. I. B. Wilson, Nature **303**, 481 (1983).

15. I. Ursu, I. N.. Mihailescu, L. Nanu, A. M. Prokhorov, V. I. Konov, and V. G. Ralchenko, Appl. Phys. Lett. **46**, 110 (1985).

16. D. Henderson, J. C. White, H. G. Craighead, and I. Adesida, Appl. Phys. Lett. **46**, 900 (1985).

17. R. F. Davis, in *Processing Science of Advanced Ceramics,* (eds.) I. A. Aksay, G. L. McVay, and D. R. Ulrich, P. 213 (MRS, Pennsylvania, 1989).

18. R. K. Singh, O. W. Holland, and J. Narayan, J. Appl. Phys. **68**, 233 (1990).

19. R. K. Singh, and J. Narayan, Phys. Rev. B **41**, 8843 (1990).

20. M. Aden, E. Beyer, G. Herziger, and H. Kunze, J. Phys. D: Appl. Phys. **25**, 57 (1992).

21. L. J. Radziemski and D. A. Cremers (eds), Laser Induced Plasmas and Applications, (Marcel Dekker, Inc., New York, 1989).

22. R. K. Thareja, R. K. Dwivedi, and Abhilasha, Phys. Rev. B **55**, 2600 (1997).

23. R. K. Thareja and Abhilasha, Proc. XXI International Conf. Phen. Ion. Gases **Vol III**, 482 (1993).

24. Abhilasha, P. S. R. Prasad and R K Thareja, Phy. Rev. E **48**, 2929 (1993).

25. T. P. Hudges, *Plasmas and Laser Light* (Wiley, New York, 1975).

26. M. V. Allmen, and A. Blatter, in *Laser-Beams Interactions with Materials*, (Springer, New York, 1998).

27. R. E. Leuchtner, A. C. Harms and A. W. Castleman, Jr., J. Chem. Phys. **94**, 1093 (1991).

28. J. F. Ready, *Effects of High Power Laser Radiation*, (Academic, New York, 1971)

29. K. Laqua, in *Analytical Laser Spectroscopy*, N. Omemetto (ed.), (Wiley, Interscience, New York, 1979).

30. R. F. Wood, and G. E. Giles, Phys. Rev. **B 23**, 2923 (1981).

31. N. G. Basov, V. A. Boiko, V. A. Gribbov, S. M. Zakharov, D. N. Krokhin, and G. V. Shlizkov, Sov. Phys. JETP **34**, 81 (1972).

32. Y. A. Bykovskii, N. N. Degtyarenko, V. F. Elesin, Y. P. Kozyrev, and S. M. Sil'nov, Sov. Phys. JETP **33**, 706 (1971).

33. V Kumar, and R K Thareja, J. Appl Phy. **67**, 3260 (1990).

34. R. Tambay, R. Singh, and R. K. Thareja, J. Appl. Phys. **72**, 1197 (1992).

35. M. Aden, E. Beyer, G. Herziger, and H. Kunze, J. Phys. D: Appl. Phys. **25**, 57 (1992).

36. A Neogi, and R K Thareja, Pramana -J. Phys. **50**, 63 (1998).

37. E. Sutcliffe, and R. Srinivasan, J. Appl. Phys. **60**, 3315 (1986).

38. R. Srinivasan, B. Braren, and R. W. Dreyfus, J. Appl. Phys. **61**, 372 (1987).

39. S. Küper, and M. Stuke, Appl. Phys. Lett. **54**, 4 (1989).

40. B. J. Garrison, and R. Srinivasan, J. Appl. Phys. **57**, 2909 (1985).

41. R. Srinivasan, and V. Mayne-Banton, Appl. Phys. Lett. **41**, 576 (1982).

42. B. Danielzik, N. Fabricius, M. Röwekamp, and D. Von der Linde, Appl. Phys. Lett. **48**, 212 (1986).

43. G. Koren, and J. T. C. Yeh, Appl. Phys. Lett. **44**, 1112 (1984).

44. J. H. Brannon, J. R. Lankard, A. I. Baise, F. Burns, and J. Kaufman, J. Appl. Phys. **58**, 2036 (1985).

45. G. Gorodetsky, T. G. Kazyaka, R. L. Melcher and R. Srinivasan, Appl. Phys. Lett. **46**, 828 (1985).

46. T. Shino, K. Setsune, O. Yamazaki, and K. Wasa, Appl. Opt. **26**, 587 (1987).

47. R. K. Thareja, and Abhilasha, J. Chem. Phy. **100**, 4019 (1994).

48. J. N. Broughton and R. Fedosejevs, J. Appl. Phys. **74**, 3712 (1993).

49. R. Tambay, and R. K. Thareja, Pramana-J. Phys. **41**, 257 (1993).

50. B. Bescós, and A. G. Ureña, J. Laser Appls. **7**, 47 (1995).

51. R. Timm, P. R. Willmott, and J. R. Huber, J. Appl. Phys. **80**, 1794 (1996).

52. K. Mann, and K. Rohr, Laser and Particle Beams **10**, 435 (1992).

53. J. C. S. Kools, and J. Dieleman, J. Appl. Phys. **74**, 4163 (1993).

54. H. F. Sakeek, T. Morrow, W. G. Graham, and D. G. Walmsley, J. Appl. Phys. **75**, 1138 (1994).

55. C. Cali, F. La Rosa, G. Targia, and D. Robba, J. Appl. Phys. **78**, 6265 (1995).

56. A. H. El-Astal, and T. Morrow, J. Appl. Phys. **80**, 1156 (1996).

57. N. H. Cheung, Q. Y. Ying, J. P. Zheng, and H. S. Kwok, J. Appl. Phys. **69**, 6349 (1991).

58. I. Olivares and H. J. Kunze, Phys. Rev. E **47**, 2006 (1993).

59. F. Fuso, L. N. Vyacheslavov, G. Masciarelli, and E. Arimondo, J. Appl. Phys. **76**, 8088 (1994).

60. R. A. Al-Wazzan, C. L. S. Lewis, and T. Morrow, Rev. Sci. Instrum. **67**, 85 (1996).

61. J. Grun, J. Stamper, C. Manka, J. Resnick, R. Burris, J. Crawford, and B. H. Ripin, Phys. Rev. Lett. **66**, 2738 (1991).

62. R. G. Tuckfield, and F. Schwirzke, Plasma Phys. **11**, 11 (1969).

63. G. Dimonte, and L. G. Wiley, Phys. Rev. Lett. **67**, 1755 (1991).

64. A. Neogi, and R. K. Thareja, J. Appl. Phys. **85**, (1999) 1131

65. L. Dirnberger, P. E. Dyer, S. R. Farrar, and P. H. Key, in *AIP Conference Proceedings* 288, edited J. C. Miller and D. B. Geohegan (AIP, New York, 1994) pp 349.

66. B. Soom, H. Chen, Y. Fisher, and D. D. Meyerhofer, J. Appl. Phys. **74**, 5372 (1993).

67. G. Mehlman, D. B. Chrisey, P. G. Burkhalter, J. S. Horwitz, and D. A. Newman, J. Appl. Phys. **74**, 53 (1993).

68. N. G. Utterback, S. P. Tang and J. F. Friichtenicht, Phys. Fluids **19**, 900 (1976).

69. B. C. Boland, F. E. Irons and R. W. P. McWhirter, J. Phys. **B 1**, 1180 (1968).

70. F. E. Irons, R. W. P. McWhirter and N. J. Peacock, J. Phys. B: Atom. Molec. Phys. **5**, 1975 (1972).

71. C. Steden, and H. -J. Kunze, Phys. Lett. **A 151**, 534 (1990).

72. R. Tambay, and R. K. Thareja, IEEE J. Quant. Electron. **31**, 743 (1995).

73. F. E. Irons, and N. J. Peacock, J. Phys. **B 7**, 2084 (1974).

74. P. E. Dyer, P. H. Key, D. Sands, H. V. Snelling, and F. X. Wagner, Appl. Surf. Sci. **86**, 18 (1995).

75. L. Z. Barabash, Yu. A. Bykovskii, A. A. Golubev, D. G. Kosyrev, K. I. Krechet, Yu. I. Lapitskii, S. V. Latyshev, R. T. Haydarov, B. U. Sharkov and A. V. Shumshirov, Laser and Part. Beams **2**, 49 (1984).

76. R. H. Dixon, and R. C. Elton, Phys. Rev. Lett. **38**, 1072 (1977).

77. D. B. Geohegan, A. A. Puretzky, R. L. Hettich, X. -Y. Zheng, R. E. Haufter, and R. N. Compton, Trans. Mat. Res. Soc. Jpn. **17**, 349 (1994).

78. R. K. Thareja, Abhilasha, and R. K. Dwivedi, Inst. Phys. Conf.Ser.**140**, 435 (1995).

79. D. B. Geohegan, and A. A. Puretzsky, Mat. Res. Soc. Symp. Proc. **388**, 21 (1995).

80. J. Farny, S. Nagraba, and E. Woryna, J. Tech. Phys. **28**, 185 (1987).

81. R. R. Goforth, and D. W. Koopman, Phys. Fluids **17**, 698 (1974).

82. O. Yavas, E. L. Maddocks, M. R. Papantonakis, and R. F. Haglund, Appl. Phys. Lett. **71**, 1287 (1997).

83. T. Kerdja, S. Abdelli, D. Ghobrini, and S. Malek, J. Appl. Phys. **80**, 5365 (1996).

84. V. Yu. Baranov, O. N. Derkach, V. G. Grishina, M. F. Kanevskii, and A. Yu. Sebrant, Phys. Rev. **E 48**, 1324 (1993).

85. A. Misra, A. Mitra, and R. K. Thareja, Appl. Phys. Lett. **74**, 929 (1999).

86. A. Namiki, T. Kawai, and K. Ichige, Surf. Sci. **166**, 129 (1986).

87. J. R. Ho, C. P. Grigoropolous, and J. A. G. Humphrey, J. Appl. Phys. **79**, 7205 (1996).

88. R. F. Wood, J. N. Leboeuf, D. B. Geohegan, A. A. Puretzky, and K. R. Chen, Physical Review B **58**, 1533 (1998).

89. H. –U. Habermeier, *Laser Ablation of Electronic Materials,* (Eds.) E. Fogarassy and S. Lazzare, (Elsevier Science, New York, 1992).

90. R. Kelly, A. Miotello, B. Braren, A. Gupta, and K. Casey, Nucl. Inst. Meth. Phys. Res. B **65**, 187 (1992).

91. J. C. S. Kools, J. Appl. Phys. **74**, 6401 (1993).

92. O. B. Anan'in, Yu. A. Bykovskii, Yu. V. Eremin, E. L. Stupitskii, I. K. Novikov, and S. P. Frolov, Sov. J. Quant. Electron. **21**, 787 (1991).

93. J. J. McFarlane, G. A. Moses, and R. R. Peterson, Phys. Fluids **B 1**, 635 (1989).

94. K. L. Saenger, J. Appl. Phys. **66**, 9435 (1989).

95. R. K. Thareja, A. Misra and S. R. Franklin, Spect. Acta B **53**, 1919 (1999).

96. R. A. Lindley, R. M. Gilgenbach, C. H. Chung, J. S. Lash and G. L. Doll, J. Appl. Phys. **76**, 5457 (1996).

97. M. Aden, E. Beyer, and G. Herziger, J. Phys. D: Appl. Phys. **23**, 655 (1990).

98. S. Witanachchi, and P. Mukherjee, J. Appl. Phys. **78**, 4099 (1995).

99. D. B. Geohegan, and A. A. Puretzsky, Appl. Phys. Lett. **67**, 197 (1995).

100. Y. Nakata, H. Kaibara, T. Okada, and M. Maeda, J. Appl. Phys. **80**, 2458 (1996).

101. J. Gonzalo, F. Vega, and C. N. Afonso, J. Appl. Phys. **77**, 6588 (1995).

102. P. E. Dyer, A. Issa, and P. H. Key, Appl. Phys. Lett. **57**, 186 (1990).

103. W. K. A. Kumuduni, Y. Nakayama, Y. Nakata, T. Okada, and M. Maeda, Jpn. J. Appl. Phys. **32**, L271 (1993).

104. D. B. Geohegan, in *Laser Ablation of Electronic Materials : Basic Mechanisms and Applications*, (eds.) by E. Fogarassy and S. Lazare (North Holland, Amsterdam, 1992).

105. P. E. Dyer, and J. Sidhu, J. Appl. Phys. **64**, 4657 (1986).

106. D. B. Geohegan, Appl. Phys. Lett. **60**, 2732 (1992).

107. Wanniarachchi K. A. Kumuduni, Y. Nakayama, Y. Nakata, T. Okada, and M. Maeda, J. Appl. Phys. **74**, 7510 (1993).

108. V. Berardi, S. Amoruso, N. Spinelli, M. Armenante, R. Velotta, F. Fuso, M. Allegrini, and E. Arimondo, J. Appl. Phys. **76**, 8077 (1994).

109. D. W. Koopman, H. -L. Siebeneck, and G. Jellison, Phys. Fluids **22**, 526 (1979).

110. A. Neogi, and R. K. Thaerja, Phys. of Plasma **xx**, xxxx (1999).

111. D. K. Zerkle, and A. D. Sappey, IEEE Trans. Plasma Sci. **24**, 37 (1996).

112. A. Gupta, B. Braren, K. G. Casey, B. W. Hussey, and R. Kelly, Appl. Phys. Lett. **59**, 1302 (1991).

113. T. Kerdja, S. Abdelli, D. Ghobrini, and s. Malek, J. Appl. Phys. **80**, 5365 (1996).

114. F. Vega, C. N. Afonso, and J. Solis, J. Appl. Phys. **73**, 2472 (1993).

115. D. B. Geohegan, Appl. Phys. Lett. **62**, 1463 (1993).

116. D. B. Geohegan, A. A. Puretzky, G. Duscher, and S. J. Pennycook, Appl. Phys. Lett. **72**, 2987 (1998).

117. R. K. Thareja, Abhilasha, and R. K. Dwivedi, Laser and Part. Beams **13**, 481 (1995).

118. R. V. Nieuwenhove, and G. V. Oost, Rev. Sci. Instrum. **59**, 1053 (1988).

119. S. Amoruso, M. Armenante, V. Berardi, R. Bruzzese, and N. Spinelli, Appl. Phys. **A 65**, 265 (1997).

120. R. K. Dwivedi, S. P. Singh, and R. K. Thareja, Int. J. Mod. Phys. **B 12**, 2619 (1998)

121. T. M. D. Palma, S. Orlando, A. G. Guidoni, A. J. Paul, J. W. Hastie, and A. Mele, Appl. Surf. Sci. **86**, 68 (1995).

122. F. Lopez, and E. Bernabeu, Thin Solid Films **191**, 13 (1990).

123. D. K. Lathrop, S. E. Russek, and R. A. Buhrman, Appl. Phys. Lett. **51**, 1554 (1987).

124. G. Wagner, E. G. Gonzales, K. Numssen, and H. -U. Habermeier, Physica C **235**, 637 (1994).

125. C. Wyon, R. Gillet, and L. Lombard, Thin Solid Films **122**, 203 (1984).

126. J. C. Angus, J. E. Schultz, P. J. Shiller, J. R. MacDonald, M. J. Mirtich, and S. Dowitz, Thin Solid Films **118**, 311 (1984).

127. W. M. Lau, I. Bello, X. Feng, L. J. Huang, Q. Fuguang, Y. Zhenyu, R. Zhizhang, and S. -T. Lee, J. Appl. Phys. **70**, 5623 (1991).

128. E. Grossman, G. D. Lempert, J. Kulik, D. Marton, J. W. Rabalais, and Y. Lifshitz, Appl. Phys. Lett. **68**, 1214 (1996).

129. X. Queralt, C. Ferrater, F. Sanchez, R. Aguiar, J. Palau, and M. Varela, Appl. Surf. Sci. **86**, 95 (1995).

130. I. P. Llewellyn, N. Rimmer, G. A. Scarsbrook, and R. A. Heinecke, Thin solid films **191**, 135 (1990).

131. J. Narayan, A. R. Srivatsa, M. Peters, S. Yokota, and K. V. Ravi, Appl. Phys. Lett. **53**, 1823 (1988).

132. K. Kitahama, Appl. Phys. Lett. **53**, 1812 (1988).

133. J. Kwo, M. Hong, D. J. Trevor, R. M. Fleming, A. E. White, R. C. Garrow, A. R. Kortan, and K. T. Short, Appl. Phys. Lett. **53**, 2683 (1988).

134. D. B. Chrisey, and G. K. Hubler, in *Pulsed Laser Deposition of Thin Films*, (John Wiley, New York, 1994).

135. I. W. Boyd, in *Laser Processing of Thin Films and Microstructures*, (Springer, New York, 1987).

136. A. Misra and R. K. Thareja, Appl. Surf. Sci. **143**, 56 (1999).

137. J. P. Rebouillat, B. Michelutti, Y. Souche, J. P. Gavigan, D. Givord and A. Lienard, Mater. Res. Soc. Proc. **151**, 259 (1989).

138. A. K. Saxena, R. K. Dwivedi, R. K. Thareja, R. Cowsik, R. Sarkar, and A. Misra, J. Current Science **xx**, xxxx (1999).

139. R. E. Muenchausen, K. M. Hubbard, S. Foltyn, R. C. Estler, N. S. Nogar and C. Jenkins, Appl. Phys. Lett. **56**, 578 (1990).

140. H. Kidoh, A. Morimoto and T. Shimizu, Appl. Phys. Lett. **59**, 237 (1991).

141. R. P. van Ingen, R. H. J. Fastenau and E. J. Mittemeijer, J. Appl. Phys.. **76**, 1871 (1994).

142. I. N. Mihailescu, N. Chitica, L. C. Nistor, M. Popescu, V. S. Teodorescu, I. Ursu, A. Andrei, A. Barborica, A. Luches, M. Luisa De Giorgi, A. Perrone, B. Dubreuil and J. Hermann, J. Appl. Phys. **74**, 5781 (1993).

143. A. Misra, and R. K. Thareja, J. Appl. Phys. (Communications) xx, xxxx (1999).

144. A. H. Miklich, F. C. Wellstood, J. J. Kingston, J. Clarke, M. S. Clclough, K. Char, and G. Zaharchuck, Nature **352**, 482 (1991).

145. G. Koren, R. J. Baseman, A. Gupta, M. I. Lutwyche and R. B. Laibwitz, Appl. Phys. Lett. **56**, 2144 (1990).

146. V. Berardi, S. Amoruso, N. Spinelli, M. Armenante, R. Velotta, F. Fuso, M. Allegrini and E. Arimondo, J. Appl. Phys. **76**, 8077 (1994).

147. E. W. Kreutz, A. Voss, M. Alunovic, J. Funken and H. Sung, Surf. Coat. Technol. **59**, 26 (1993).

148. C. Champeaux, P. Marchet, J. Aubreton, J.-P. Mercurio and A. Catherinot, Appl. Surf. Sci. **69**, 335 (1993).

149. O. Auciello, Materials and Manufacturing Process **6**, 33 (1991).

150. H.-U. Krebs and O. Bremert, Appl. Phys. Lett. **62**, 2341 (1993).

151. A. M. Widdowson, T. J. Jackson, R. Allott, I. C. E. Turcu, S. B. Palmer and C. McCoard, RAL Report # **TR - 96-066**, 172 (1995-96).

152. J. G. Lunney, Appl. Surf. Sci. **86**, 79 (1995).

153. E. Dyer and R.-J. Farlay, J. Appl. Phys. **74**, 1442 (1993).

154. G. B. Blanchet, Appl. Phys. Lett. **62**, 479 (1993).

155. P. Perlin, A. Polain and T. Suski, Phys. Rev. B **47**, 2874 (1993).

156. R. E. Leuchtner, A. C. Harms and A. W. Castleman, Jr., J. Chem. Phys. **94**, 1093 (1991).

157. E. A. Rohlfing, D. M. Cox and A. Kaldor, J. Chem. Phys. **81**, 3322 (1984).

158. U. Näher, H. Göhlich, T. Lange and T. P. Martin, Phys. Rev. Lett. **68**, 3416 (1992).

159. D. E. Powers, S. G. Hansen, M. E. Geusic, D. L. Michalopopulos and R. E. Smalley, J. Chem. Phys. **78**, 2866 (1983).

160. T. Yoshida, S. Takeyama, Y. Yamada and K. Mutoh, Appl. Phys. Lett. **68**, 1772 (1996).

161. R. W. Dreyfus, R. Kelly and R. E. Walkup and R. Srinivasan, SPIE **710**, 46 (1986).

162. A. A. Voevodin, S. D. Walck, J. S. Solomon, P. J. John, D. C. Ingram, M. S. Donley and J. S. Zabinsky, J. Vac. Sci. Technol. A **14**, 1927 (1996).

163. S. Leppävuori, J. Levoska, J. Vaara and O. Kusmartseva, Mat. Res. Soc. Symp. Proc. **285**, 557 (1993).

164. K. Fukushima, M. Badaye, and T. Morishita, J. Appl. Phys. **79**, 3697 (1996).

165. A. Lembo, F. Fuso, M. Allegrini, E. Arimondo, V. Berardi, N. Spinelli, F. Leccabue, B. E. Watts, G. Franco, and G. Chiorboli, Appl. Phys. Lett. **63**, 1194 (1993).

166. H. C. Ong, and R. P. H. Chang, Phys. Rev. B **55**, 213 (1997)

167. T. F. Tseng, M. H. Yeh, K. S. Liu, and I. N. Lin, J. Appl. Phys. **80**, 4984 (1996).

168. R. K. Singh, N. Biunno, and J. Narayan, Appl. Phys. Lett. **53**, 1013 (1988).

169. H. S. Kim, and H. S. Kwok, Appl. Phys. Lett. **61**, 2234 (1992).

170. M. Ozegowski, S. Metev, and G. Sepold, Appl. Surf. Sci., **127-129**, 614 (1998).

171. J. C. S. Kools, in *Pulsed Laser Deposition of Thin Films*, (eds.) D. B. Chrisey, and G. K. Hubler, (John Wiley, New York, 1994).

172. A. A. Gorbunov, and V. I. Konov, Sov. Phys. Tech. Phys. **34**, 77 (1989).

173. C. Björmander, A. M. Grishin, B. M. Moon, J. Lee, and K. V. Rao, Appl. Phys. Lett. **64**, 3646 (1994).

174. J. Y. Gu, K. H. Kim, T. W. Noh, and K. -S. Suh, J. Appl. Phys. **78**, 6151 (1995).

175. M. Y. Chen, and P. T. Murray, J. Vac. Sci. Technol. A **16**, 2093 (1998).

176. R K Thareja, R K Dwivedi, A Misra, A Mitra, and A Neogi, Metals, Materials and Processes **10**, 217 (1998)

177. K. Jagannadham, A. K. Sharma, Q. Wei, R. Kalyanraman, and J. Narayan, J. Vac. Sci. Technol. A **16**, 2804 (1998).

178. K. Seki, X. Xu, H. Okabe, J. M. Frye, and J. B. Halpern, Appl. Phys. Lett. **60**, 2234 (1992).

179. M. Ohring, *The Materials Science of Thin Films,*(Academic Press, Inc. New York, 1992).

180. J. F. Asmus, F. S. Baker, Record of 10th Symp. On Electron, Ion, and Laser Beam Technology (San Francisco Press, San Francisco, 1969).

181. R. Solanki, G. J. Collins, Appl. Phys. Lett. **42**, 662 (1983).

182. M. Wautelet, Mat. Lett. **2**, 20 (1994).

183. I. W. Boyd, Contemp. Phys. **24**, 461 (1983).

184. S. Cao, A. J. Pedraza, D. H. Lowndes, and L. F. Allard, Appl. Phys. Lett. **65**, 2940 (1994).

185. R. Serna, and C. N. Afonso, Appl. Phys. Lett. **69**, 1541 (1996).

186. R. D. Vispute, J. Narayan, Hong Wu, and K. Jagannadham, J. Appl. Phys. **77**, 4724 (1995).

187. R. D. Vispute, H. Wu, and J. Narayan, Appl. Phys. Lett. **67**, 1549 (1995).

188. J. F. Moore, D. R. Strongin, P. B. Comita, M. W. Ruckman, and M. Strongin, Appl. Phys. Lett. **65**, 368 (1999).

189. S. Sato, T. Yoneyama, and T. Horaguchi, Jpn. J. Appl. Phys. **36**, L1328 (1997).

190. G. N. V. D. Hoven, E. Snoeks, A. Polman, J. W. M. V. Uffelen, Y. S. Oei, and M. K. Smit, Appl. Phys. Lett. **62**, 3065 (1993).

191. M. G. Norton, P. G. Kotula, and C. B. Carter, J. Appl. Phys. **70**, 2871 (1991).

192. P. Bhattacharya, and D. N. Bose, Jpn. J. Appl. Phys. **30**, L1750 (1991).

193. A. Morimoto, Y. Yamanaka, and T. Shimizu, Jpn. J. Appl. Phys. **35**, L227 (1996).

194. K. A. Brown, S. A. Ustin, L. Lauhon, and W. Ho, J. Appl. Phys. **79**, 7667 (1996).

195. R. D. Vispute, V. Talyansky, R. P. Sharma, S. Choopun, M. Downes, T. Venkatesan, K. A. Jones, A. A. Lliadis, M. A. Khan, J. W. Yang, Appl. Phys. Lett. **71**, 102 (1997).

196. M. He, N. Cheng, P. Zhou, H. Okabe, and J. B. Halpern, J. Vac. Sci. Technol. A **16**, 2372 (1998).

197. P. M. Lundquist, W. P. Lin, Z. Y. Xu, G. K. Wong, E. D. Rippert, J. A. Helfrich, and J. B. Ketterson, Appl. Phys. Lett. **65**, 1085 (1994).

198. X. Tang, F. Hossain, K. Wongchotigul, and M. G. Spencer, Appl. Phys. Lett. **72**, 1501 (1998).

199. T. P. Hughes, in *Plasma and Laser Light*, (Wiley, New York, 1975).

200. P. K. Carroll, and E. T. Kennedy, Contemp. Phys. **22**, 61 (1981).

201. B. H. Ripin, C. K. Manka, T. A. Peyser, E. A. Mclean, J. A. Stamper, A. N. Mostovych, J. Grun, K. Keavney, J. Y. Crawford, and J. D. Huba, Laser and Part. Beam **8**, 183 (1990).

202. S. Suckewer, C. H. Skinner, H. Milchberg, C. Keane, and D. Voorhees, Phys. Rev. Lett. **55**, 1753 (1985).

203. Ya. B. Zel'dovich, and Yu. P. Raizer, in *Physics of Shock waves and High Temperature Hydrodynamic Phenomenon* Vol. I, (Academic, NY, 1996).

204. M. A. Liberman, and A. L. Velikovich, in *Physics of Shock Waves in Gases and Plasmas* (Springer-Verlag, Berlin, 1986).

205. K. Fukushima, M. Badaye, and T. Morishita, J. Appl. Phys. **79**, 3697 (1996).

206. T. Sasakai, S. Terauchi, N. Koshizaki, and H. Umehara, Ceram. Process. **43**, 2636 (1997).

207. H. -U. Krebs, S. Fähler, and O. Bremert, Appl. Surf. Sci. **86**, 86 (1995).

208. J. C. S. Kools, C. J. C. M. Nillesen, S. H. Brongersma, E. van de Riet, and J. Dieleman, J. Vac. Sci. Technol. **A10**, 1809 (1992).

209. J. Seth, R. Padiyath, D. H. Rasmussen, and S. V. Babu, Appl. Phys. Lett. **63**, 473 (1993).

210. S. P. McGinnis, M. A. Kelly, S. B. Hagström, and R. L. Alvis, J. Appl. Phys. **79**, 170 (1996).

211. B. E. Williams, H. S. Kong, and J. T. Glass, J. Mater. Res. **5**, 801 (1990).

212. J. Singh, M. Vellaikal, and J. Narayan, J. Appl. Phys. **73**, 4351 (1993).

213. M. Yoshimoto, T. Arakane, T. Asakawa, K. Horiguchi, K. Hirai, and H. Koinuma, Jp. J. Appl. Phys. **32**, L1081 (1993).

214. T. Som, S. Dhar, S. N. Minwalla and V. N. Kulkarni, Nucl. Instr. Meth. B **122**, 244 (1997).

215. R. O. Dhillon, J. A. Woolman and V. Katkanant, Phys. Rev B **29**, 3482 (1984).

216. H. D. Bist, Proc. Ind. Assoc. Cult. Sci., **80 B**, 1 (1997).

217. Abhilasha, Ph. D. Thesis, IIT Kanpur (1994).

218. R. K. Dwivedi, Ph. D. Thesis, IIT Kanpur (1997).

219. H. R. Griem, in *Plasma Spectroscopy*, (McGraw Hill, New York, 1964).

220. G. Bekefi, in *Principles of Laser Plasmas*, (Wiley, New York, 1976).

221. J. T. Knudtson, W. B. Green and D. G. Sutton, J. Appl. Phys. **61**, 4771 (1987).

222. R. W. P., in Plasma Diagnostic Techniques, (eds.) R. H. Huddlestone and S. L. Leonard (Academic Press, New York, 1965).

223. P. L. G. Ventzek, R. M. Gilgenbach, C. H. Ching, and R. A. Lindley, J. Appl. Phys. **72**, 1696 (1996).

224. Tripti Srivastava, M. Tech. Thesis, IIT Kanpur (1999).

225. J. M. Hendron, C. M. O. Mahony, T. Morrow, and W. G. Graham, J. Appl. Phys. **81**, 2131 (1997).

226. A. Misra, T. Srivastava, and R. K. Thareja, Int. J. Mod. Phys. **xx**, xxxx (1999).

227. W. K. Chu, J. W. Mayer, and M. -A Nicolet, in Backscattering Spectrometry (Academic Press, New York, 1978).

228. L. R. Dolittle, Nucl. Inst. Meth. **B 9**, 344 (1985).

229. Y. Nakata, K. A. K. Wanniarachchi, T. Okada, and M. Maeda, Appl. Phys. Lett. **64**, 2599 (1994).

230. R. E. Hall, J. Appl. Phys. **40**, 1941 (1969).

231. D. B. Geohegan, A. A. Puretzky, Appl. Surf. Sci. **96**, 131 (1996).

232. A. Neogi, A. Misra, and R. K. Thareja, J. Appl. Phys. **83**, 2831 (1998).

233. P. K. Schenck, J. W. Hastie, A. J. Paul, and D. W. Bonnell, Opt. Eng. **35**, 3199 (1996).

234. R. Niedrig, and O. Bostanjoglo, J. Appl. Phys. **81**, 480 (1997).

235. V. Bulatov, L. Xu, and I. Schechter, Anal. Chem. **68**, 2966 (1996).

236. R. Kelly, A. Miotello, B. Braren, and C. E. Otis, Appl. Phys. Lett. **60**, 2980 (1992).

237. M. Ohkoshi, T. Yoshitake, and K. Tsushima, Appl. Phys. Lett. **64**, 3340 (1994).

238. D. B. Geohegan, Thin Solid Films **220**, 138 (1992).

239. O. B. Anan'in, Y. A. Bykovskii, Y. V. Eremin, A. A. Zhuravlev, O. S. Lyubchenko,

I. K. Novikov, and S. P. Frolov, Laser Phys. **2**, 711 (1992).

240. M. A. Cappelli, P. H. Paul, and R. K. Hanson, Appl. Phys. Lett. **56**, 1715 (1990).

241. Y. Nakata, K. A. K. Wanniarachchi, T. Okada, and M. Maeda, Appl. Phys. Lett. **66**, 3206 (1995).

242. R. M. Gilgenbach, and P. L. G. Ventzek, Appl. Phys. Lett. **58**, 1597 (1991).

243. Z. Toth, B. Hopp, F. Ignácz, T. Szórényı, and Z. Bor, Appl. Phys. **A 60**, 431 (1995).

244. J. J. Chang, and B. E. Warner, Appl. Phys. Lett. **69**, 473 (1996).

245. A. Sircar, R. K. Dwivedi, and R. K. Thareja, Appl. Phys. **B 63**, 623 (1996).

246. P. S. R. Prasad, Abhilasha, and R. K. Thareja, Phys. Stat. Solids (a) **139**, K1 (1993).

247. E. A. Rohlfing, J. Chem. Phys. **89**, 6103 (1988).

248. D. Temple, and A. Reisman, J. Electron. Mater. **19**, 995 (1990).

249. W. Lin, L. Meng, G. Chen, and H. Liu, Appl. Phys. Lett. **66**, 2066 (1995),

250. W. P. Lin, P. M. Lundquist, G. K. Wong, E. D. Rippert, and J. B. Ketterson, Appl. Phys. Lett. **63**, 2875 (1993).

251. S. Strite, and H. Morkoc, J. Vac. Sci. Technol. B **10**, 1237 (1992).

252. J. R. Heffelfinger, D. L. Medlin, and K. F. McCarty, J. Appl. Phys. **85**, 466 (1999).

253. S. P. S. Porto, and R. S. Krishnan, J. Chem. Phys. **47**, 1009 (1967).

254. A. Misra, H. D. Bist, R. K. Thareja, M. S. Navati, and J. Narayan, J. Chem. Phys. (communicated).

255. F. A. Cotton and G. Wilkinson, in *Advanced Inorganic Chemistry*, (John Wiley, New York, 1988).

256. J. Emsley, in *The Elements*, (Oxford University Press, U. K, 1990).

A 131099

Date Slip

This book is to be returned on the date last stamped.